The Perseus ALMA Chemistry Survey (PEACHES). I. The Complex Organic Molecules in Perseus Embedded Protostars

Yao-Lun Yang, Nami Sakai, Yichen Zhang, Nadia M Murillo, Ziwei E Zhang, Aya E Higuchi, Shaoshan Zeng, Ana López-Sepulcre, Satoshi Yamamoto, Bertrand Lefloch, et al.

The Astrophysical Journal, 910:20 (38pp), 2021 March 20 https://doi.org/10.3847/1538-4357/abdfd6

The Perseus ALMA Chemistry Survey (PEACHES). I. The Complex Organic Molecules in Perseus Embedded Protostars

Yao-Lun Yang[1,2], Nami Sakai[2], Yichen Zhang[2], Nadia M. Murillo[2], Ziwei E. Zhang[2], Aya E. Higuchi[3], Shaoshan Zeng[2], Ana López-Sepulcre[4], Satoshi Yamamoto[5], Bertrand Lefloch[4], Mathilde Bouvier[4], Cecilia Ceccarelli[4], Tomoya Hirota[3], Muneaki Imai[5], Yoko Oya[5], Takeshi Sakai[6], and Yoshimasa Watanabe[7]
[1] Department of Astronomy, University of Virginia, Charlottesville, VA 22904-4235, USA; yaolunyang.astro@gmail.com
[2] RIKEN Cluster for Pioneering Research, Wako-shi, Saitama, 351-0106, Japan
[3] National Astronomical Observatory of Japan, Osawa, Mitaka, Tokyo 181-8588, Japan
[4] Univ. Grenoble Alpes, CNRS, Institut de Planétologie et d'Astrophysique de Grenoble (IPAG), F-38000 Grenoble, France
[5] Department of Physics, The University of Tokyo, 7-3-1, Hongo, Bunkyo-ku, Tokyo 113-0033, Japan
[6] Department of Communication Engineering and Informatics, Graduate School of Informatics and Engineering, The University of Electro-Communications, Chofugaoka, Chofu, Tokyo 182-8585, Japan
[7] Shibaura Institute of Technology, 3-9-14 Shibaura, Minato-ku, Tokyo 108-8548, Japan
Received 2020 September 18; revised 2021 January 18; accepted 2021 January 21; published 2021 March 23

Abstract

To date, about two dozen low-mass embedded protostars exhibit rich spectra with lines of complex organic molecules (COMs). These protostars seem to possess a different enrichment in COMs. However, the statistics of COM abundance in low-mass protostars are limited by the scarcity of observations. This study introduces the Perseus ALMA Chemistry Survey (PEACHES), which aims at unbiasedly characterizing the chemistry of COMs toward the embedded (Class 0/I) protostars in the Perseus molecular cloud. Of the 50 embedded protostars surveyed, 58% of them have emission from COMs. 56%, 32%, and 40% of the protostars have CH_3OH, CH_3OCHO, and N-bearing COMs, respectively. The detectability of COMs depends neither on the averaged continuum brightness temperature, a proxy of the H_2 column density, nor on the bolometric luminosity and the bolometric temperature. For the protostars with detected COMs, CH_3OH has a tight correlation with CH_3CN, spanning more than two orders of magnitude in column densities normalized by the continuum brightness temperature, suggesting a chemical relation between CH_3OH and CH_3CN and a large chemical diversity in the PEACHES samples at the same time. A similar trend with more scatter is also found between all identified COMs, which hints at a common chemistry for the sources with COMs. The correlation between COMs is insensitive to the protostellar properties, such as the bolometric luminosity and the bolometric temperature. The abundance of larger COMs (CH_3OCHO and CH_3OCH_3) relative to that of smaller COMs (CH_3OH and CH_3CN) increases with the inferred gas column density, hinting at an efficient production of complex species in denser envelopes.

Unified Astronomy Thesaurus concepts: Star formation (1569); Astrochemistry (75); Chemical abundances (224); Interstellar molecules (849)

Supporting material: figure set

1. Introduction

Planet formation may start during the embedded phase of star formation (Tychoniec et al. 2020). In the scenario in which planets form from the embedded disks, resulting in substructures, the chemistry of embedded disks may play a significant role for the chemical composition of the forming planets. In the past two decades, observations show the emission of complex molecules toward the center of several protostellar cores. From the astronomical point of view, complex molecules are usually defined as a species that contains six or more atoms (Herbst & van Dishoeck 2009). All detected complex molecules are organic. It can be saturated (e.g., Cazaux et al. 2003; Bottinelli et al. 2007; Jørgensen et al. 2016; Ceccarelli et al. 2017; Lee et al. 2017 and the ALMA PILS Survey) or unsaturated (e.g., carbon-chain molecules: Sakai & Yamamoto 2013; Sakai et al. 2014; Law et al. 2018). The saturated organic molecules, often called complex organic molecules (COMs) or interstellar COMs (iCOMs), have single covalent bonds between carbon atoms, making them rich in hydrogen, while the unsaturated organic molecules contain double or triple bonds between carbon atoms, making them poor in hydrogen. Most of the COMs appear in the inner warm envelope (e.g., Bottinelli et al. 2004b) and/or the surface of the embedded disk where the temperature is warm ($\gtrsim$100 K; e.g., Lee et al. 2017), while COMs in some sources, such as L1157, are linked to molecular shocks (e.g., Bachiller et al. 2001; Lefloch et al. 2017; Codella et al. 2020). The connection between a disk-like structure and the emission of COMs has been elusive (Belloche et al. 2020). However, if the disk formation can inherit COMs from the embedded envelope (e.g., Drozdovskaya et al. 2014), the chemistry of COMs at the embedded phase of star formation may implicate future developments of organics on the planets.

For low-mass protostars, gas-phase COMs typically emit from the warm inner protostellar envelope ($T \gtrsim 100$ K), which corresponds to $\lesssim$100 au for typical low-mass protostars (Bottinelli et al. 2004b; Ceccarelli et al. 2007). Thus, COMs serve as a tracer of the inner envelope where a disk may be forming (Aikawa 2013), measuring the chemistry and dynamics of embedded disks (Sakai et al. 2014; Lee et al. 2017). Other

Table 1
ALMA Projects for PEACHES

Project Code	Regions	Calibrators (amplitude, bandpass, phase)	Baselines	$\theta_{\rm beam}$[a]	$\theta_{\rm MRS}$[b]
2016.1.01501.S[c]	L1448, L1455, NGC 1333	J0238+1636, J0237+2848, J0336+3218	15–919 m	$\sim 0\farcs6 \times 0\farcs4$	$\sim 6\farcs3$
2017.1.01462.S[d]	B1, IC 348, B5	J0237+2848, J0237+2848, J0336+3218	15–1231 m	$\sim 0\farcs5 \times 0\farcs3$	$\sim 4\farcs3$

Notes.
[a] The beam size varies slighly from source to source. Table 4 gives the synthesized beam size for each source.
[b] Maximum recoverable scale.
[c] Observations were performed on 2016 November 16, 19, 26, 29, and 30.
[d] Observations were performed on 2018 September 10 and 12.

processes, such as jets and outflows, can also produce the emission of COMs by sputtering and/or shock chemistry (e.g., Arce et al. 2008; Lefloch et al. 2017). Furthermore, accretion shocks occurred when the gas falls onto the disk may enhance the desorption of COMs (Oya et al. 2016; Miura et al. 2017; Csengeri et al. 2018). However, Belloche et al. (2020) showed no clear correlation between the COM emission and the occurrence of disk-like structures possibly due to specific conditions required for efficient desorption via accretion shocks (Miura et al. 2017) or insufficient sensitivity. Outbursting protostars, such as FU Orionis objects, can temporarily increase the COM abundance with elevated temperature (van't Hoff et al. 2018b; Lee et al. 2019). In the more evolved stage, COMs have only been detected in a few disks (Öberg et al. 2015; Walsh et al. 2016; Favre et al. 2018; Podio et al. 2020).

While recent observations show abundant COMs in several embedded protostars, the probability of the existence of COMs and their relationship to the star formation process yet remain to be understood. Several protostars are rich in long carbon-chain molecules but have few COMs, such as L1527 (Sakai et al. 2010) and IRAS 15398−3359 (Sakai et al. 2009; Oya et al. 2014; Okoda et al. 2018). In comparison, interferometric observations detected both COMs and carbon-chain molecules in several protostars, such as IRAS 16293−2422 (Jaber Al-Edhari et al. 2017; Murillo et al. 2018), L483 (Oya et al. 2017), and B335 (Imai et al. 2016). Single-dish surveys showed no correlation between COMs and long carbon-chain molecules (Graninger et al. 2016; Higuchi et al. 2018). Interestingly, carbon-chain molecules tend to distribute at a larger spatial scale than that of COMs (Imai et al. 2016; Oya et al. 2017; Bouvier et al. 2020). Aikawa et al. (2020) demonstrated that the conditions of prestellar cores can result in a larger spatial extent of carbon-chain molecules that coexist with COMs or deficient of carbon-chain molecules in COM-rich sources. Moreover, dust opacity may obscure the emission of COMs in submillimeter wavelengths, introducing additional uncertainty to our understanding of COMs (De Simone et al. 2020). Therefore the chemical pathways of complex molecules at the embedded protostars remain ill-constrained, highlighting the need of unbiased chemistry surveys to characterize the statistics of COMs (e.g., Caux et al. 2011; Lefloch et al. 2018).

The Perseus molecular cloud is one of the most active nearby star-forming regions, which extends ∼10 pc on the sky. Many studies assume a distance of 235 pc for Perseus based on the maser observations toward NGC 1333 SVS 13 (Hirota et al. 2008). Recently, Ortiz-León et al. (2018) estimated a distance of 321 ± 10 pc for IC 348 using VLBA and a distance of 293 ± 22 pc for NGC 1333 using Gaia parallaxes. Zucker et al. (2020) combined the Gaia parallaxes and photometric data with a Bayesian framework to revise the distances toward several sightlines of Perseus, resulting in distances ranging from 234 to 331 pc.

In Perseus molecular cloud, infrared and submillimeter surveys reveal more than 400 young stellar objects as well as ∼100 dense cores, which contains ∼50 Class 0 and I protostars (Hatchell et al. 2005; Jørgensen et al. 2008; Dunham et al. 2013; hereafter the embedded protostars). The Perseus molecular cloud contains star-forming regions in a wide range of environments. The majority of protostars in Perseus are associated with the two clusters, NGC 1333 and IC 348. NGC 1333, which has many active outflows (Knee & Sandell 2000; Plunkett et al. 2013), was thought to be younger than IC 348 based on the higher extinction and abundance of protostars; however, Luhman et al. (2016) showed a similar age for two regions based on the evolutionary modeling of young stars and brown dwarfs. The embedded protostars associated with IC 348 lie southwest of the open cluster, IC 348, near a prominent outflow, HH 211 (e.g., Lee et al. 2009). Most of the other embedded protostars at Perseus are related to L1448, L1455, Barnard 1 (B1), and Barnard 5 (B5). L1448 has active outflows that may regulate the ongoing star formation (Curtis et al. 2010). The low abundance of Class 0 protostars in L1455 suggests a more evolved protostellar population than that in other regions (Hatchell et al. 2007); B1 exhibits rich spectra of deuterated species (Marcelino et al. 2005; Roueff et al. 2005). B5 has a dominant embedded protostar, IRS1, along with three gravitationally bound gas condensation at a separation greater than 1000 au (Pineda et al. 2015). Furthermore, the protostellar multiplicity in Perseus has been extensively studied by the VLA Nascent Disk and Multiplicity Survey (VANDAM) of Perseus protostars, showing a multiplicity fraction of 0.57 ± 0.09 and 0.23 ± 0.08 for Class 0 and I protostars, respectively (Tobin et al. 2016, 2018; Segura-Cox et al. 2018; Tychoniec et al. 2018). Murillo et al. (2016) further characterized the spectral energy distributions of all sources identified in the VANDAM survey to derive protostellar properties, such as bolometric luminosities ($L_{\rm bol}$), bolometric temperatures ($T_{\rm bol}$), and evolutionary stage classification. Several surveys using CO isotopologues and NH_3 probe chemical variations and kinematics at cloud scale (Pineda et al. 2008; Friesen et al. 2017). Thus, the Perseus molecular cloud provides an ideal test bed for chemistry in embedded protostars by surveying the protostars within each region and across the entire cloud.

Higuchi et al. (2018) presented a pilot survey of the chemistry in the Perseus embedded protostars with Nobeyama 45 m telescope and IRAM 30 m telescope, which surveyed all Class 0/I protostars (Hatchell et al. 2007) that have $L_{\rm bol}$ greater than 1 $L_\odot$ (0.7 $L_\odot$for protostars in B1 and B5) and the envelope mass greater than 1 $M_\odot$. This pilot survey probes the molecules such as C_2H, c-C_3H_2, and CH_3OH. The majority of the sources have emission of both CH_3OH and carbon-chain molecules. They suggested a possible correlation between the

Table 2
PEACHES Sample

Source	Common Names	R.A. (J2000) (hh:mm:ss)	Decl. (J2000) (dd:mm:ss)	v_{lsr} (km s^{-1})	Reference (v_{lsr})
Per-emb 22 B		03:25:22.35	30:45:13.11	4.3	S19
Per-emb 22 A		03:25:22.41	30:45:13.26	4.3	S19
L1448 NW	L1448 IRS 3C	03:25:35.67	30:45:34.16	4.2	H18
Per-emb 33 B/C		03:25:36.32	30:45:15.19	5.3	S19
Per-emb 33 A		03:25:36.38	30:45:14.72	5.3	S19
L1448 IRS 3A		03:25:36.50	30:45:21.90	4.6	H18
Per-emb 26		03:25:38.88	30:44:05.28	5.4	S19
Per-emb 42		03:25:39.14	30:43:57.90	5.8	S19
Per-emb 25	IRAS 03235+3004	03:26:37.51	30:15:27.81	5.5	S18
Per-emb 17	L1455 IRS 1, IRAS 03245+3002	03:27:39.11	30:13:02.96	6.0	S19
Per-emb 20	L1455 IRS 4	03:27:43.28	30:12:28.88	5.3	S19
L1455 IRS 2		03:27:47.69	30:12:04.33	5.1	H18
Per-emb 35 A	NGC 1333 IRAS 1	03:28:37.10	31:13:30.77	7.4	this study
Per-emb 35 B	NGC 1333 IRAS 1	03:28:37.22	31:13:31.74	7.3	this study
Per-emb 27	NGC 1333 IRAS 2A	03:28:55.57	31:14:36.97	6.5	this study
EDJ2009-172		03:28:56.65	31:18:35.43	...	...
Per-emb 36	NGC 1333 IRAS 2B	03:28:57.37	31:14:15.77	6.9	S19
Per-emb 54	NGC 1333 IRAS 6	03:29:01.55	31:20:20.49	7.9	S19
SVS 13B	NGC 1333 SVS 13B	03:29:03.08	31:15:51.73	8.5	S19
SVS 13A2	VLA 3	03:29:03.39	31:16:01.58	8.4	S18
Per-emb 44	NGC 1333 SVS 13A	03:29:03.76	31:16:03.70	8.7	S19
Per-emb 15		03:29:04.06	31:14:46.23	6.8	S19
Per-emb 50	IRAS 03260+3111 A	03:29:07.77	31:21:57.11	9.3	this study
Per-emb 12 B	NGC 1333 IRAS 4A2	03:29:10.44	31:13:32.08	6.9	S19
Per-emb 12 A	NGC 1333 IRAS 4A1	03:29:10.54	31:13:30.93	6.9	S19
Per-emb 21	NGC 1333 IRAS 7 SM2	03:29:10.67	31:18:20.16	8.6	this study
Per-emb 18	NGC 1333 IRAS 7 SM1	03:29:11.27	31:18:31.09	8.1	S19
Per-emb 13	NGC 1333 IRAS 4B1	03:29:12.02	31:13:07.99	7.1	S19
IRAS4B'	NGC 1333 IRAS 4B2	03:29:12.85	31:13:06.87	7.1	S19
Per-emb 14	NGC 1333 IRAS 4C	03:29:13.55	31:13:58.12	7.9	S19
EDJ2009-235		03:29:18.26	31:23:19.73	7.7	this study
EDJ2009-237		03:29:18.74	31:23:25.24	...	...
Per-emb 37		03:29:18.97	31:23:14.28	7.5	this study
Per-emb 60		03:29:20.05	31:24:07.35	...	...
Per-emb 5	IRAS 03282+3035	03:31:20.94	30:45:30.24	7.3	S19
Per-emb 2	IRAS 03292+3039	03:32:17.92	30:49:47.81	7.0	S19
Per-emb 10	B1-d	03:33:16.43	31:06:52.01	6.4	S19
Per-emb 40	B1-a	03:33:16.67	31:07:54.87	7.4	S19
Per-emb 29	B1-c	03:33:17.88	31:09:31.74	6.1	this study
B1-b N		03:33:21.21	31:07:43.63	6.6	C16
B1-b S		03:33:21.36	31:07:26.34	6.6	C16
Per-emb 16		03:43:50.97	32:03:24.12	8.8	S19
Per-emb 28		03:43:51.01	32:03:08.02	8.6	S19
Per-emb 1	HH 211 MMS	03:43:56.81	32:00:50.16	9.4	S19
Per-emb 11 B	IC 348 MMS	03:43:56.88	32:03:03.08	9.0	S19
Per-emb 11 A	IC 348 MMS	03:43:57.07	32:03:04.76	9.0	S19
Per-emb 11 C	IC 348 MMS	03:43:57.70	32:03:09.82	9.0	S19
Per-emb 55	IRAS 03415+3152	03:44:43.30	32:01:31.22	12.0	S19
Per-emb 8		03:44:43.98	32:01:35.19	11.0	S19
Per-emb 53	B5 IRS 1	03:47:41.59	32:51:43.62	10.2	this study

References. C16 = Carney et al. (2016); H18 = Higuchi et al. (2018); S18 = Stephens et al. (2018); S19 = Stephens et al. (2019).

location of sources within the clouds and the ratio of CH_3OH/C_2H indicating the environmental effect on the chemistry. However, single-dish observations of CH_3OH are contaminated by the contribution of the photodissociation region of the molecular clouds hosting the protostar (Bouvier et al. 2020). In addition, chemical surveys with single-dish telescopes are often less sensitive to detect the COMs in the vicinity of the protostars. To trace those COMs, high spatial resolution from interferometric observations is crucial. Based on the NOEMA observations of 26 embedded protostars in several molecular clouds, Belloche et al. (2020) detected CH_3OH and other COMs in about a half of them. Interestingly, CH_3OH and CH_3CN show a strong correlation, while their chemical link remains unclear. They also investigated the origins of COMs and revealed apparent chemical difference among binary systems in their survey. Internal luminosity is the

Table 3
Frequency Setup

Frequency Range (MHz)	Channel Width (kHz)	Channel Width (km s^{-1})
2016.1.01501.S		
243483–243542	122.070	0.150
243878–243937	122.070	0.150
244200–244259	122.070	0.150
244898–244957	122.070	0.149
246186–247124	976.562	1.187
257489–257548	122.070	0.142
258218–258276	122.070	0.142
259288–259347	122.070	0.141
258974–259032	122.070	0.141
262046–262104	122.070	0.140
260442–260551	122.070	0.140
261787–261845	122.070	0.140
2017.1.01462.S		
243502–243561	122.070	0.150
243897–243956	122.070	0.150
244219–244278	122.070	0.150
244917–244975	122.070	0.149
245805–246743	976.562	1.189
257509–257568	122.070	0.142
258238–258296	122.070	0.142
259308–259366	122.070	0.141
258993–259052	122.070	0.141
262066–262124	122.070	0.140
260462–260571	122.070	0.140
261807–261865	122.070	0.140

most impacting parameter for the COM chemical composition, while the existence of a disk-like structure has no obvious impact to the COM emission. A combined analysis of a few protostars from four different star-forming regions (Perseus, Serpens, Ophiuchus, and Orion) showed no significant correlation between the occurrence of COMs and the $L_{\rm bol}$ (van Gelder et al. 2020). Furthermore, the abundance of a few O-bearing COMs to CH_3OH are similar for the sources in different regions. They suggested an inheritance scenario where the evolution in the prestellar phase dominates the chemistry. Despite the growing sample of COM detections in embedded protostars, the statistics of COM abundance remain unconstrained due to the biases from the source selection, limited resolution, and small sample sizes. To unbiasedly understand the chemistry, we conducted the Perseus ALMA Chemistry Survey (PEACHES) that probes the complex chemistry toward Perseus embedded protostars. The source selection followed the same criteria as in Higuchi et al. (2018) with a few pointing modifications using the results from the VANDAM of Perseus protostars (Tobin et al. 2016). The PEACHES survey also probed the outflows of embedded protostars (e.g., NGC1333 IRAS 4C: Zhang et al. 2018).

Section 2 describes the details of our ALMA observations. Section 3 presents the identification of protostellar sources and the methodology of spectral extraction, line identification, and modeling. Section 4 shows the detection statistics of COMs and their correlations. Section 5 discusses the implications of the observed COM abundance on the current understanding of chemistry of COMs at protostellar sources. Finally, Section 6 summarizes the findings of this study.

2. Observations

The PEACHES observations were conducted in two ALMA projects (2016.1.01501.S and 2017.1.01462.S; PI: N. Sakai), surveying 37 fields toward the Perseus molecular cloud. Each project surveyed different regions in the Perseus molecular cloud. Table 1 lists the basic information for each project, while Table 2 shows basic information of the sources observed in the PEACHES survey. The ALMA correlator was configured to have 13 spectral windows at Band 6. The windows have 12 narrow spectral windows with 480 channels and a wide spw with 980 channels. The narrow spectral windows were tuned to observe specific molecular species, such as SiO, C_2H, CS, CH_3OH, and CH_3CN, with a spectral resolution of 122 kHz ($\sim$0.15 km s^{-1}), while the wide spectral window was scheduled to observe the continuum with a resolution of 0.976 MHz ($\sim$1.2 km s^{-1}). In later imaging processes, we combined the two spectral windows potentially affected by the broad SiO emission, resulting in a total of 12 spectral windows. The frequency setups for the two ALMA projects are largely identical, except for the wide continuum window, which shifts by $\sim$380 MHz. Table 3 lists the frequency ranges for each spectral window and the corresponding channel widths.

We used CASA (McMullin et al. 2007) for standard calibration and imaging of the continuum and spectral lines with `tclean`. Self-calibration is not applied in this study because some of the samples have weak continuum emission. Because of the rich spectra, we manually flagged the lines for the continuum imaging. The images were cleaned down to 0.022 Jy beam^{-1}, except for the continuum spectral windows, whose images were cleaned down to 0.008 Jy beam^{-1} due to their lower spectral resolution. The line imaging used the "multiscale" deconvolver with a robust parameter of 0.5 because the targeted emission traces different spatial scales (e.g., SiO for outflows and COMs for the inner envelope/disk). Last, we applied the primary beam correction to the image cubes. The synthesized beam is about $0\farcs6 \times 0\farcs4$ averaged across all spectral windows. In this study, we assume a distance of 300 pc for the entire Perseus cloud, resulting in a synthesized beam of 180 au $\times$ 120 au.

3. Analyses

3.1. Identification of Young Stellar Objects

In the 37 fields of view, 51 continuum peaks are identified. We used the CASA task `imfit` to iteratively fit a 2D Gaussian profile for continuum emission down to 5σ of the residual image within the central 70% of the size of the primary beam (20″). We measured the noise of the continuum emission (σ) from the vicinity of the continuum emission. For the field centered on Per-emb 16, which also covers Per-emb 28, the fitting used a threshold of 4σ and extended the mask to the entire primary beam because Per-emb 28 is detected toward the edge of the primary beam, where the noise is higher. The continuum of the multiple systems were manually fitted to the individual continuum peaks. The two protostars L1448 IRS 2E and SVS 3 become nondetections in our observations due to their low brightness. SVS 13C locates at the edge of the primary beam, resulting in a noisy continuum. Thus, we excluded SVS 13C from this study, making a total of 50 protostars.

Table 4 lists the properties ot the fitted continuum emission, while Figure 1 shows the continuum emission along with the

Table 4
Fitted Continuum

Source	Beam	Convolved Size	Deconvolved Size	PA	$T_{b,\ cont}$ (K)	Multiplicity[a]
Per-emb 22 B	0.″64 × 0.″39	0.″95 × 0.″51	0.″72 × 0.″34	16.°0 ± 11.°0	0.92	
Per-emb 22 A	0.″64 × 0.″39	0.″86 × 0.″65	0.″64 × 0.″47	49.°0 ± 18.°0	1.71	
L1448 NW	0.″64 × 0.″39	0.″83 × 0.″47	0.″55 × 0.″25	22.°6 ± 5.°5	3.15	binary
Per-emb 33 B/C	0.″64 × 0.″39	0.″75 × 0.″48	0.″42 × 0.″28	24.°0 ± 76.°0	5.55	binary
Per-emb 33 A	0.″64 × 0.″39	0.″73 × 0.″45	0.″38 × 0.″24	172.°0 ± 19.°0	10.33	
L1448 IRS 3A	0.″64 × 0.″39	0.″85 × 0.″59	0.″65 × 0.″32	135.°4 ± 4.°3	3.21	
Per-emb 26	0.″64 × 0.″39	0.″69 × 0.″45	0.″31 × 0.″23	24.°0 ± 17.°0	8.03	
Per-emb 42	0.″64 × 0.″39	0.″64 × 0.″39	0.″17 × 0.″05	155.°0 ± 28.°0	0.66	
Per-emb 25	0.″64 × 0.″39	0.″69 × 0.″41	0.″32 × 0.″16	10.°5 ± 1.°5	5.27	
Per-emb 17	0.″64 × 0.″40	0.″79 × 0.″48	0.″53 × 0.″24	155.°5 ± 5.°2	2.00	binary
Per-emb 20	0.″64 × 0.″40	1.″29 × 0.″78	1.″13 × 0.″68	12.°1 ± 8.°9	0.14	
L1455 IRS 2	0.″64 × 0.″40	0.″60 × 0.″38	0.″21 × 0.″07[b]	…[b]	0.13	
Per-emb 35 A	0.″66 × 0.″42	0.″75 × 0.″51	0.″36 × 0.″29	9.°9 ± 82.°0	0.93	
Per-emb 35 B	0.″66 × 0.″42	0.″78 × 0.″53	0.″44 × 0.″30	24.°0 ± 25.°0	0.75	
Per-emb 27	0.″66 × 0.″42	0.″93 × 0.″66	0.″66 × 0.″50	9.°2 ± 13.°9	5.79	binary
EDJ2009-172	0.″66 × 0.″42	0.″69 × 0.″44	0.″20 × 0.″10	133.°0 ± 12.°0	0.62	
Per-emb 36	0.″66 × 0.″42	0.″73 × 0.″46	0.″31 × 0.″19	153.°4 ± 4.°0	5.56	binary
Per-emb 54	0.″66 × 0.″42	0.″69 × 0.″40	…[c]	…[c]	0.07	
SVS 13B	0.″66 × 0.″42	0.″87 × 0.″68	0.″56 × 0.″54	168.°0 ± 77.°0	6.64	
SVS 13A2	0.″66 × 0.″42	0.″86 × 0.″53	0.″55 × 0.″31	11.°0 ± 25.°0	0.61	
Per-emb 44	0.″66 × 0.″42	0.″98 × 0.″79	0.″72 × 0.″67	174.°0 ± 74.°0	6.84	binary
Per-emb 15	0.″66 × 0.″42	0.″89 × 0.″70	0.″60 × 0.″56	146.°0 ± 81.°0	0.17	
Per-emb 50	0.″66 × 0.″42	0.″73 × 0.″44	0.″30 × 0.″15	177.°2 ± 2.°1	4.13	
Per-emb 12 B	0.″66 × 0.″42	1.″33 × 0.″81	1.″19 × 0.″63	133.°7 ± 7.°3	10.04	
Per-emb 12 A	0.″66 × 0.″42	1.″11 × 0.″98	0.″91 × 0.″86	34.°0 ± 82.°0	21.85	
Per-emb 21	0.″66 × 0.″42	0.″74 × 0.″48	0.″34 × 0.″25	168.°0 ± 15.°0	2.05	
Per-emb 18	0.″66 × 0.″42	0.″84 × 0.″73	0.″73 × 0.″30	75.°0 ± 2.°0	3.42	binary
Per-emb 13	0.″66 × 0.″42	1.″07 × 0.″83	0.″91 × 0.″64	122.°1 ± 8.°0	14.76	
IRAS4B'	0.″66 × 0.″42	0.″83 × 0.″74	0.″61 × 0.″51	80.°0 ± 17.°0	7.13	
Per-emb 14	0.″66 × 0.″42	0.″79 × 0.″50	0.″46 × 0.″23	18.°6 ± 3.°3	3.05	
EDJ2009-235	0.″67 × 0.″42	0.″66 × 0.″44	0.″19 × 0.″13[b]	…[b]	0.26	
EDJ2009-237	0.″67 × 0.″42	0.″67 × 0.″42	0.″11 × 0.″05	132.°0 ± 55.°0	0.12	
Per-emb 37	0.″67 × 0.″42	0.″82 × 0.″57	0.″49 × 0.″38	155.°0 ± 28.°0	0.56	
Per-emb 60	0.″67 × 0.″42	0.″73 × 0.″47	0.″31 × 0.″20	15.°0 ± 74.°0	0.08	
Per-emb 5	0.″45 × 0.″30	0.″56 × 0.″41	0.″37 × 0.″27	22.°9 ± 5.°1	15.29	
Per-emb 2	0.″45 × 0.″30	1.″35 × 0.″97	1.″28 × 0.″93	175.°6 ± 3.°3	7.41	binary
Per-emb 10	0.″46 × 0.″30	0.″49 × 0.″32	0.″20 × 0.″14	161.°0 ± 19.°0	1.82	
Per-emb 40	0.″46 × 0.″30	0.″47 × 0.″32	0.″16 × 0.″09	38.°0 ± 13.°0	1.44	binary
Per-emb 29	0.″46 × 0.″30	0.″56 × 0.″39	0.″34 × 0.″26	170.°0 ± 34.°0	8.41	
B1-b N	0.″46 × 0.″30	0.″56 × 0.″47	0.″38 × 0.″33	87.°0 ± 25.°0	7.67	
B1-b S	0.″46 × 0.″30	0.″63 × 0.″53	0.″45 × 0.″42	108.°0 ± 28.°0	14.79	
Per-emb 16	0.″50 × 0.″32	0.″61 × 0.″52	0.″44 × 0.″41	86.°0 ± 58.°0	0.35	
Per-emb 28	0.″50 × 0.″32	0.″56 × 0.″32	0.″34 × 0.″14	3.°0 ± 6.°9	1.52	
Per-emb 1	0.″49 × 0.″32	0.″68 × 0.″48	0.″52 × 0.″36	20.°0 ± 22.°0	4.57	
Per-emb 11 B	0.″50 × 0.″33	0.″92 × 0.″69	0.″84 × 0.″58	39.°0 ± 24.°0	0.40	
Per-emb 11 A	0.″50 × 0.″33	0.″61 × 0.″48	0.″41 × 0.″38	14.°0 ± 72.°0	10.47	
Per-emb 11 C	0.″50 × 0.″33	1.″10 × 0.″86	1.″01 × 0.″79	141.°0 ± 57.°0	0.34	
Per-emb 55	0.″50 × 0.″32	0.″49 × 0.″33	0.″23 × 0.″10	36.°0 ± 34.°0	0.32	
Per-emb 8	0.″50 × 0.″32	0.″49 × 0.″36	0.″23 × 0.″19	65.°0 ± 24.°0	8.51	
Per-emb 53	0.″51 × 0.″33	0.″58 × 0.″42	0.″36 × 0.″31	150.°0 ± 17.°0	1.55	

Notes.
[a] The "binary" label indicates that the continuum source is an unsolved binary in our observations, according to Tobin et al. (2016).
[b] The deconvolved continuum source is a point source no larger than the listed size.
[c] The continuum cannot be deconvolved because the emission may be resolved in only one direction.

fitted shapes. The continuum emission peak appears as a compact circular or elliptical shape. Some sources show extended continuum emission resembling the shape of outflow cavities, such as Per-emb 22 A and B. The source velocities collected from the literatures agree with our observations. Three sources, EDJ2009-237, Per-emb 60, and EDJ2009-172, show no spectral line and no reliable measurement of source velocity in literature; therefore we excluded them from spectral extraction as well as from the line identification and modeling. However, these three sources still contribute to the total number of sources for characterizing detection statistics.

The observations resolved or marginally resolved 94% (47 of 50) of the continuum sources. Our sample includes single sources as well as resolved and unresolved multiple systems.

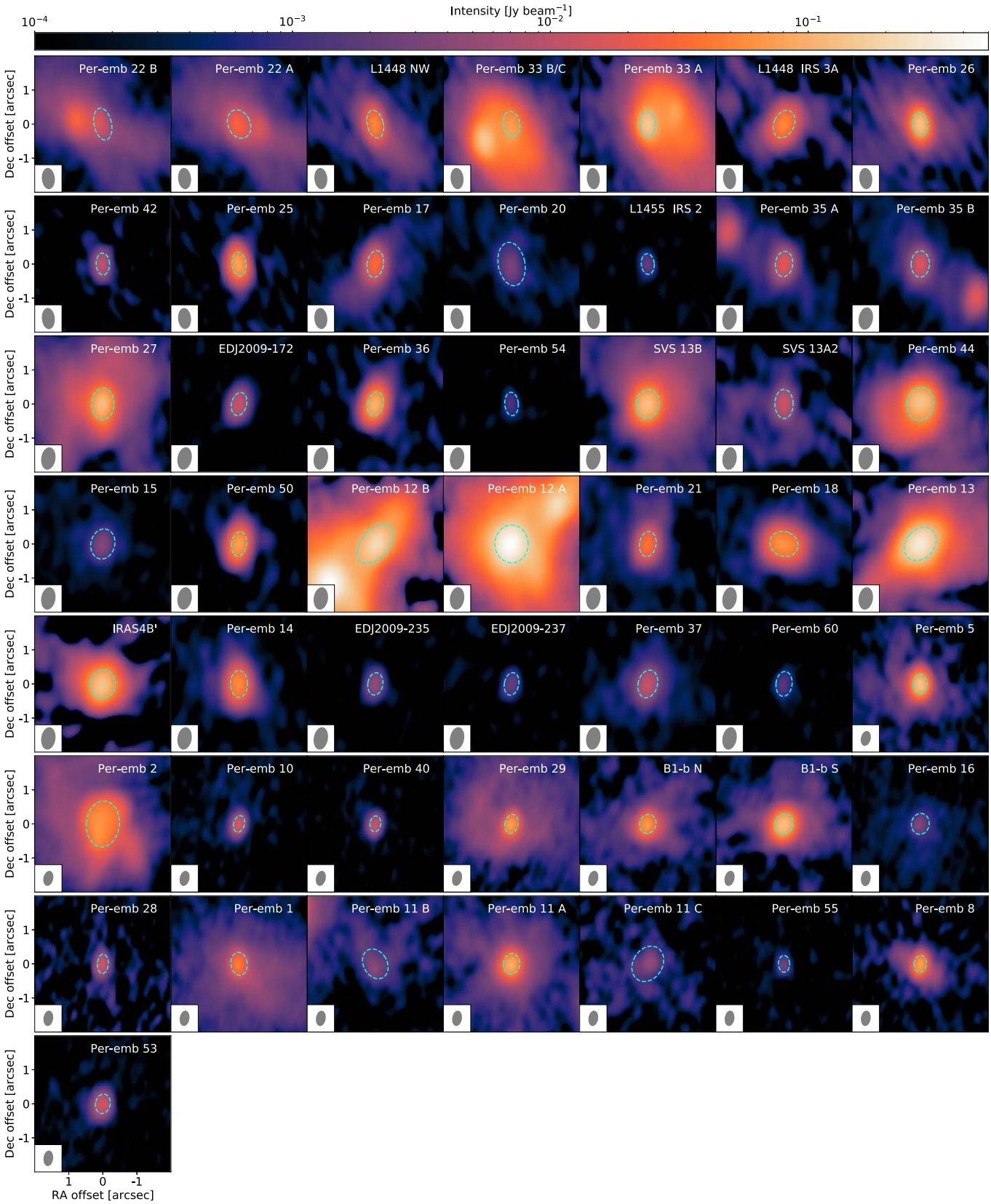

Figure 1. The continuum images of the PEACHES sample. Each panel is a zoom-in view of each continuum source with a size of $4''\times4''$ and has the same color scale. The corresponding beam size is shown in the lower left corner of each panel. Nondetections toward L1448 IRS 2E and NGC 1333 SVS 3 are not shown. EDJ2009-172, EDJ2009-237, and Per-emb 60 have no emission line. The dashed ellipses illustrate the size of the fitted continuum, which is the region in which 1D spectra are extracted.

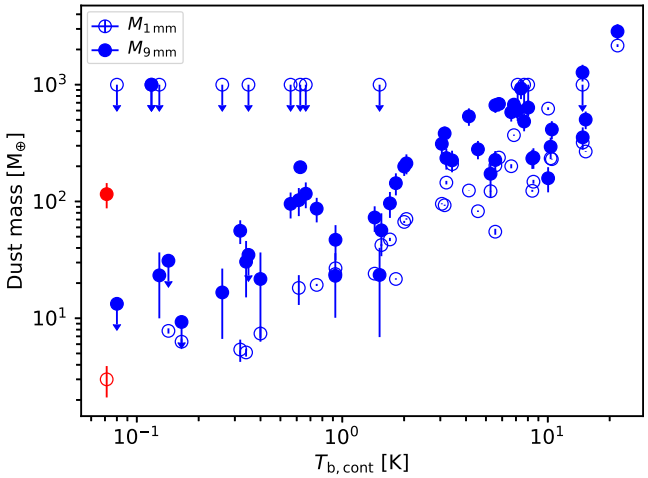

Figure 2. The averaged continuum brightness temperature compared with the masses derived with the 1 mm and 9 mm observations in opened and filled circles, respectively (Tychoniec et al. 2020). The red points highlight the mass of Per-emb 54 as an outlier of the linear trend with the 9 mm masses.

According to the VANDAM survey (Tobin et al. 2016), nine close binary systems remain unresolved in the PEACHES survey (Table 4).

The mean continuum brightness temperature ($T_{\rm b,cont}$) traces the optically thin dust mass; however, the dust emission from the center of protostars may be marginally optically thick at ALMA Band 6 (Ko et al. 2020), making the derived dust mass a lower limit. The $T_{\rm b,cont}$ of the PEACHES sample correlates with the dust mass of the disk-like structure of Perseus protostars derived from the 1 mm ALMA and 9 mm VLA observations (Tychoniec et al. 2020), except for that of Per-emb 54 (Figure 2). The 1 mm masses are systematically lower than the 9 mm masses because the inner disk-like structure becomes optically thick at 1 mm. Nonetheless, the $T_{\rm b,cont}$ increases linearly with the 1 mm masses with a similar slope as that with the 9 mm masses, suggesting that the $T_{\rm b,cont}$ traces the central mass without significant impact of the optical depth. The 1 mm mass of Per-emb 54 follows the linear trend, indicating that the deviation of its 9 mm mass may be due to excessive free–free emission.

Seven sources in our sample have $T_{\rm b,cont} > 10$ K (Table 4). Per-emb 12 A has a $T_{\rm b,cont}$ of 21.9 K, the brightest among our sample. In fact, the continuum opacity limits the detectability of COMs toward 4A1, where COMs show no emission or appear in absorption at ALMA Band 7 (López-Sepulcre et al. 2017; Sahu et al. 2019) and are observed in emission at centimeter wavelengths (De Simone et al. 2020). Toward the other six sources with $T_{\rm b,cont} > 10$ K, Per-emb 33 A, Per-emb 12 B, Per-emb 13, Per-emb 5, B1-b S, and Per-emb 11 A (see Section 3.2 and figures mentioned there), our observations detected several molecular lines from the central region, suggesting that the continuum opacity has less impact than that for Per-emb 12 A. Previous observations also suggest less impact from the continuum opacity for Per-emb 13 (Belloche et al. 2020) and B1-b S (Marcelino et al. 2018). Most of the sources have a mean brightness temperature lower than 10 K, while spatially resolved embedded disks tend to have a warm temperature, >20 K within a radius of 100–150 au (van't Hoff et al. 2018a, 2020a, 2020b). Thus the continuum source is likely to be unresolved and have an insignificant impact on the COMs emission at the angular resolution of this study. Note that some of the sources, such as Per-emb 18 and Per-emb 21, show a systematical shift of the peaks in multiple species. This could be understood by the high dust opacity at the continuum peak. However, correlations between the column density of COMs (Section 4.2.2) would be less affected because the dust opacity effect could be similar for all the species. We take the $T_{\rm b,cont}$ as a tracer of the averaged gas column densities, judging from a reasonable correction in Figure 2. Constraining the actual column densities requires higher resolution observations at multiple frequency bands and insights into the dust properties.

3.2. Spectral Extraction

The ALMA image cubes were post-processed to extract 1D spectra for identifying the emission of complex molecules and further analyses. Given the compact size of COM emission ($\lesssim$100 au) and the spatial resolution of $\sim$0.″5 ($\sim$150 au at 300 pc), we focused on the spectra toward the continuum sources to search for the COMs in the inner envelope. Figure 3 shows a representative sample of the COMs emission, while the maps for the rest of the sample are shown in the figure set. In most of the cases, COM emission is concentrated around the protostars at $\lesssim$300 au scale. Three steps of post-processing reduced the image cubes to 1D spectra. The steps are summarized below.

1. Extracting spectra: We used the CASA task `specflux` to extract the mean flux density within the ellipse that has the same major and minor axes as well as the position angle as the fitted continuum sources (see also the dashed ellipses in Figure 1).
2. Baseline subtraction: The continuum has been removed before the imaging process; however, the extracted spectra sometimes still show imperfect baselines due to the rich spectra of COMs and broad features. Thus, we manually selected the frequency ranges for baseline subtraction for each spectral window and each field.
3. Velocity correction: Finally, the frequencies of the extracted spectra were corrected according to the source velocities. We collected the source velocities from the literature as well as from the strong emission lines in our spectra, such as SO and CS. Table 2 lists the adopted source velocities and the corresponding references.

3.3. Line Identification

Line identification starts with manual identification and verification for a few sources with rich spectra, including Per-emb 12 B and B1-b S. Then, we tested the list of identified species to the rest of sources for identification. We used SPLATALOGUE[8] to identify the molecular species, where the molecular data come from the Cologne Database of Molecular Spectroscopy (CDMS; Müller et al. 2001, 2005; Endres et al. 2016) and the Jet Propulsion Laboratory Millimeter and Submillimeter Spectral Line Catalog (JPL; Pickett et al. 1998). Appendix A and Table A1 summarize the catalogs relevant for each species. Any tentatively identified species requires verification using synthetic spectra modeled with the XCLASS (Möller et al. 2017), which performs local thermodynamic equilibrium (LTE) radiative transfer calculations using the

[8] http://www.splatalogue.net/

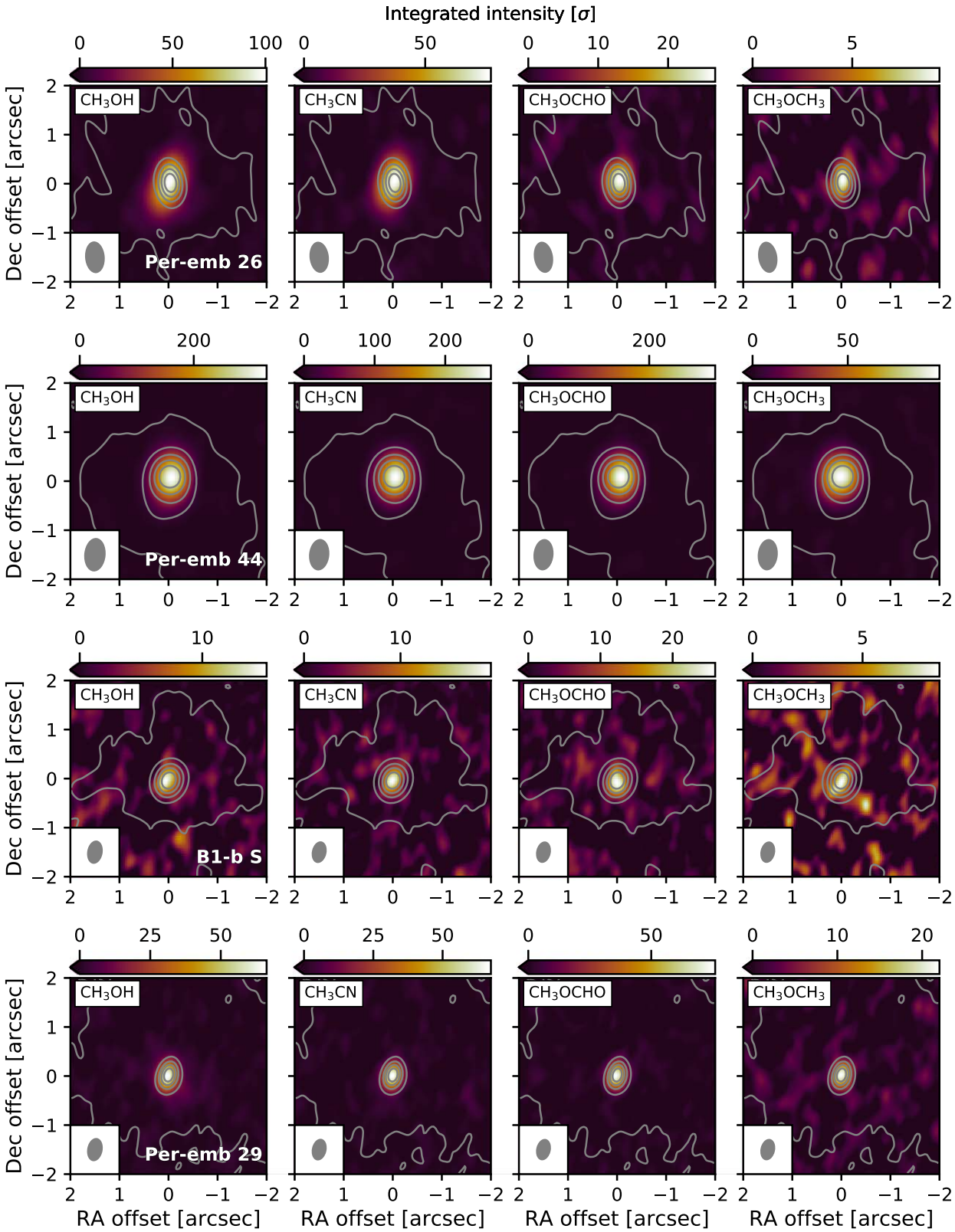

Figure 3. The intensity maps of the most frequently detected COMs, CH_3OH, $CH_3C^{15}N$, CH_3OCHO, and CH_3OCH_3 (from left to right) at selected sources. Each row shows the emission from Per-emb 26, Per-emb 44, B1-b S, and Per-emb 29 (top to bottom). The intensity is calculated by integrating over 3 km s^{-1} around the line centroid shown in the unit of the corresponding noise. The gray contours illustrate the continuum emission, with six contours linearly separated from 3σ to maximum intensity.

(The complete figure set (42 images) is available.)

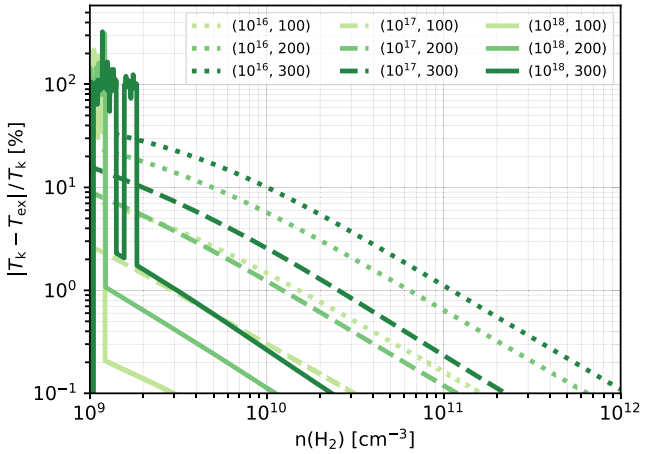

Figure 4. The difference between the excitation temperature (T_{ex}) and the kinetic temperature (T_k) normalized to T_k for the CH_3OH $2_{11} \rightarrow 1_{01}$ transition at 261805.68 MHz as a function of the number density of H_2 at different T_k. The calculations were performed using RADEX. The results with CH_3OH column densities of 10^{16}, 10^{17}, and 10^{18} cm^{-2} are shown as dotted, dashed, and solid lines, respectively, while the results with T_k of 100, 200, and 300 K are shown in decreasing transparency. The legends indicate the combination of N_{CH3OH} and T_k as (N_{CH3OH}, T_k).

molecular data from CDMS and JPL. We describe the details of the XCLASS modeling in Section 3.4. An identification needs to satisfy the following criteria:

1. The predicted strengths in synthetic spectra agree with the observations, assuming a fiducial column density that produces the observed intensity, an excitation temperature of 100 K, and a source size of 0.″5. Identification of a species requires an unblended line detected at a signal-to-noise ratio (S/N) > 3.
2. For each species, at least one spectral line is not blended with other emission. The emission of several species, such as HDCO & $^{13}CH_3OH$, CH_3OH & CH_3OCHO, CH_3CHO & CH_2DOH, ^{34}SO & C_2H_5OH, and CH_3OCH_3 & CH_2DCN, are partially blended (blending occurs at a few lines, but other lines remain isolated). The fittings of these species were performed together to verify their identification.
3. Identified molecules need to be already found toward young stellar objects, as summarized in McGuire (2018).

The identified species and transitions that are detected in at least one of the PEACHES sample are listed in Appendix B. Only identifiable transitions are listed. The XCLASS modeling includes all the transitions for the identified species in our frequency coverage so that we can test the relative strengths of different transitions in the identification process. Not all emission is identified; we reserve the analysis of the unidentified lines in future studies.

3.4. Modeling the Spectra of COMs

In addition to verifying the identification, we use XCLASS to model the observed spectra to constrain the column densities of COMs. XCLASS solves the radiative transfer equation for an isothermal source in 1D, called detection equation (Stahler & Palla 2004). The source brightness distribution follows a 2D Gaussian distribution, described by its full width at half maximum ($FWHM_{COM}$), the column density within $FWHM_{COM}$ (N_{COM}), and the excitation temperature (T_{ex}). The model has two additional parameters, the line width ($\Delta\nu$) and velocity offset (v_{off}), to calculate the spectra. For each species, XCLASS solves the radiative transfer equations independently. For a few species whose emission is blended at some frequencies, we fit them together in pairs, such as CH_3OH & CH_3OCHO, HDCO & $^{13}CH_3OH$, CH_3CHO & CH_2DOH, ^{34}SO & C_2H_5OH, and CH_3OCH_3 & CH_2DCN. We detect several simple molecules, such as CS, $H^{13}CN$, HDCO, SO, and SO_2. However, these lines often exhibit double-peaked or complex line profiles (see Figure 5 for an example) due to the self-absorption or contamination from the envelope and outflows, which will be analyzed in future studies. While our modeling includes these species to account for the weaker emission in the spectral coverage, we excluded these species from the following analysis because of the limitation of the simple LTE model.

To test the assumption of LTE, we ran 1D non-LTE models to estimate the discrepancy between the kinetic temperature (T_k) and the excitation temperature (T_{ex}) for the emission of CH_3OH, which often is the most abundant COM (e.g., Belloche et al. 2020). We followed a similar procedure as by Jørgensen et al. (2016) using RADEX, a 1D non-LTE radiative transfer package (van der Tak et al. 2007). The collision rates were taken from the Leiden Atomic and Molecular Database (Schöier et al. 2005) based on calculations by Rabli & Flower (2010). For one of the two most frequently detected CH_3OH transitions at 261805.68 MHz in our observations, T_k deviates from T_{ex} by more than 10% at $n(H_2) < 10^{10}$ cm^{-3}, or the CH_3OH column density $\lesssim 10^{16}$ cm^{-2} (Figure 4). The disagreement increases toward lower gas densities where the negative T_{ex}, indicative of a masing condition, causes the spikes in Figure 4. Assuming optically thin continuum emission, we estimated a gas density ranging from $\sim 4 \times 10^9 - 10^{12}$ cm^{-3} for the continuum sources in our sample (Appendix C). In this range, T_k agrees with T_{ex} within 10%–30%. Our calculations for the CH_3OH line at 243915.79 MHz show a maximum difference smaller than 0.1% for the combinations of parameters. The 243915.79 MHz CH_3OH line has $\Delta K = 0$ so that it is not a maser line, which requires $\Delta K \neq 0$. Therefore LTE is a valid assumption for modeling the spectra of COMs.

Our observations cover one transition or a few transitions for each species, making the determination of excitation temperature uncertain. Thus, instead of choosing an excitation temperature, we optimized the model with five different T_{ex}, 100, 150, 200, 250, and 300 K. Then, we took the mean and the range of fitted column density as the best-fit value and the corresponding uncertainty, respectively. For the COMs with A- and E-species due to the nuclear spins, such as CH_3OH and CH_3CN, we assumed that the A- and E-species have the same excitation temperature so that they can be modeled together. These T_{ex} cover the typical range of T_{ex} for the COMs detected toward embedded protostars (e.g., Bergner et al. 2019). We derived a similar range of T_{ex} for the species that have multiple detected transitions, such as CH_3OH and CH_3OCHO (Appendix D), suggesting that the range of 100–300 K represents the typical T_{ex} of COMs in the PEACHES sample. Therefore we can take the range of the derived column densities as an estimate of the true column density without fine-tuning the model for each source. To have a robust fitting result, we fixed $FWHM_{COM}$ to 0.″5 and assumed $v_{off} = 0$. We also assumed a negligible dust optical depth, making the fitted column density a lower limit if the dust opacity turns out to be

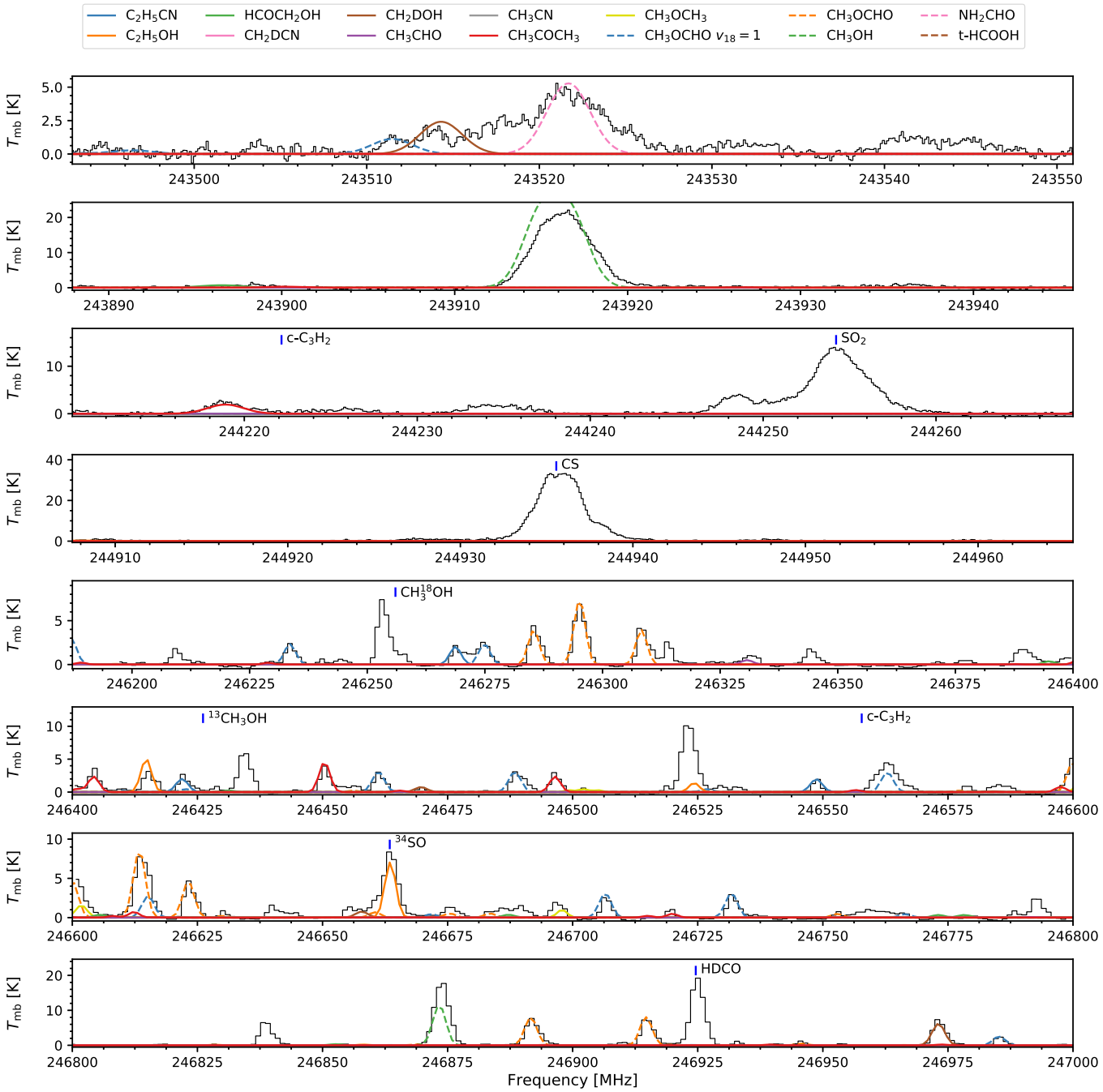

Figure 5. The spectra of Per-emb 44 (SVS 13 A) along with the best-fitting model assuming $T_{ex} = 150$ K. The fitted spectra for each species are illustrated by colored lines (solid and dashed) with the legends shown at the top of the figure. The frequencies of identifiable simple organic species, carbon-chain molecules, and the blended COMs emission, such as $^{13}CH_3OH$ and $CH_3^{18}OH$, are shown as blue vertical bars with the species listed next to it.

substantial. The synthetic spectra were calculated for the size of continuum emission (Table 2) to include the effect of beam dilution. We allowed the line width to vary between 1.2 and 3.5 km s^{-1} for a better fitting quality and chose a range of the column density for each molecule according to the strength of the emission.

The fitting function in XCLASS includes several optimization algorithms that can be used in sequence to reduce biases. We configured the algorithm chain that starts with the genetic algorithm followed by the Levenberg–Marquardt χ^2 minimization. The genetic algorithm iteratively searches for the best-fitting parameters with generations that evolve like a natural selection, where the better fitting models are modified less over generations. We set up the genetic algorithm to search for the top two best-fitting models with 30 generations. Then, the Levenberg–Marquardt χ^2 minimization was applied to the two best-fitting models for 20 iterations to determine the best-fitting models. The genetic algorithm aims to find global minima, and the Levenberg–Marquardt χ^2 minimization further finds the best-fitting models in the global minimums. The two best-fitting models found by the genetic algorithm are often very similar, suggesting that there is only one minimum. In the rare cases of two distinct global minima, we selected the model with the lower χ^2 values from the two best-fitting models constrained by the Levenberg–Marquardt

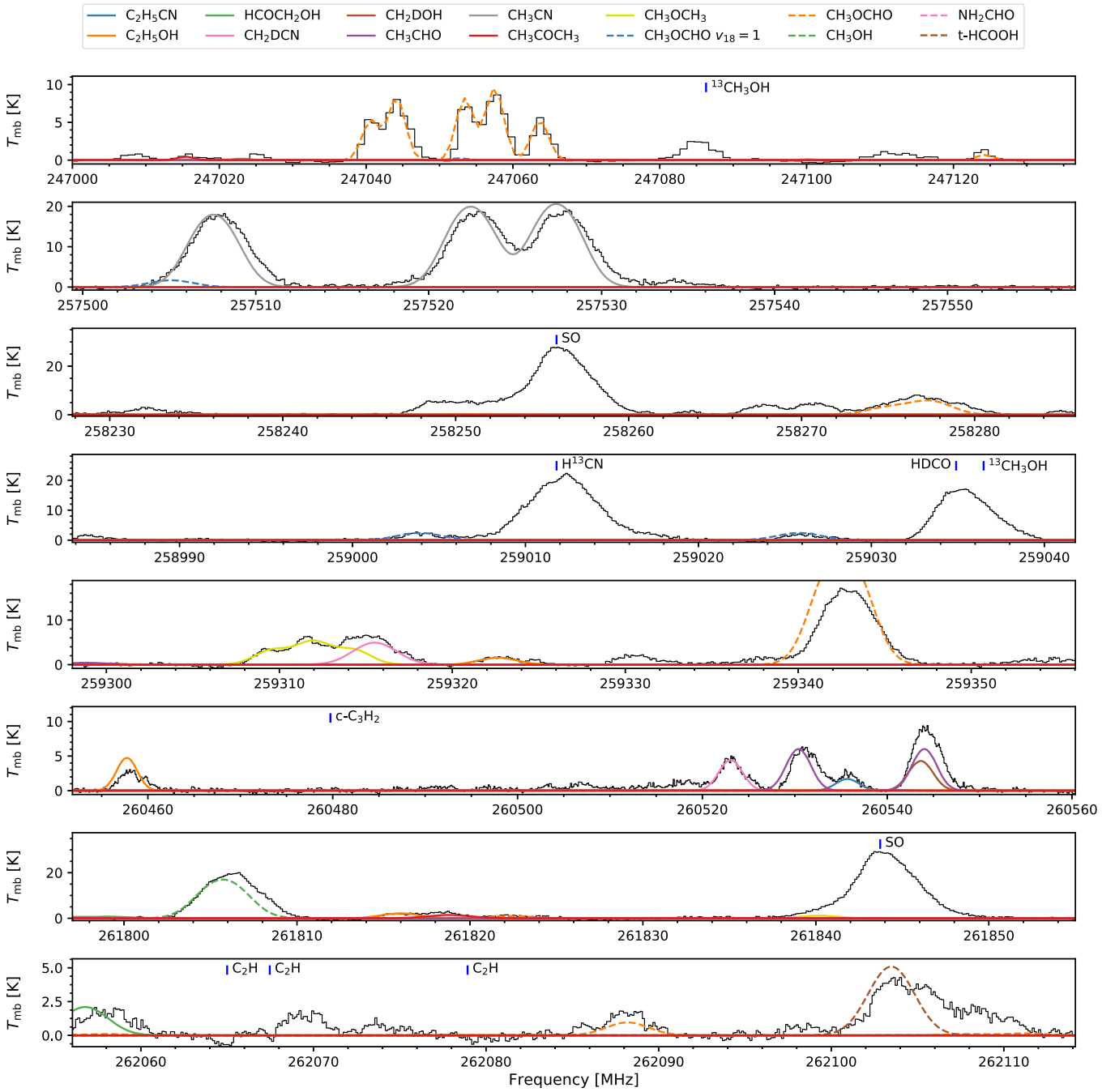

Figure 5. (Continued.)

χ^2 minimization. We allowed the column density to vary by a few orders of magnitude to ensure that a global minimum was found.

From the five fitted column densities assuming five different T_{ex}, if a molecule is detected according to the criteria listed in Section 3.3, we took the mean column densities as the best-fitting column density, while the range of the column densities indicates the uncertainty. If a species is considered nondetected (Section 3.3), we used the synthetic spectra to derive the upper limit of the column density corresponding to the noise of the spectra. The fitted column density assumes an FWHM of 0.″5 (150 au). Figure 5 shows an example of the fitted spectra for Per-emb 44 (SVS 13 A), assuming $T_{ex} = 150$ K. The fitted spectra may under- or overestimate the strengths of some transitions because the assumed excitation temperature may not be the true excitation temperature.

To benchmark this hybrid optimization process, we compared the fitted column densities with the fitting using the Monte Carlo Markov chain (MCMC) algorithm on the most chemically rich source, Per-emb 44 (SVS 13 A). The MCMC algorithm uses the affine-invariant MCMC package EMCEE (Foreman-Mackey et al. 2013) to sample the parameter space. In this MCMC optimization, we fit both the excitation temperature and the column density. For a single-species fitting, we used 100 walkers with 100 iterations after 30 burn-in iterations; for a combined fitting of two species,

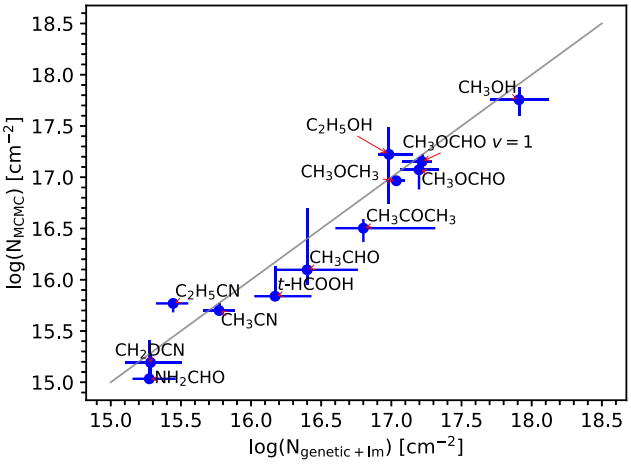

Figure 6. The column densities of Per-emb 44 (SVS 13 A) fit using the hybrid algorithm, genetic and Levenberg–Marquardt χ^2 minimization, and the MCMC algorithm. The molecular species are annotated, and the gray line indicates the equality.

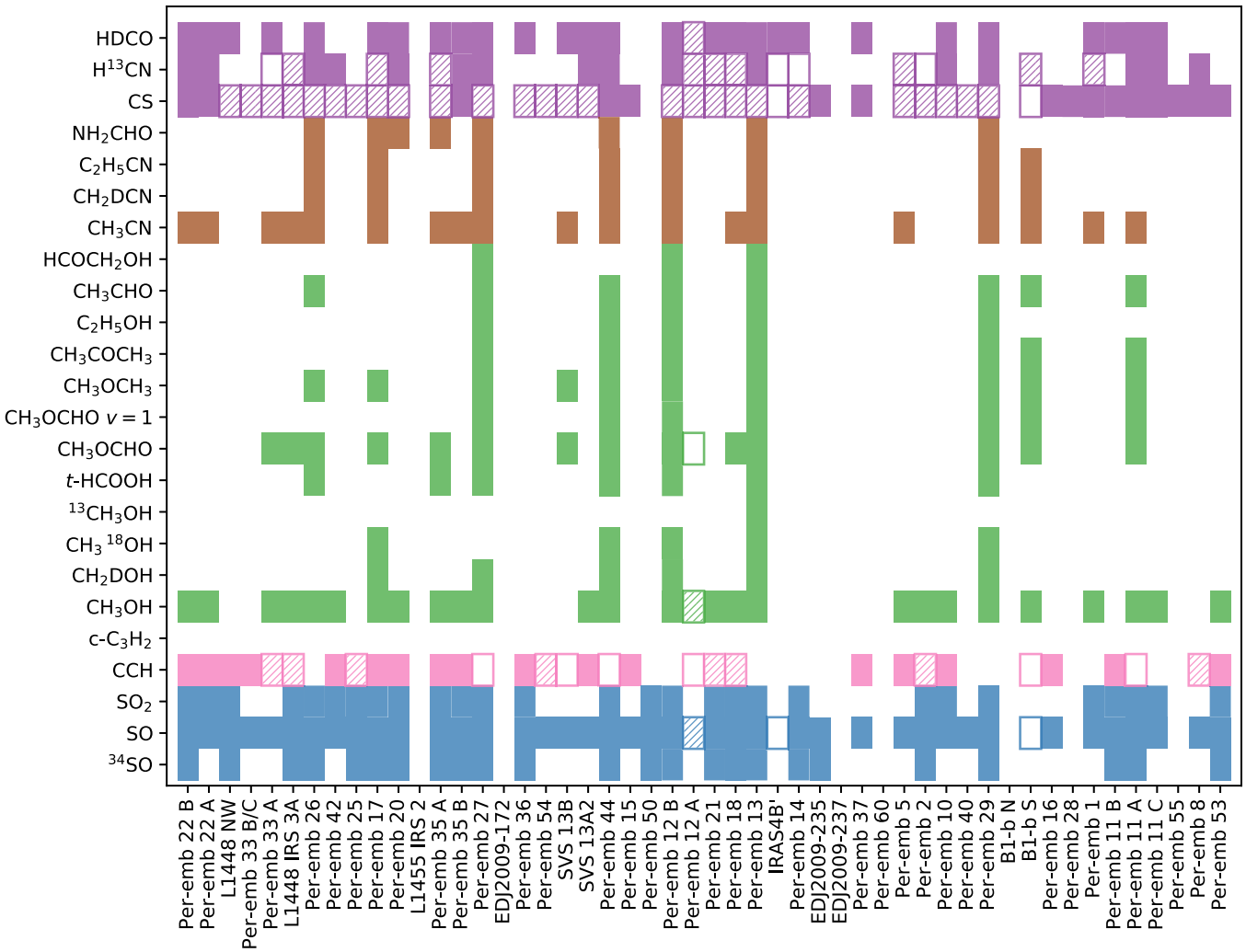

Figure 7. Summary of molecular detections. The sources are sorted by increasing R.A. from left to right. The detections are color-coded by the types of species: S-bearing molecules in blue, carbon-chain molecules in pink, O-bearing COMs in green excluding N-bearing molecules, N-bearing COMs in brown, and other simple organics in dark purple. The boxes with solid colors indicate emission and the empty boxes indicate absorption. The hatched boxes indicate both emission and absorption are seen.

we used 500 walkers to better sample the parameter space. The fitting column densities from the hybrid (genetic and Levenberg–Marquardt χ^2 minimizations) method are consistent with that fit with the MCMC optimization (Figure 6). Moreover, our hybrid method yields comparable uncertainties to those from the MCMC method, validating our modeling approach.

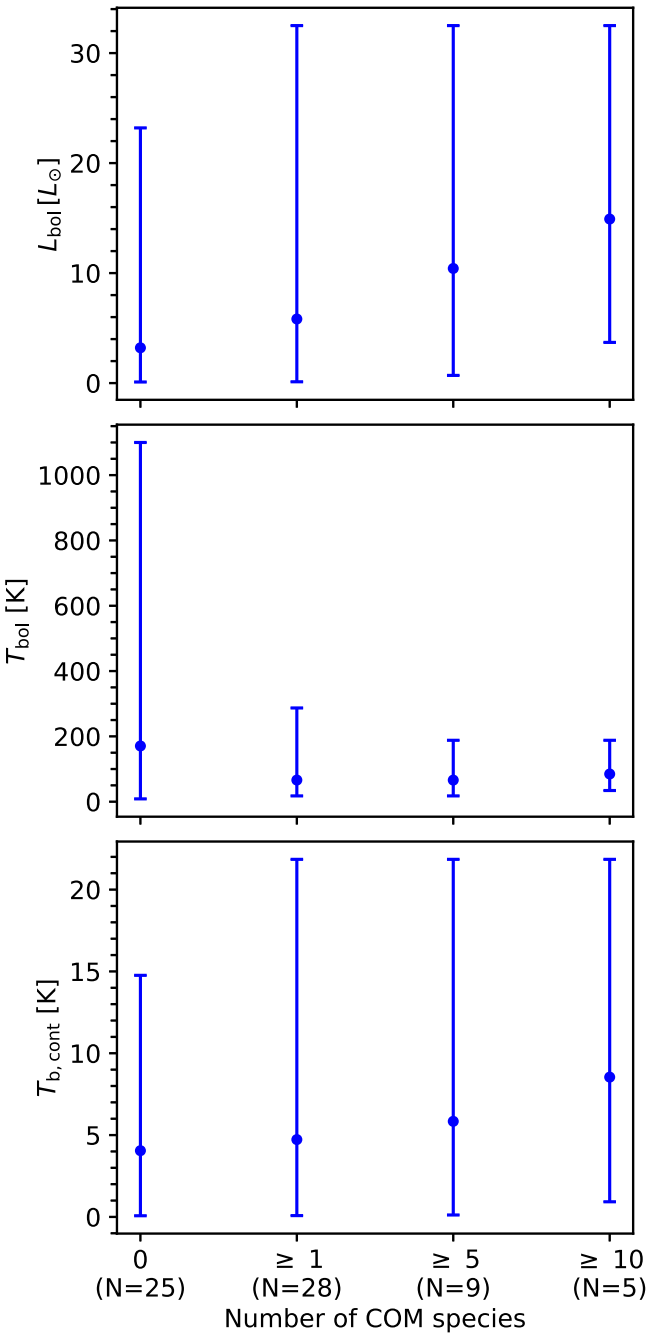

Figure 8. The number of COMs detected toward the PEACHES sample compared with the bolometric luminosity (L_{bol}), the bolometric temperature (T_{bol}), and the averaged continuum brightness temperature ($T_{b,cont}$) from top to bottom. The sample is divided into four groups with detected COM species of 0, $\geqslant 1$, $\geqslant 5$, and $\geqslant 10$, respectively. For each group, the circles show the mean values of the corresponding properties, while the error bars show the value ranges. The number of sources in each group is labeled in parentheses. L_{bol} and T_{bol} are taken from Tobin et al. (2016) and Murillo et al. (2016).

4. Results

4.1. Detection Statistics

We summarize the detection statistics in Figure 7, which includes COMs, carbon-chain molecules, and simple molecules, such as CS, $H^{13}CN$, SO, ^{34}SO, and SO_2. To derive the detection fraction, we included the three sources that were excluded from modeling because their source velocity was not reliable (Section 3.1), making a total of 50 sources. The COMs discussed here are derived from the spectra taken from the area surrounding the continuum peak, as explained in Section 3.1. We focus on the chemistry of COMs toward the disk-forming regions in this study. Therefore this study excludes any molecules that are only detected outside the region of continuum emission. A comparison of the chemical composition in protostellar envelopes (100–1000 au) requires observations with a larger maximum recoverable scale (θ_{MRS}).

The PEACHES sample shows a diverse chemistry of COMs, from no molecule detected (e.g., B1-b N and L1455 IRS 2) to rich spectra of COMs (e.g., Per-emb 13). Most protostars of the PEACHES sample have simple molecules, such as SO, CS, $H^{13}CN$, and HDCO, and ∼60% of the sources have SO_2 and ^{34}SO. Emission of C_2H can be easily identified from the spectra. However, C_2H toward the continuum sources often shows irregular line profiles together with velocity offsets and absorption (Appendix E, Figure 21). Warm environments, such as the outflow cavity wall, easily enhance the abundance of C_2H because of the elevated abundance of C^+ (e.g., Zhang et al. 2018; Imai et al. 2019). Thus, C_2H emission tends to extend along with the outflow cavities, which means that 1D spectra toward the continuum source are no longer representative of the abundance of C_2H. Future studies will investigate the comparison between unsaturated species and COMs using follow-up observations with a higher dynamic range of the spatial distribution (from ∼100 au to several 1000 au scale). Previous observations with single-dish telescopes have a beam size of ∼3000 au (e.g., Higuchi et al. 2018). Thus, observations that fill in the spatial scale from several 100 au to 1000 au are necessary.

Several sources have broad SiO emission, significantly contaminating the emission of CH_3CH_2CN and CH_3CHO. In comparison, the emission of COMs has relatively narrow line width of a few km s^{-1}. In the quantitative discussion below, we exclude the spectral windows that are contaminated by the SiO emission. For a few sources, such as Per-emb 26, we can still distinguish the emission of CH_3CH_2CN and CH_3CHO from the broad SiO emission and include these identification in the detection statistics.

Figure 7 shows the number of COMs detected toward the PEACHES sample. Twenty-nine (58%) sources have detected COMs. CH_3OH is detected in 28 sources (56%), CH_3OCHO is detected in 14 sources (28%), and N-bearing COMs are detected in 20 sources (40%). Compared to the COMs in the CALYPSO survey (Belloche et al. 2020), the fraction of sources that have methanol, ∼50%, is similar to that for the PEACHES sample. Furthermore, 30% of the CALYPSO sources have at least three species of COMs, while 28% of the PEACHES sample have at least three species of COMs. In a smaller sample selected from several molecular clouds, van Gelder et al. (2020) found that 3 of 7 protostars show emission of COMs.

To investigate the impact of protostellar properties on the appearance of COMs, we divided the PEACHES sample into four groups according to the number of detected COMs from no COM, at least 1, 5, and 10 species of COMs (Figure 8). The compared protostellar properties include the bolometric luminosity (L_{bol}), the bolometric temperature (T_{bol}), and the mean continuum brightness temperature ($T_{b,cont}$), where the T_{bol} and L_{bol} are collected from Tobin et al. (2016) and Murillo et al. (2016). T_{bol} traces the evolutionary stage of protostars with higher T_{bol} for more evolved protostars (Myers & Ladd 1993;

Table 5
Column Densities of Molecules

Source	CH_3OH	CH_3CN	CH_3OCHO	CH_3OCH_3	CH_3CHO	C_2H_5OH
L1448 NW	$2.1^{+0.7}_{-0.1} \times 10^{15}$	$<1.0 \times 10^{14}$	$<1.4 \times 10^{15}$	$<4.8 \times 10^{15}$	$<6.9 \times 10^{14}$	$<3.3 \times 10^{15}$
Per-emb 33 A	$5.3^{+1.9}_{-2.8} \times 10^{15}$	$8.5^{+4.3}_{-3.5} \times 10^{13}$	$1.3^{+0.4}_{-0.5} \times 10^{15}$	$<6.1 \times 10^{15}$	$<5.2 \times 10^{14}$	$<1.4 \times 10^{15}$
Per-emb 33 B/C	$<3.9 \times 10^{15}$	$<9.8 \times 10^{13}$	$<1.2 \times 10^{15}$	$<1.2 \times 10^{16}$	$<8.5 \times 10^{14}$	$<1.3 \times 10^{15}$
L1448 IRS 3A	$8.4^{+4.5}_{-5.3} \times 10^{15}$	$1.7^{+0.8}_{-0.7} \times 10^{14}$	$2.3^{+0.1}_{-0.9} \times 10^{15}$	$<9.9 \times 10^{15}$	$<3.3 \times 10^{14}$	$<2.5 \times 10^{15}$
Per-emb 26	$8.9^{+3.2}_{-4.4} \times 10^{16}$	$1.5^{+0.7}_{-0.6} \times 10^{15}$	$1.0^{+0.5}_{-0.5} \times 10^{16}$	$5.9^{+0.2}_{-1.0} \times 10^{15}$	$<2.4 \times 10^{15}$	$<2.1 \times 10^{15}$
Per-emb 42	$9.0^{+4.6}_{-5.4} \times 10^{15}$	$<4.1 \times 10^{13}$	$<1.1 \times 10^{15}$	$<1.2 \times 10^{16}$	$<4.5 \times 10^{14}$	$<4.4 \times 10^{15}$
Per-emb 22 A	$2.0^{+1.1}_{-1.2} \times 10^{16}$	$1.8^{+0.9}_{-0.8} \times 10^{14}$	$<1.4 \times 10^{15}$	$<4.0 \times 10^{15}$	$<3.3 \times 10^{14}$	$<2.7 \times 10^{15}$
Per-emb 22 B	$1.6^{+0.7}_{-1.0} \times 10^{16}$	$1.6^{+0.7}_{-0.7} \times 10^{14}$	$<1.0 \times 10^{15}$	$<6.7 \times 10^{15}$	$<1.4 \times 10^{13}$	$<1.5 \times 10^{15}$
Per-emb 25	$<4.6 \times 10^{15}$	$<1.2 \times 10^{14}$	$<2.0 \times 10^{15}$	$<1.0 \times 10^{16}$	$<5.6 \times 10^{14}$	$<3.0 \times 10^{15}$
Per-emb 20	$1.3^{+0.8}_{-0.8} \times 10^{16}$	$<7.4 \times 10^{13}$	$<8.7 \times 10^{14}$	$<5.1 \times 10^{14}$	$<1.5 \times 10^{14}$	$<2.8 \times 10^{15}$
L1455 IRS 2	$<4.4 \times 10^{15}$	$<1.2 \times 10^{14}$	$<1.5 \times 10^{15}$	$<5.6 \times 10^{15}$	$<4.9 \times 10^{14}$	$<2.6 \times 10^{15}$
Per-emb 44	$8.1^{+5.0}_{-3.1} \times 10^{17}$	$5.9^{+1.8}_{-1.3} \times 10^{15}$	$1.6^{+0.6}_{-0.4} \times 10^{17}$	$1.1^{+0.2}_{-0.1} \times 10^{17}$	$2.5^{+1.7}_{-1.4} \times 10^{16}$	$9.6^{+1.8}_{-3.1} \times 10^{16}$
SVS 13A2	$6.9^{+4.5}_{-4.6} \times 10^{15}$	$<7.5 \times 10^{13}$	$<1.1 \times 10^{15}$	$<2.4 \times 10^{15}$	$<5.5 \times 10^{14}$	$<2.0 \times 10^{15}$
Per-emb 12 A	$7.3^{+6.4}_{-4.9} \times 10^{15}$	$<5.4 \times 10^{13}$	$1.3^{+0.1}_{-0.7} \times 10^{14}$	$<6.8 \times 10^{15}$	$<6.0 \times 10^{14}$	$<1.4 \times 10^{15}$
Per-emb 12 B	$2.0^{+1.0}_{-0.1} \times 10^{17}$	$2.9^{+1.1}_{-1.0} \times 10^{15}$	$9.2^{+3.6}_{-3.0} \times 10^{16}$	$5.1^{+0.9}_{-0.7} \times 10^{16}$	$1.7^{+0.1}_{-0.9} \times 10^{16}$	$5.2^{+1.2}_{-1.1} \times 10^{16}$
Per-emb 13	$5.0^{+3.3}_{-3.2} \times 10^{16}$	$7.3^{+3.2}_{-2.5} \times 10^{14}$	$3.7^{+1.6}_{-1.4} \times 10^{16}$	$2.9^{+0.6}_{-0.4} \times 10^{16}$	$1.1^{+0.6}_{-0.6} \times 10^{16}$	$1.5^{+0.4}_{-0.3} \times 10^{16}$
IRAS4B'	$<3.5 \times 10^{14}$	$<3.9 \times 10^{13}$	$<9.6 \times 10^{14}$	$<4.8 \times 10^{15}$	$<1.5 \times 10^{15}$	$<1.7 \times 10^{15}$
Per-emb 27	$1.1^{+0.1}_{-0.5} \times 10^{18}$	$6.5^{+2.1}_{-1.3} \times 10^{15}$	$8.4^{+3.6}_{-1.9} \times 10^{16}$	$5.7^{+0.1}_{-1.0} \times 10^{16}$	$2.9^{+1.8}_{-1.6} \times 10^{16}$	$4.8^{+1.3}_{-2.3} \times 10^{16}$
Per-emb 54	$<2.3 \times 10^{15}$	$<8.4 \times 10^{13}$	$<1.1 \times 10^{15}$	$<4.9 \times 10^{15}$	$<6.1 \times 10^{14}$	$<2.7 \times 10^{15}$
Per-emb 21	$1.7^{+0.8}_{-1.0} \times 10^{16}$	$<8.2 \times 10^{13}$	$<1.2 \times 10^{15}$	$<4.4 \times 10^{15}$	$<3.2 \times 10^{14}$	$<3.5 \times 10^{15}$
Per-emb 14	$<3.3 \times 10^{15}$	$<3.1 \times 10^{13}$	$<9.9 \times 10^{14}$	$<4.2 \times 10^{15}$	$<7.8 \times 10^{13}$	$<1.9 \times 10^{15}$
Per-emb 35 A	$5.3^{+2.2}_{-2.9} \times 10^{16}$	$5.0^{+2.5}_{-2.1} \times 10^{14}$	$2.0^{+0.9}_{-0.7} \times 10^{15}$	$<9.0 \times 10^{15}$	$<2.6 \times 10^{14}$	$<2.9 \times 10^{15}$
Per-emb 35 B	$6.3^{+3.0}_{-3.5} \times 10^{15}$	$6.9^{+3.5}_{-2.9} \times 10^{13}$	$<1.3 \times 10^{15}$	$<1.1 \times 10^{15}$	$<8.1 \times 10^{14}$	$<3.3 \times 10^{15}$
SVS 13B	$<2.4 \times 10^{15}$	$3.0^{+1.5}_{-1.1} \times 10^{13}$	$9.4^{+4.2}_{-3.2} \times 10^{14}$	$5.2^{+1.7}_{-1.0} \times 10^{15}$	$<4.1 \times 10^{15}$	$<1.6 \times 10^{15}$
Per-emb 15	$<2.8 \times 10^{15}$	$<5.5 \times 10^{13}$	$<1.1 \times 10^{15}$	$<3.9 \times 10^{15}$	$<3.6 \times 10^{14}$	$<2.0 \times 10^{15}$
Per-emb 50	$<2.2 \times 10^{15}$	$<5.9 \times 10^{13}$	$<1.5 \times 10^{15}$	$<4.0 \times 10^{14}$	$<8.4 \times 10^{14}$	$<3.7 \times 10^{15}$
Per-emb 18	$2.3^{+1.0}_{-0.1} \times 10^{16}$	$2.3^{+0.1}_{-1.0} \times 10^{14}$	$2.1^{+1.1}_{-1.1} \times 10^{15}$	$<5.8 \times 10^{15}$	$<5.3 \times 10^{14}$	$<1.2 \times 10^{15}$
Per-emb 37	$<1.3 \times 10^{15}$	$<2.3 \times 10^{13}$	$<1.2 \times 10^{15}$	$<9.0 \times 10^{14}$	$<4.7 \times 10^{14}$	$<1.2 \times 10^{15}$
EDJ2009-235	$<4.0 \times 10^{15}$	$<8.1 \times 10^{13}$	$<8.1 \times 10^{14}$	$<5.1 \times 10^{15}$	$<1.0 \times 10^{15}$	$<2.3 \times 10^{15}$
Per-emb 36	$<3.6 \times 10^{15}$	$<8.4 \times 10^{13}$	$<1.4 \times 10^{15}$	$<1.0 \times 10^{15}$	$<1.1 \times 10^{13}$	$<3.3 \times 10^{15}$
B1-b S	$1.5^{+0.1}_{-0.9} \times 10^{16}$	$3.2^{+1.6}_{-1.4} \times 10^{14}$	$1.4^{+0.4}_{-0.2} \times 10^{16}$	$2.0^{+0.3}_{-0.3} \times 10^{16}$	$2.1^{+1.5}_{-1.2} \times 10^{15}$	$<1.5 \times 10^{15}$
B1-b N	$<3.9 \times 10^{15}$	$<8.5 \times 10^{13}$	$<2.6 \times 10^{14}$	$<3.4 \times 10^{15}$	$<2.2 \times 10^{12}$	$<2.1 \times 10^{15}$
Per-emb 29	$9.0^{+6.3}_{-5.9} \times 10^{16}$	$1.1^{+0.5}_{-0.4} \times 10^{15}$	$5.9^{+0.1}_{-0.9} \times 10^{16}$	$2.8^{+0.9}_{-0.7} \times 10^{16}$	$2.1^{+1.2}_{-1.3} \times 10^{15}$	$3.6^{+1.3}_{-1.0} \times 10^{16}$
Per-emb 10	$2.7^{+1.3}_{-1.6} \times 10^{15}$	$<8.8 \times 10^{13}$	$<5.2 \times 10^{14}$	$<5.9 \times 10^{15}$	$<1.4 \times 10^{15}$	$<2.9 \times 10^{15}$
Per-emb 40	$<4.8 \times 10^{15}$	$<8.6 \times 10^{13}$	$<1.1 \times 10^{15}$	$<6.0 \times 10^{15}$	$<4.5 \times 10^{14}$	$<3.5 \times 10^{15}$
Per-emb 2	$3.1^{+0.9}_{-0.1} \times 10^{15}$	$<5.1 \times 10^{13}$	$<9.4 \times 10^{13}$	$<8.3 \times 10^{14}$	$<2.0 \times 10^{14}$	$<1.9 \times 10^{15}$
Per-emb 5	$9.9^{+4.7}_{-6.0} \times 10^{15}$	$1.8^{+0.8}_{-0.8} \times 10^{14}$	$<9.1 \times 10^{14}$	$<1.1 \times 10^{16}$	$<4.7 \times 10^{12}$	$<2.6 \times 10^{15}$
Per-emb 1	$8.9^{+3.8}_{-5.4} \times 10^{15}$	$6.2^{+3.1}_{-2.6} \times 10^{13}$	$<3.9 \times 10^{14}$	$<1.2 \times 10^{15}$	$<4.8 \times 10^{15}$	$<3.4 \times 10^{15}$
Per-emb 11 A	$9.1^{+5.3}_{-5.6} \times 10^{15}$	$1.4^{+0.7}_{-0.6} \times 10^{14}$	$7.3^{+1.7}_{-1.3} \times 10^{15}$	$3.4^{+0.4}_{-0.3} \times 10^{15}$	$8.4^{+3.7}_{-3.8} \times 10^{15}$	$<2.3 \times 10^{15}$
Per-emb 11 B	$<2.6 \times 10^{15}$	$<1.9 \times 10^{13}$	$<2.7 \times 10^{14}$	$<3.7 \times 10^{15}$	$<4.2 \times 10^{12}$	$<9.3 \times 10^{14}$
Per-emb 11 C	$6.4^{+3.9}_{-4.0} \times 10^{15}$	$<4.6 \times 10^{13}$	$1.1^{+0.2}_{-0.3} \times 10^{15}$	$<4.0 \times 10^{14}$	$<5.1 \times 10^{14}$	$<2.4 \times 10^{15}$
Per-emb 8	$<3.4 \times 10^{15}$	$<8.0 \times 10^{13}$	$<1.5 \times 10^{14}$	$<5.2 \times 10^{14}$	$<5.2 \times 10^{13}$	$<4.2 \times 10^{15}$
Per-emb 55	$<3.9 \times 10^{15}$	$<7.9 \times 10^{13}$	$<1.1 \times 10^{15}$	$<4.9 \times 10^{15}$	$<5.7 \times 10^{14}$	$<3.0 \times 10^{15}$
Per-emb 16	$<2.0 \times 10^{15}$	$<6.1 \times 10^{13}$	$<1.1 \times 10^{15}$	$<3.7 \times 10^{15}$	$<5.6 \times 10^{12}$	$<3.3 \times 10^{15}$
Per-emb 28	$<1.7 \times 10^{16}$	$<4.0 \times 10^{14}$	$<3.5 \times 10^{14}$	$<1.7 \times 10^{16}$	$<1.8 \times 10^{13}$	$<7.1 \times 10^{15}$
Per- emb 53	$5.1^{+2.9}_{-3.2} \times 10^{15}$	$<7.7 \times 10^{13}$	$<1.0 \times 10^{14}$	$<3.8 \times 10^{15}$	$<4.5 \times 10^{12}$	$<1.5 \times 10^{15}$

Source	CH_3OCHO $v = 1$	CH_3COCH_3	*t*-HCOOH	C_2H_5CN	NH_2CHO	CH_2DCN
L1448 NW	$<1.7 \times 10^{16}$	$<5.0 \times 10^{14}$	$<1.2 \times 10^{15}$	$<2.5 \times 10^{14}$	$<2.1 \times 10^{14}$	$<7.5 \times 10^{13}$
Per-emb 33 A	$<7.6 \times 10^{15}$	$<7.6 \times 10^{14}$	$<4.3 \times 10^{14}$	$<2.3 \times 10^{14}$	$<2.0 \times 10^{14}$	$<1.2 \times 10^{14}$
Per-emb 33 B/C	$<4.7 \times 10^{15}$	$<1.0 \times 10^{15}$	$<1.2 \times 10^{15}$	$<2.3 \times 10^{14}$	$<5.1 \times 10^{13}$	$<1.5 \times 10^{14}$
L1448 IRS 3A	$<9.0 \times 10^{15}$	$<5.2 \times 10^{14}$	$<9.8 \times 10^{14}$	$<2.0 \times 10^{14}$	$<9.4 \times 10^{13}$	$<7.3 \times 10^{13}$
Per-emb 26	$<1.2 \times 10^{16}$	$<9.8 \times 10^{14}$	$1.0^{+0.6}_{-0.5} \times 10^{15}$	$2.6^{+0.8}_{-0.5} \times 10^{14}$	$1.4^{+0.5}_{-0.5} \times 10^{14}$	$1.5^{+0.7}_{-0.6} \times 10^{14}$
Per-emb 42	$<5.3 \times 10^{15}$	$<1.3 \times 10^{15}$	$<1.2 \times 10^{15}$	$<2.7 \times 10^{14}$	$<2.3 \times 10^{14}$	$<1.1 \times 10^{14}$
Per-emb 22 A	$<1.4 \times 10^{16}$	$<3.9 \times 10^{13}$	$<7.8 \times 10^{14}$	$<1.4 \times 10^{14}$	$<1.8 \times 10^{14}$	$<1.3 \times 10^{14}$
Per-emb 22 B	$<9.4 \times 10^{15}$	$<9.9 \times 10^{14}$	$<1.0 \times 10^{15}$	$<2.3 \times 10^{14}$	$<1.9 \times 10^{14}$	$<6.7 \times 10^{13}$
Per-emb 25	$<4.3 \times 10^{15}$	$<1.2 \times 10^{15}$	$<9.4 \times 10^{14}$	$<1.9 \times 10^{14}$	$<8.9 \times 10^{13}$	$<1.4 \times 10^{14}$
Per-emb 20	$<8.0 \times 10^{15}$	$<4.9 \times 10^{14}$	$<3.8 \times 10^{14}$	$<1.8 \times 10^{14}$	$9.6^{+3.1}_{-3.6} \times 10^{13}$	$<8.6 \times 10^{13}$
L1455 IRS 2	$<1.1 \times 10^{16}$	$<5.6 \times 10^{14}$	$<1.4 \times 10^{15}$	$<2.7 \times 10^{14}$	$<7.7 \times 10^{13}$	$<7.9 \times 10^{13}$
Per-emb 44	$1.7^{+0.6}_{-0.2} \times 10^{17}$	$6.3^{+3.7}_{-4.4} \times 10^{16}$	$1.5^{+0.6}_{-0.7} \times 10^{16}$	$2.8^{+0.9}_{-0.6} \times 10^{15}$	$1.9^{+0.6}_{-0.7} \times 10^{15}$	$1.9^{+1.0}_{-0.8} \times 10^{15}$
SVS 13A2	$<3.3 \times 10^{15}$	$<7.9 \times 10^{14}$	$<6.3 \times 10^{14}$	$<2.1 \times 10^{14}$	$<1.9 \times 10^{14}$	$<1.2 \times 10^{14}$

Table 5
(Continued)

Source	CH_3OCHO $v=1$	CH_3COCH_3	*t*-HCOOH	C_2H_5CN	NH_2CHO	CH_2DCN
Per-emb 12 A	$<6.6\times10^{15}$	$<6.5\times10^{14}$	$<7.5\times10^{14}$	$<1.5\times10^{14}$	$<1.4\times10^{14}$	$<7.8\times10^{13}$
Per-emb 12 B	$1.1^{+0.3}_{-0.2}\times10^{17}$	$3.9^{+5.5}_{-3.0}\times10^{16}$	$9.1^{+4.8}_{-4.2}\times10^{15}$	$2.3^{+0.6}_{-0.5}\times10^{15}$	$1.1^{+0.4}_{-0.4}\times10^{15}$	$1.3^{+0.6}_{-0.5}\times10^{15}$
Per-emb 13	$3.8^{+0.1}_{-0.6}\times10^{16}$	$9.6^{+1.4}_{-7.8}\times10^{15}$	$1.4^{+0.8}_{-0.7}\times10^{15}$	$5.7^{+1.5}_{-1.2}\times10^{14}$	$2.3^{+0.8}_{-0.9}\times10^{14}$	$2.3^{+0.1}_{-0.9}\times10^{14}$
IRAS4B'	$<8.2\times10^{15}$	$<5.5\times10^{14}$	$<3.8\times10^{14}$	$<1.9\times10^{14}$	$<1.5\times10^{14}$	…[a]
Per-emb 27	$6.9^{+3.7}_{-1.2}\times10^{16}$	$3.0^{+4.3}_{-2.4}\times10^{16}$	$1.6^{+0.8}_{-0.7}\times10^{16}$	$3.1^{+0.1}_{-0.8}\times10^{15}$	$2.1^{+0.7}_{-0.8}\times10^{15}$	$1.4^{+0.7}_{-0.5}\times10^{15}$
Per-emb 54	$<1.6\times10^{16}$	$<1.0\times10^{15}$	$<4.0\times10^{14}$	$<2.4\times10^{14}$	$<2.4\times10^{14}$	$<1.0\times10^{14}$
Per-emb 21	$<1.4\times10^{16}$	$<9.0\times10^{14}$	$<3.5\times10^{14}$	$<2.2\times10^{14}$	$<2.1\times10^{14}$	$<4.3\times10^{13}$
Per-emb 14	$<1.5\times10^{16}$	$<7.4\times10^{14}$	$<9.8\times10^{14}$	$<1.2\times10^{14}$	$<1.2\times10^{14}$	$<8.8\times10^{13}$
Per-emb 35 A	$<8.8\times10^{15}$	$<8.0\times10^{14}$	$9.1^{+5.0}_{-4.5}\times10^{14}$	$<1.5\times10^{14}$	$1.3^{+0.4}_{-0.5}\times10^{14}$	$<1.0\times10^{14}$
Per-emb 35 B	$<8.6\times10^{15}$	$<9.1\times10^{14}$	$<8.5\times10^{14}$	$<1.9\times10^{14}$	$<2.0\times10^{14}$	$<6.8\times10^{13}$
SVS 13B	$<1.9\times10^{15}$	$<7.6\times10^{14}$	$<2.4\times10^{14}$	$<1.7\times10^{14}$	$<5.3\times10^{13}$	…[a]
Per-emb 15	$<9.5\times10^{15}$	$<7.9\times10^{14}$	$<7.6\times10^{14}$	$<6.2\times10^{13}$	$<1.7\times10^{14}$	$<1.2\times10^{14}$
Per-emb 50	$<8.1\times10^{15}$	$<3.6\times10^{14}$	$<8.6\times10^{14}$	$<2.3\times10^{14}$	$<6.9\times10^{13}$	$<6.2\times10^{13}$
Per-emb 18	$<3.2\times10^{15}$	$<6.9\times10^{14}$	$<2.9\times10^{14}$	$<1.6\times10^{14}$	$<1.6\times10^{14}$	$<8.2\times10^{13}$
Per-emb 37	$<1.3\times10^{16}$	$<2.7\times10^{13}$	$<9.2\times10^{14}$	$<1.8\times10^{14}$	$<1.8\times10^{14}$	$<5.6\times10^{13}$
EDJ2009-235	$<1.5\times10^{16}$	$<1.1\times10^{15}$	$<1.1\times10^{15}$	$<2.5\times10^{14}$	$<1.6\times10^{14}$	$<8.1\times10^{13}$
Per-emb 36	$<4.6\times10^{15}$	$<6.8\times10^{14}$	$<5.8\times10^{14}$	$<1.5\times10^{14}$	$<1.1\times10^{14}$	$<8.2\times10^{13}$
B1-b S	$2.1^{+0.8}_{-0.3}\times10^{16}$	$6.4^{+8.8}_{-5.0}\times10^{15}$	$<7.8\times10^{14}$	$2.9^{+0.7}_{-0.7}\times10^{14}$	$<1.6\times10^{14}$	$2.2^{+0.1}_{-0.9}\times10^{14}$
B1-b N	$<8.5\times10^{15}$	$<9.5\times10^{14}$	$<3.7\times10^{14}$	$<1.7\times10^{14}$	$<2.0\times10^{14}$	$<1.1\times10^{14}$
Per-emb 29	$7.0^{+2.8}_{-1.1}\times10^{16}$	$2.5^{+3.7}_{-2.0}\times10^{16}$	$1.5^{+0.8}_{-0.7}\times10^{15}$	$1.5^{+0.4}_{-0.2}\times10^{15}$	$3.5^{+1.2}_{-1.3}\times10^{14}$	$5.3^{+2.6}_{-2.1}\times10^{14}$
Per-emb 10	$<1.9\times10^{16}$	$<1.3\times10^{15}$	$<1.4\times10^{15}$	$<2.7\times10^{14}$	$<2.2\times10^{14}$	$<2.2\times10^{14}$
Per-emb 40	$<2.0\times10^{16}$	$<1.3\times10^{15}$	$<1.4\times10^{15}$	$<2.9\times10^{14}$	$<2.4\times10^{14}$	$<1.0\times10^{14}$
Per-emb 2	$<8.6\times10^{15}$	$<6.0\times10^{14}$	$<2.3\times10^{14}$	$<1.3\times10^{14}$	$<1.2\times10^{14}$	$<8.7\times10^{13}$
Per-emb 5	$<1.5\times10^{16}$	$<1.0\times10^{15}$	$<1.1\times10^{15}$	$<1.8\times10^{14}$	$<1.8\times10^{14}$	$<1.6\times10^{14}$
Per-emb 1	$<7.1\times10^{15}$	$<8.3\times10^{14}$	$<3.3\times10^{14}$	$<2.2\times10^{14}$	$<1.7\times10^{14}$	…[a]
Per-emb 11 A	$8.7^{+3.8}_{-1.6}\times10^{15}$	$2.0^{+2.9}_{-1.6}\times10^{15}$	$<8.5\times10^{14}$	$<1.3\times10^{14}$	$<1.7\times10^{14}$	…[a]
Per-emb 11 B	$<1.1\times10^{16}$	$<6.8\times10^{14}$	$<2.6\times10^{14}$	$<6.0\times10^{13}$	$<1.3\times10^{14}$	$<4.8\times10^{13}$
Per- emb 11 C	$<5.5\times10^{15}$	$<3.8\times10^{14}$	$<6.3\times10^{14}$	$<1.5\times10^{14}$	$<1.1\times10^{14}$	$<3.5\times10^{13}$
Per-emb 8	$<2.0\times10^{16}$	$<5.6\times10^{14}$	$<1.1\times10^{15}$	$<3.0\times10^{14}$	$<1.9\times10^{14}$	$<9.6\times10^{13}$
Per-emb 55	$<1.4\times10^{16}$	$<1.3\times10^{15}$	$<1.1\times10^{15}$	$<1.9\times10^{14}$	$<6.1\times10^{13}$	$<1.8\times10^{14}$
Per-emb 16	$<1.3\times10^{16}$	$<5.2\times10^{14}$	$<7.8\times10^{14}$	$<1.3\times10^{14}$	$<1.4\times10^{14}$	$<8.1\times10^{13}$
Per-emb 28	$<3.4\times10^{16}$	$<2.0\times10^{15}$	$<4.5\times10^{15}$	$<1.3\times10^{15}$	$<8.5\times10^{14}$	$<2.9\times10^{14}$
Per-emb 53	$<8.1\times10^{15}$	$<1.6\times10^{14}$	$<6.7\times10^{14}$	$<1.2\times10^{14}$	$<1.5\times10^{14}$	$<5.4\times10^{13}$

Note. The column density is fitted with an aperture of $0''.5$.
[a] The column densities of molecules are unconstrained because the spectral window contaminated by the SiO emission is excluded.

Chen et al. 1995; Evans et al. 2009), and L_{bol} serves as a proxy of the size of the warm inner envelope as the accretion luminosity dominates the L_{bol} for Class 0/I protostars (Dunham et al. 2014). The number of detected COMs shows no obvious trend with L_{bol}, T_{bol}, and $T_{b,cont}$.

If the COMs mostly come from thermal desorption, the region with $T > T_{desorption}$ may be smaller for low-luminosity sources, resulting in fainter emission of COMs and reducing their detectability. In contrast to this expectation, the COMs detection shows no obvious trend with L_{bol}, except that the group with more COMs has a higher minimum L_{bol}. However, the range of L_{bol} in each group is much larger than the change in the minimum L_{bol}; thus, we cannot establish a significant correlation between the appearance of COMs and L_{bol}.

The high T_{bol} value for the sources without COM detection is driven by the high T_{bol} of EDJ2009-172 ($T_{bol} = 1100$ K), while the second highest T_{bol} for the group is L1455 IRS 2 with 740 K. The lower maximum T_{bol} for the sources with more detected COMs indicates that evolved sources may have fewer COMs in the gas phase. In the Ophiuchus molecular cloud, Artur de la Villarmois et al. (2019) reported no detection of CH_3OH toward a sample of Class I protostars either. If we take T_{bol} of 70 K as the boundary between Class 0 and I, our survey shows no obvious difference for the Class 0 and I sources; however, the evolutionary stage classified with T_{bol} may not represent the true evolutionary state of the protostar due to extinction and the effect of inclination (Launhardt et al. 2013; Dunham et al. 2014). The detectability of COMs may depend on other factors, such as the chemistry in the envelope scale, instead of the current physical condition. Thus, the chemo-physical history of protostars may play a dominant role in the chemistry of COMs (e.g., Garrod et al. 2008; Aikawa 2013; Aikawa et al. 2020).

Several COM-rich protostars in Perseus have been known previously (e.g., Bottinelli et al. 2004a, 2007; Sakai et al. 2006; Marcelino et al. 2018; Bianchi et al. 2019). Our survey detects more COMs in addition to the known CH_3OH toward Per-emb 35 A and Per-emb 11 A (Figure 8). Per-emb 35 A is in a binary system (NGC 1333 IRAS 1) together with Per-emb 35 B. Source A has emission of CH_3OH, CH_3CN, CH_3OCHO, and *t*-HCOOH, while Source B only has weak emission of CH_3OH, showing an apparent chemical differentiation. Per-emb 11 A is the brightest source in a wide triple system, where Per-emb 11 B is $\sim3''$ away toward the southwest and Per-emb 11 C is $\sim9''.5$ away toward the northeast (Tobin et al. 2016). Per-emb 11 A has rich spectra of COMs, including CH_3OCHO, CH_3OCH_3, CH_3COCH_3, CH_3CHO, and CH_3CN.

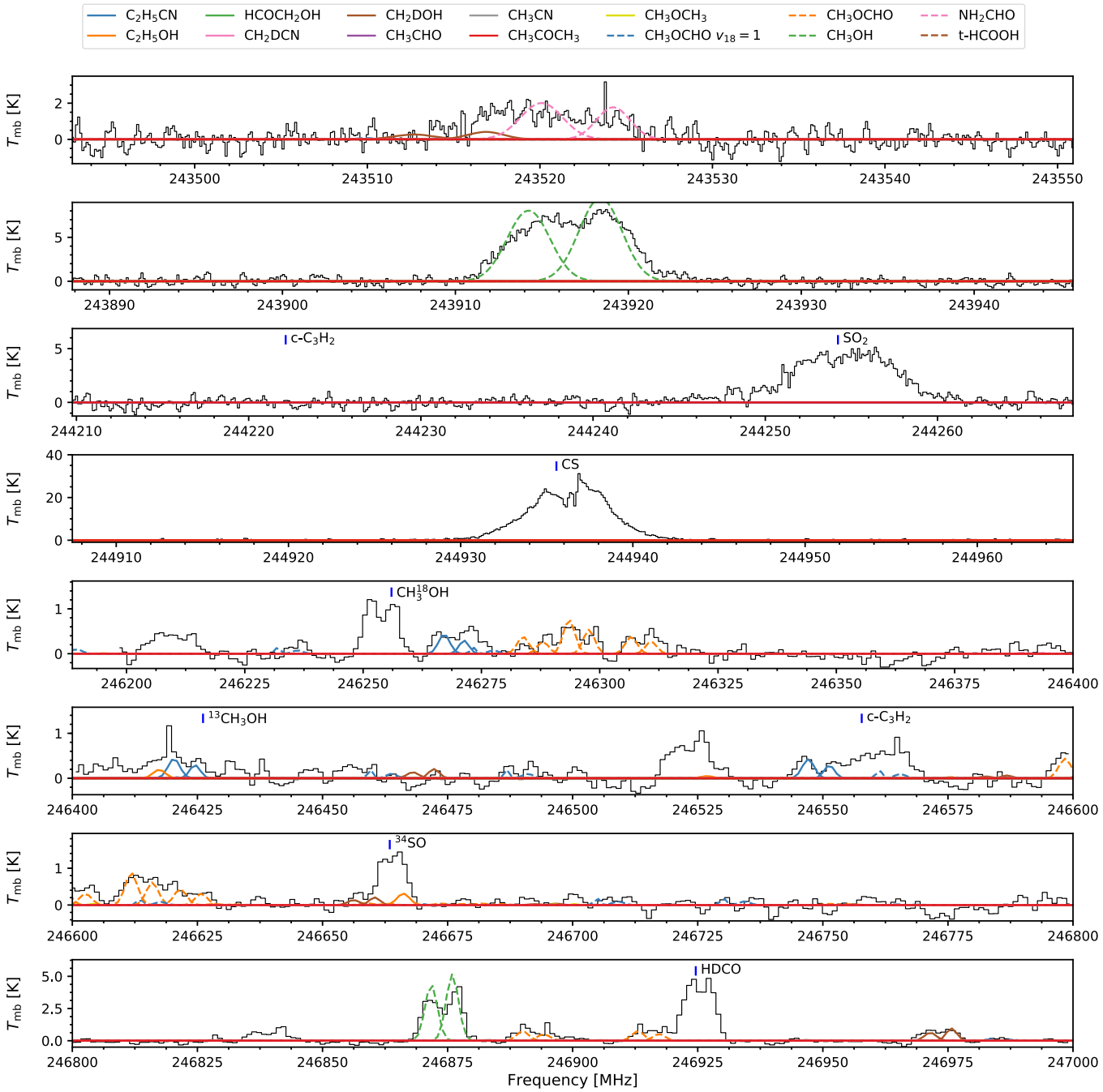

Figure 9. The spectra of Per-emb 17 along with the best-fitting model assuming $T_{ex} = 200$ K. The legends are similar to the legend in Figure 5, while each species has two velocity components at 1.96 km s^{-1}and -3.15 km s^{-1}.

Compact emission of COMs is consistent with an origin of thermal desorption at the inner envelope, the so-called hot corinos (Ceccarelli 2004). However, we cannot rule out other origins, such as local enhancement due to accretion shocks (Oya et al. 2016), because our observations only marginally resolved most of the emission of COMs. Only L1448 IRS 3A shows extended CH_3OH emission, and B1-b N shows no CH_3OH emission toward the continuum, but peaks at $\sim 1''$ away from the continuum, which is consistent with the existence of CH_3OH toward the continuum source blocked by opaque continuum (Marcelino et al. 2018). The enrichment of COMs due to outflows via sputtering (Arce et al. 2008) or photodesorption in the cavity walls (Drozdovskaya et al. 2015) dominates at a larger scale (>1000 au) and can be time dependent. It would therefore play a minor role for the COMs that are detected toward the continuum sources. Excluding L1448 IRS 3A, 28 sources (56%) are likely to have a hot-corino type chemistry. However, studies of the origin of COMs require higher spatial resolutions and are beyond the scope of this study.

4.2. Column Densities

From the method described in Section 3.4, we constrained the column densities of COMs along with their uncertainties (Table 5). Our modeling pipeline successfully reproduced the spectra of most PEACHES sample, except for Per-emb 17

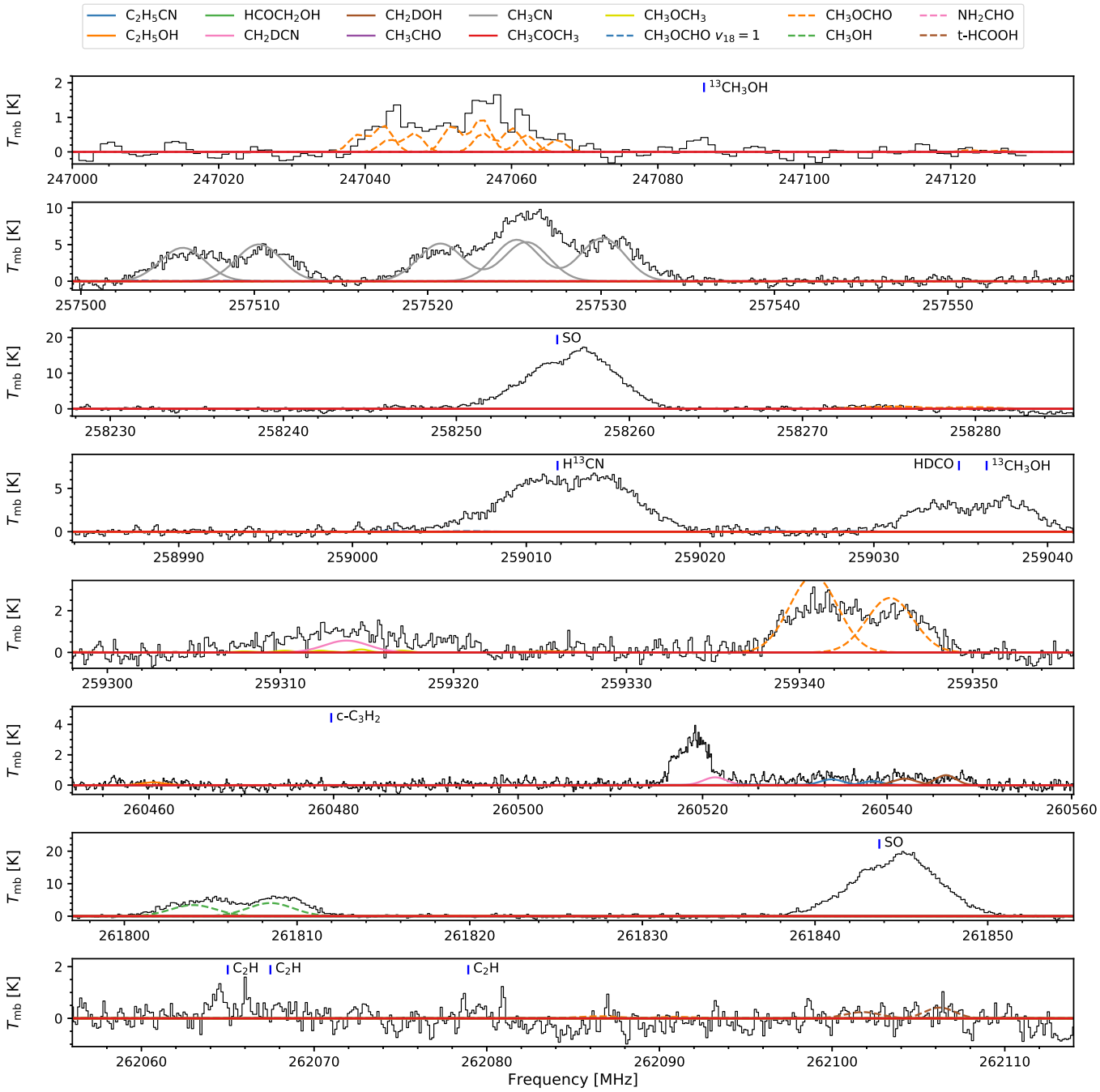

Figure 9. (Continued.)

because of its double-peaked line profile, which we further discuss in Section 4.2.1. Using the fitted column densities, we discuss the correlation between COMs in Section 4.2.2.

4.2.1. The Double-peaked Features of Per-emb 17

Per-emb 17 is a close binary system with a separation of $0\farcs278 \pm 0\farcs014$ (83.3 ± 4.0 au with a distance of 300 pc; Tobin et al. 2018). Our observations show clear double-peaked features for most of the emission (Figure 9). The position velocity diagram of the CH_3OH has a bar-shaped morphology, which may come from an unresolved disk (e.g., Lee et al. 2017; Yang et al. 2020), with asymmetric bright spots (Figure 10). However, the nature of these double-peaked features remains unclear because the spatial resolution in our observations is insufficient. The double-peaked feature challenges our standard modeling pipeline, which assumes a simple Gaussian line profile. Thus, we modeled the spectra of Per-emb 17 separately from the entire sample. In XCLASS, we set up two molecular gas components using the same assumptions as described in Section 3.4. Then, we configured the fitting to allow both components to vary in their velocity offset from the rest frequency by ± 5 km s^{-1}. The two velocity components for the emission of COMs appear at 1.96 km s^{-1}and -3.15 km s^{-1} on average, while the simple organics appear at slightly smaller velocity offsets. We reserve detailed analyses of the kinematics of Per-emb 17 for future studies. The fitting results become less robust with the additional velocity offset parameters because

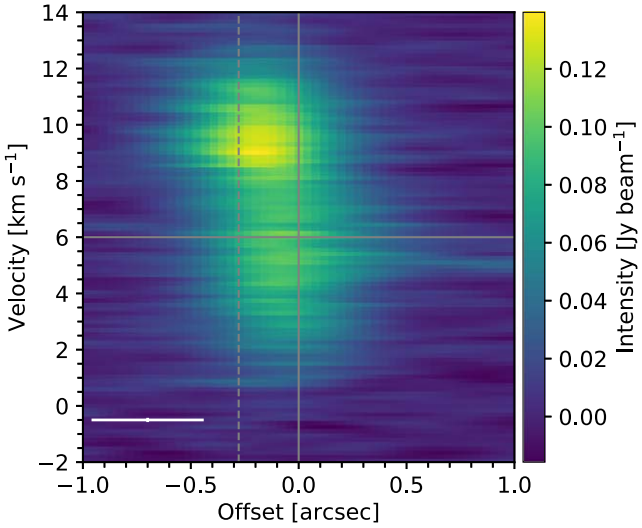

Figure 10. The position–velocity diagram of the CH_3OH emission at 243915.79 MHz toward Per-emb 17. The horizontal solid lines indicate the system velocity of 6.0 km s^{-1}. The vertical solid and dashed lines show the position of Per-emb 17 A and B, respectively. Per-emb 17 A is the main source. The white error bars indicate the beam size and the channel width.

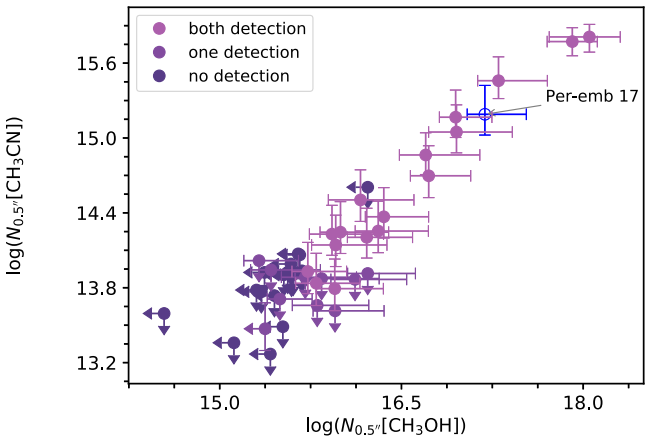

Figure 11. Correlation of the fitted column densities of CH_3OH and CH_3CN from the PEACHES sample. The data for Per-emb 17, which are estimated separately from the entire sample (Section 4.2.1), are shown as open circles and are annotated.

the double-peaked lines are blended. We therefoer performed a two-component fit with fixed velocity offsets at 1.96 km s^{-1}and -3.15 km s^{-1}, which reproduces the observations (Figure 9). To minimize the uncertainty due to substantial line blending, we estimated the total column density from the sum of the two components instead of reporting them individually. Then, we applied the same procedure to derive the mean column densities and upper limits as discussed in Section 3.4. Line blending still prevents accurate determinations of the column densities for a few species. In particular, the emission of CH_3OCH_3 at ~259310 MHz may be underestimated or severely contaminated by the emission of CH_2DCN, which has another transition at 260523 MHz that may be contaminated by SiO emission.

4.2.2. Correlations of COMs

The chemical evolution of protostars may leave certain patterns in the abundance of molecules as the dynamical evolution determines the density and temperature structures that regulate the chemical reactions. Thus, the abundance of COMs and their correlations provides critical information for studying the chemical evolution of embedded protostars. As described in Section 3.4, we fit the column density and line width with different excitation temperatures, resulting in a range of column densities as their uncertainty. Thus, we can investigate the correlation between the column density of each species to probe the underlying chemistry.

To quantify the goodness of correlation, we calculated the Pearson correlation coefficient (r), which tests the linearity of two variables. We used the bootstrap method to sample the fitted column densities to calculate the Pearson r. The bootstrap method is an iterative process that resamples the column densities and calculates the Pearson r for the sample that is drawn for each iteration. We took the correlation between CH_3OH and CH_3CN as an example to demonstrate this bootstrap method (Figure 11). For detections, we assumed an asymmetric normal distribution centered on the best-fit column density to account for the asymmetric uncertainty in logarithmic scale. The distribution on either side of the best-fit value has an equal probability, where the width of each "half" normal distribution follows the corresponding uncertainty. We ran the bootstrap process for 1000 iterations to characterize the distribution of the Pearson r. Including the nondetections for bootstrapping the correlation coefficient requires assuming that their underlying distribution is consistent with zero. However, assigning a distribution of the column densities of two species requires assuming that they are covariant, which determines the correlation coefficient. Thus, we only considered detection for the calculations of the correlation coefficient. Figure 12 shows the correlations of several COMs that were selected based on their detection rates as well as the ratios between species, which are discussed in Section 5.2. The column density of CH_3OH best correlates with that of CH_3CN (see also Figure 11). Belloche et al. (2020) also found a tight correlation between these two molecules from the CALYPSO survey, which has a smaller sample, 26 protostars, in several molecular clouds. The column densities of CH_3OCH_3 and CH_3OCHO also show a tight correlation. Jaber et al. (2014) also showed a tight correlation between CH_3OCH_3 and CH_3OCHO from different interstellar medium (ISM) sources, ranging from galactic center clouds, hot cores, protostars, and cold clouds to comets. Moreover, CH_3OH correlates with CH_3OCHO and CH_3OCH_3, which are the daughter species of CH_3OH, with a weaker correlation than with CH_3CN. The correlations between CH_3CN and CH_3OCHO or CH_3OCH_3 also show the same behavior. The decreasing correlation between CH_3OH or CH_3CN and the daughter species of CH_3OH, CH_3OCHO, and CH_3OCH_3 is consistent with the scenario in which CH_3OH and CH_3CN turns into CH_3OCHO and CH_3OCH_3 along with other COMs as the chemistry evolves (e.g., Garrod & Herbst 2006). The correlations of CH_3OH, CH_3CN, CH_3OCHO, and CH_3OCH_3 with other COMs show positive trends; however, the correlations are driven by a few sources due to the low detection rate of other COMs (Figure 13).

To directly compare the abundance of COMs, we normalized the column densities of COMs by $T_{b,cont}$, which is a proxy of the gas column density. The normalized column densities of COMs show similar correlations as the column densities (Figure 14, red markers). We further normalized the ratio of the column densities to $T_{b,cont}$ with L_{bol} and T_{bol} to test whether the correlation seen in Figure 14 (red markers) is dominated by

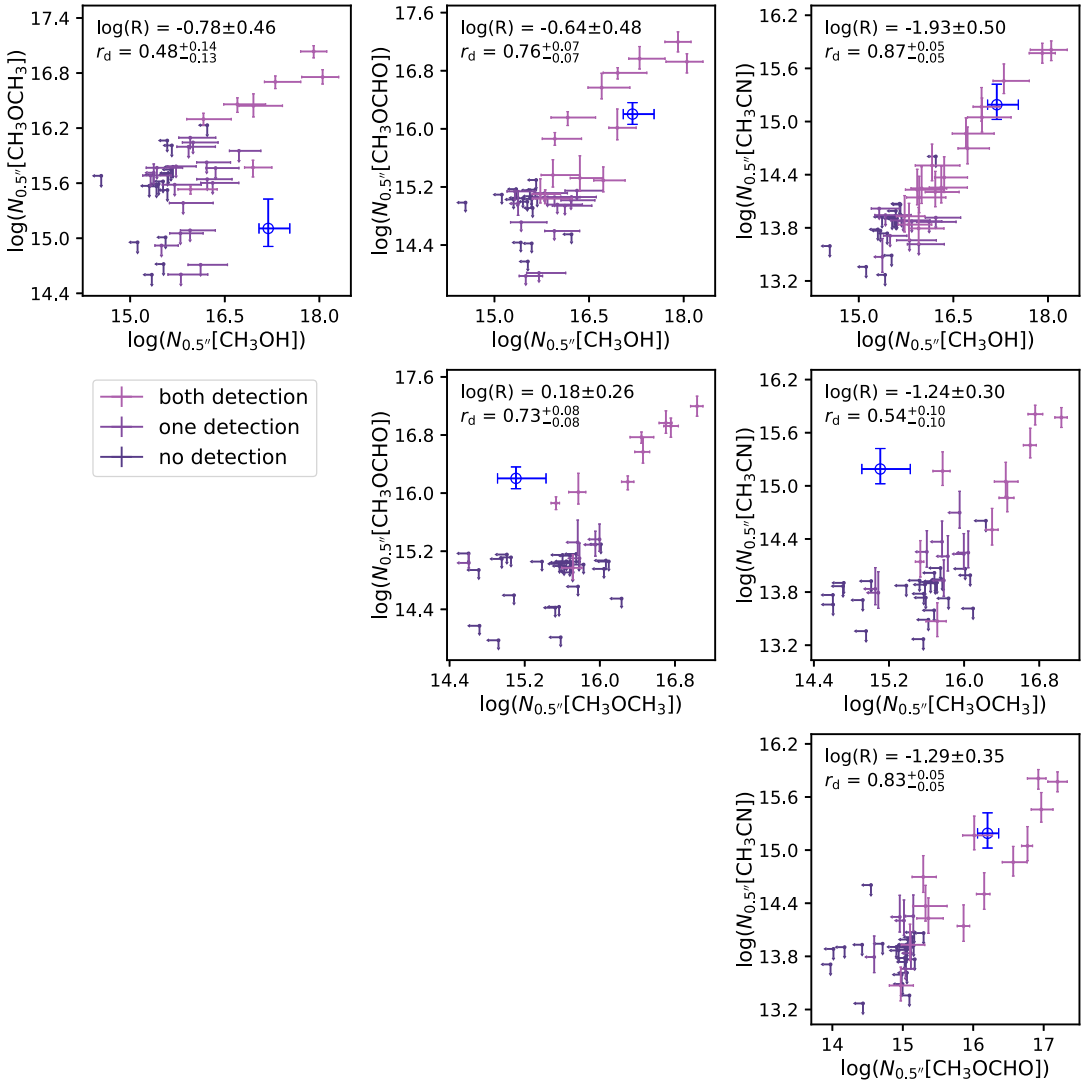

Figure 12. Corner plot of the correlations of the column densities between CH_3OH, CH_3CN, CH_3OCHO, and CH_3OCH_3. The color code follows that of Figure 11. The annotated texts indicate the Pearson r (r_d) and the logarithmic ratio of the two molecules (N_y/N_x) for the detection-only sample. The four most frequently detected COMs are shown in this figure, while other COMs are shown in Figure 13.

the protostellar properties. After the normalization with L_{bol} and T_{bol} (Figure 14, blue and black markers), the correlation between CH_3OH and CH_3OCH_3 weakens significantly, while CH_3CN also shows a considerable lower correlation with CH_3OCH_3. The correlations between CH_3OCHO and CH_3OCH_3 remain similar with different normalizations. Per-emb 17 is an outlier with a low and uncertain abundance of CH_3OCH_3 (Section 4.2.1), reducing the correlation strength. However, the correlation analyses excluding the abundance of Per-emb 17 show similar trends. In summary, CH_3CN has the best correlation with CH_3OH, followed by that of CH_3OCHO and CH_3OCH_3.

5. Discussion

5.1. Universal Chemistry among Hot Corinos?

For the protostars with compact emission of COMs, the so-called hot corinos, the abundance of COMs correlates well between the species. With the normalization of $T_{b,cont}$, the Pearson r for the correlations between the four most frequently detected species (CH_3OH, CH_3CN, CH_3OCHO, and CH_3OCH_3) range from 0.76 to 0.93 (Figure 12). The Pearson r for the same four species with all COM species has a median value of 0.86 with a range from 0.57 to 0.95 (Figure 13). The correlations remain unchanged with the normalizations of L_{bol} and T_{bol}, suggesting that the correlation that represents the chemistry of COMs may be independent of the evolutionary stage of protostars, as also suggested by Bianchi et al. (2019). The source size and beam dilution have limited impact on the derived column densities (see the discussion in Appendix F). The limited number of detections of the COMs except for the four most frequently detected COMs hinders a further quantification of their correlation strengths. While the PEACHES sample shows similar abundance ratios between COMs, the absolute column densities of COMs vary by 1–3 orders of magnitude, suggesting a diverse environment in the PEACHES survey.

To understand the chemical similarity of COMs seen in embedded protostars in different environments, we further test the effect of protostellar evolution with the abundance ratios of the four most abundant COMs (Figure 15). Per-emb 17 has a significantly lower column density of CH_3OCH_3 than the PEACHES sample, resulting in apparent outliers in

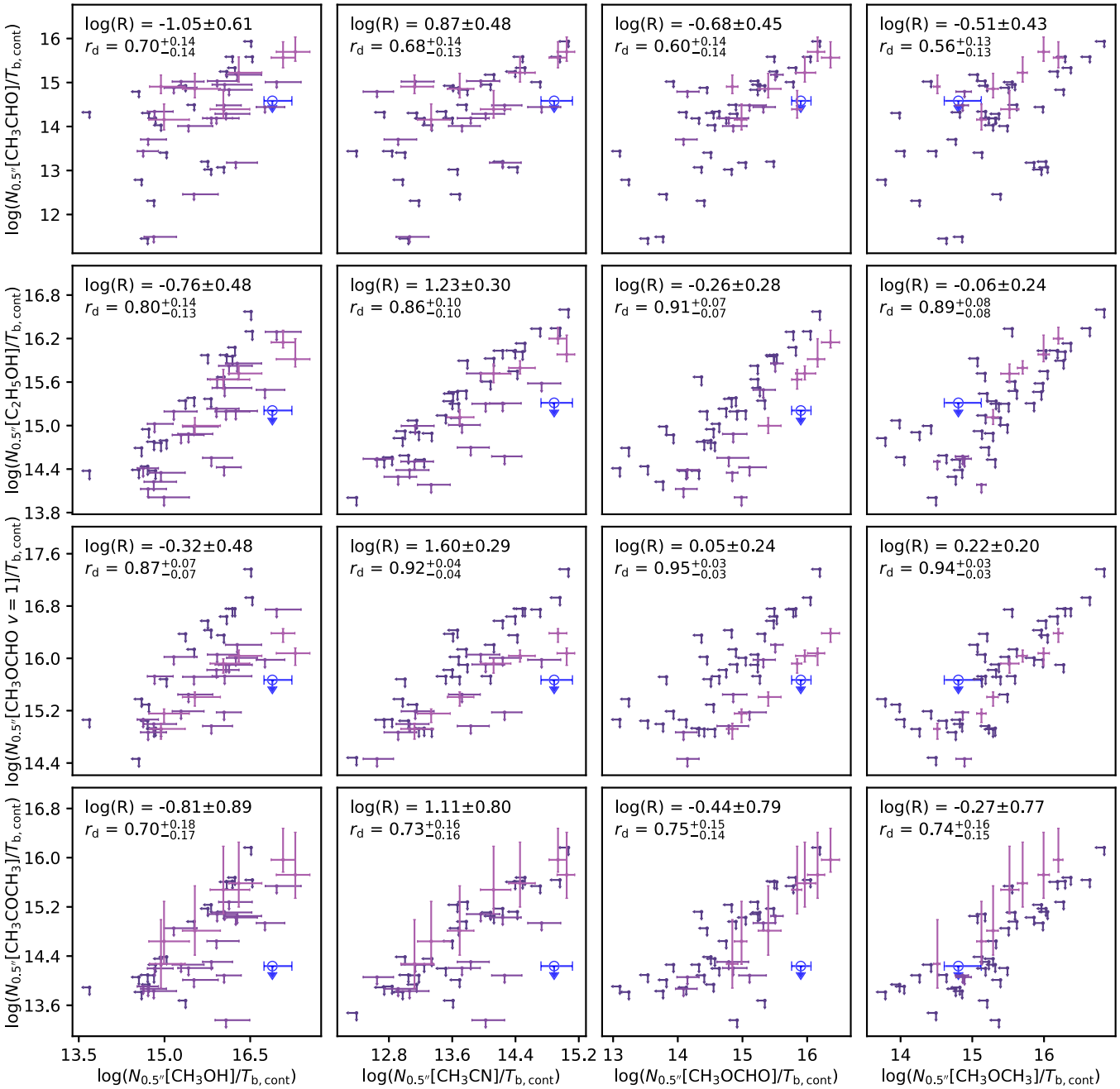

Figure 13. The correlations of the column densities normalized by the continuum brightness temperature between the more abundant COMs, CH_3OH, CH_3CN, CH_3OCHO, and CH_3OCH_3, and the less abundant COMs CH_3CHO, C_2H_5OH, CH_3OCHO $v = 1$, CH_3COCH_3, CH_3CH_2CN, *t*-HCOOH and NH_2CHO. The legends are similar to the legend in Figure 11.

Figure 15 (open circles). The ratios of CH_3CN/CH_3OH and CH_3OCH_3/CH_3OCHO, which are molecules with a similar complexity, have little variation as the functions of L_{bol}, T_{bol}, and $T_{b,cont}$. In contrast, the ratios of CH_3OCHO or CH_3OCH_3 to CH_3OH, which are the molecules with more complexity over the molecules with less complexity, increase with $T_{b,cont}$, whereas the ratios tentatively decrease with L_{bol} and T_{bol}. Because of its high abundance, CH_3OH may be more optically thick at a higher gas column density (high $T_{b,cont}$), resulting in an underestimation of the CH_3OH column density, hence the elevated ratios. The emission of CH_3CN is likely to be optically thin given its low abundance compared to that of CH_3OH. In fact, the highest fitted column density of CH_3CN, $\sim 10^{16}$ cm^{-2}, and the lowest modeled excitation temperature, 100 K, results in an optical depth of $\sim$0.4. The CH_3OH becomes optically thick when the column density exceeds 2×10^{17} and 5×10^{17} cm^{-2} at 100 K and 150 K, respectively. If the temperature is 200 K or higher, CH_3OH remains optically thin when $N \leqslant 10^{18}$ cm^{-2}, while our modeling estimates the highest column density of 1.1×10^{18} cm^{-2} in Per-emb 27. If the optical depth of CH_3OH plays a major role in the trend between the CH_3CN/CH_3OH and CH_3OCH_3/CH_3OCHO to $T_{b,cont}$, we would expect to see a similar trend in the CH_3CN/CH_3OH to $T_{b,cont}$, which shows a flat relation instead. Therefore the optical depth effect is unlikely to dominate the observed trend

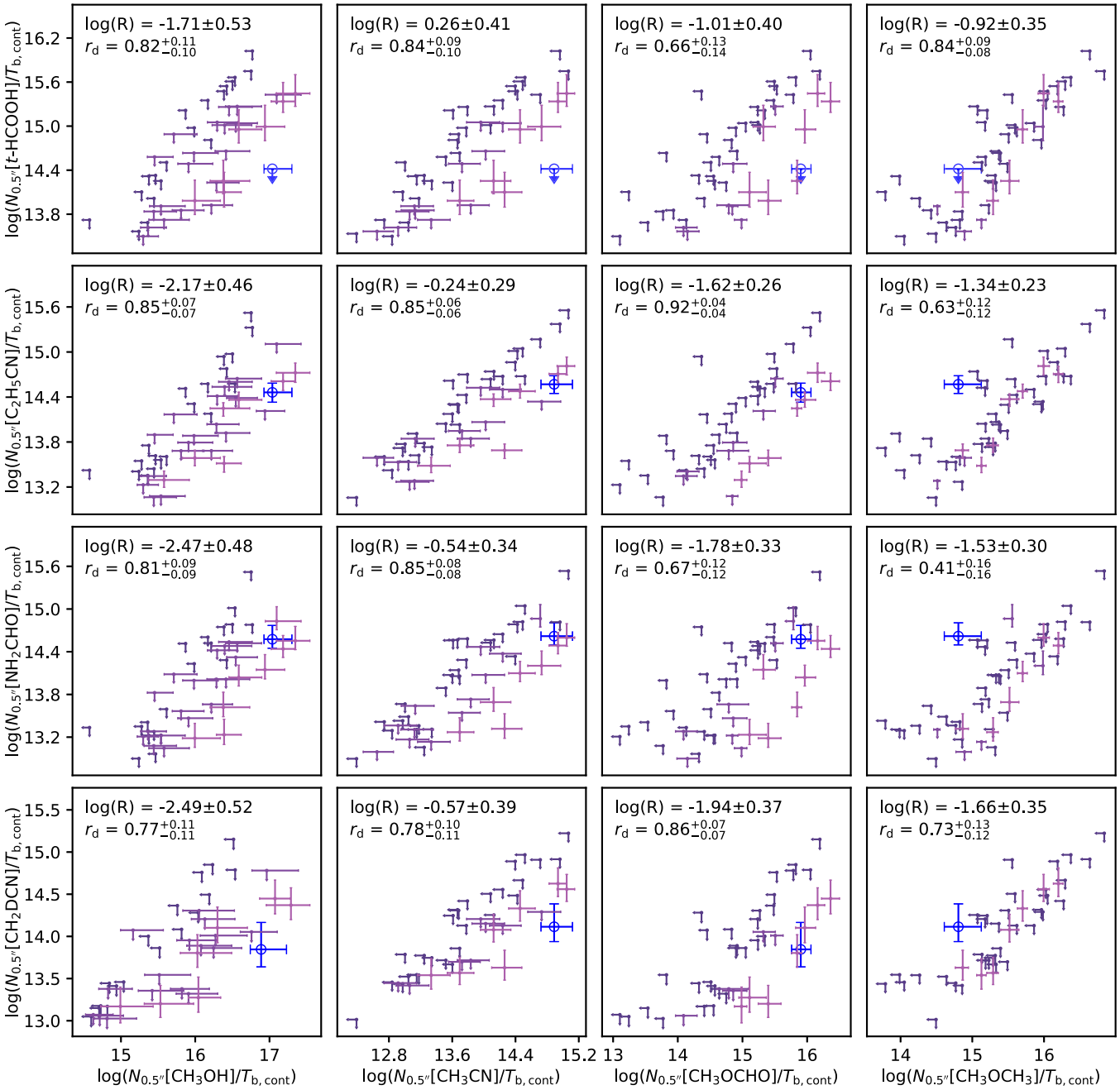

Figure 13. (Continued.)

between CH_3CN/CH_3OH and CH_3OCH_3/CH_3OCHO to $T_{b,cont}$. Chemical evolution is an alternative scenario for this trend. Under the scheme of grain-surface chemistry, CH_3OH primarily forms from the hydrogenation of CH_3O or CH_2OH on grains, while CH_3OCHO and CH_3OCH_3 primarily form from the radicals associated with H_2CO and CH_3OH destruction, which requires $T = 20$–40 K so that the radicals become mobile (Garrod & Herbst 2006). Thus, the elevated ratios of CH_3OCHO and CH_3OCH_3 to CH_3OH may be a result of a higher abundance of HCO and CH_3, a longer time of warm condition at high $T_{b,cont}$ sources for more efficient formation of CH_3OCHO, or more efficient formation of CH_3OCHO and CH_3OCH_3 in the gas phase after the evaporation/desorption of parent species, such as CH_3OH and CH_3O, as suggested by Balucani et al. (2015).

Higuchi et al. (2018) found a tentative trend where the sources closer to the edge of the cloud or the isolated sources show a higher ratio of C_2H to CH_3OH. Although our ALMA observations cannot fully sample the emission of C_2H, we can test if a similar trend exists between the abundance of COMs and the location of the sources in the cloud. We follow the approach described in Higuchi et al. (2018) to calculate the minimum distance (D_{min}) from the source to the edge of the cloud, which is arbitrarily defined as the 10σ level in the Planck 217 GHz observations.[9] Although the CH_3OH normalized by $T_{b,cont}$ has a large dynamic range (more than 2 orders of

[9] Based on observations obtained with Planck (http://www.esa.int/Planck), an ESA science mission with instruments and contributions directly funded by ESA Member States, NASA, and Canada.

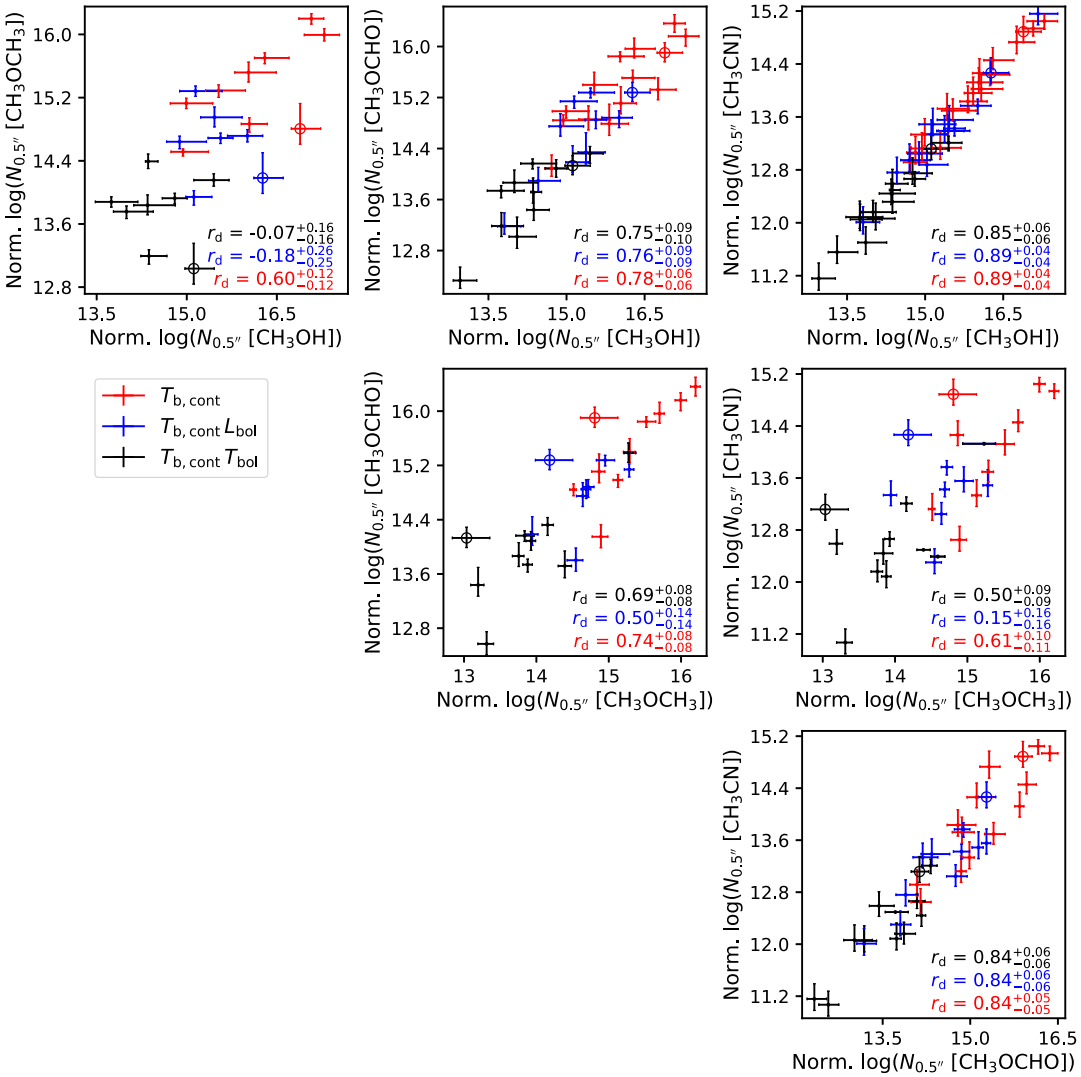

Figure 14. Corner plot of the correlations of the normalized column densities. The red, blue, and black symbols indicate the column densities normalized by the $T_{b,cont}$, $T_{b,cont}L_{bol}$, and $T_{b,cont}T_{bol}$. We only show the column densities if both molecules are detected. The Pearson r correlation coefficient for the detections with each normalization is shown in the legend with the corresponding color. A few close multiple sources, including Per-emb 12 A & B, Per-emb 35 A & B, and Per-emb 11 A & C, are excluded from the normalization of T_{bol} and L_{bol} because their SEDs are poorly determined.

magnitude), the D_{min} has no obvious effect on the normalized column density of CH_3OH (Figure 16). The column density of CH_3OH is normalized with the average continuum brightness temperature so that Figure 16 shows no clear threshold for the detection of CH_3OH due to the sensitivity. Because the emission of COMs appears compact in the PEACHES survey, the non-effect of D_{min} indicates that the D_{min} only impacts the carbon-chain molecules but not the COMs. However, two surveys have a factor of ∼40 difference in spatial resolution so that the chemical dependence with D_{min} need to be further investigated with observations that probe carbon-chain molecules and COMs at similar spatial scale. The nature of the abundance of C_2H requires a comprehensive analysis of the C_2H emission to confirm, which will be presented in future papers.

5.2. The Abundance Ratios of O-bearing and N-bearing COMs

The abundance ratios of COMs reflect the chemistry of COMs. Figure 17 compares the abundance ratios of COMs toward the PEACHES sample to the ratios from the CALYPSO survey (Belloche et al. 2020), the observations of individual protostars, and the model predictions from Garrod (2013). Belloche et al. (2020) divided the CALYPSO sample into three groups, where Group 1 has a low abundance of O-bearing COMs to CH_3OH, Group 2 has a higher abundance ratio of O-bearing COMs to CH_3OH than Group 1, and Group 3 is similar to Group 2, but has a higher abundance of CH_3CN and CH_3CH_2CN relative to CH_3OH and a lower abundance of O-bearing COMs. The abundance ratios of COMs toward the PEACHES sample generally agree with the ratios from the CALYPSO survey, which is expected because the sample overlaps significantly. Three out of four sources in Group 2 are Perseus protostars. Compared to one of the archetype hot corinos, IRAS 16293−2422 B, the ratios of COMs in the PEACHES sample are 2–18 times higher (Jørgensen et al. 2016, 2018; Calcutt et al. 2018). However, our sample has only a few sources with a comparable column density of CH_3OH, $\gtrsim 10^{18}$ cm^{-2}, as in IRAS 16293−2422, making the disagreement less robust. Moreover, our observations may underestimate the column densities of CH_3OH due to the dust optical depth. Constraining the true difference of the ratios requires

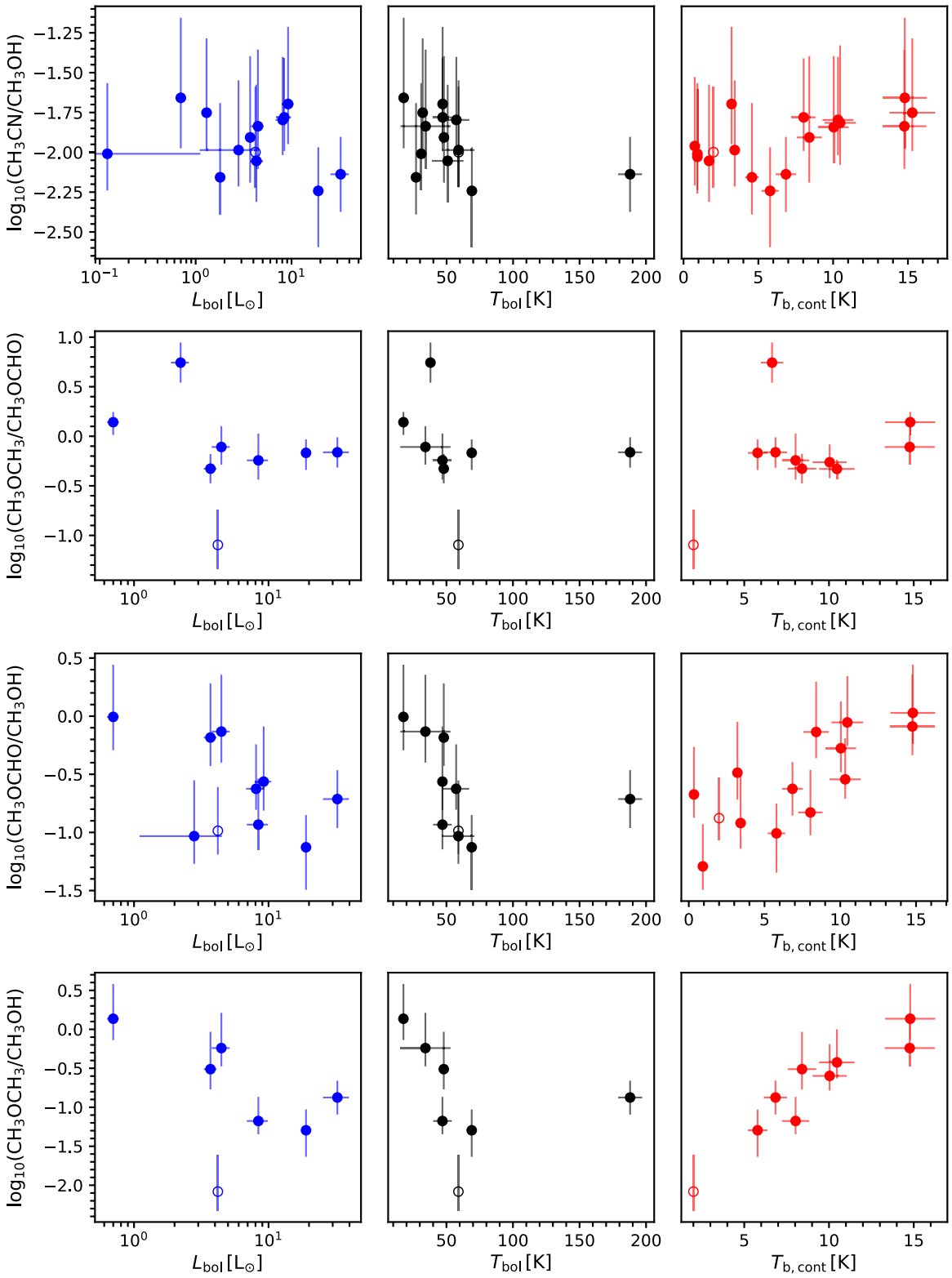

Figure 15. Ratios of well-detected molecules, CH_3OH, CH_3CN, CH_3OCHO, and CH_3OCH_3 as functions of L_{bol} (blue), T_{bol} (black), and $T_{b,cont}$ (red). The values of Per-emb 17 are shown as open circles, which may have higher systematic uncertainty due to the double-peaked line profile (Section 4.2.1). The uncertainties of L_{bol} and T_{bol} were taken from Tobin et al. (2016) and Murillo et al. (2016), where the properties of some sources are unconstrained and are therefore not shown. The uncertainty on $T_{b,cont}$ is 10%.

future analyses of the effect of the dust opacity, as demonstrated by De Simone et al. (2020).

We also compare the ratios of COMs to CH_3OH with the numerical results of chemo-physical models. Garrod (2013) modeled three different timescales for the warm-up phase in their model, where the formation of COMs becomes efficient (Garrod et al. 2008). The ratios of COMs toward the PEACHES sample differ from the ranges of the peak

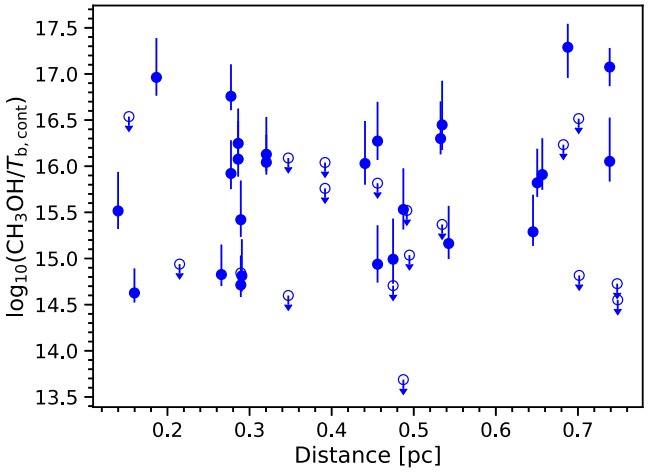

Figure 16. The column densities of CH_3OH toward the PEACHES sample (excluding Per-emb 17) normalized by the averaged continuum brightness temperature as a function of the minimum distance to the 10σ contour in the Planck 217 GHz observations. Due to the lower brightness at 217 GHz toward Per-emb 5 and Per-emb 25, their minimum distances are calculated with 5σ and 3σ contours, respectively. The solid circles show the sources with detection of CH_3OH, while the open circles show the sources without detection of CH_3OH.

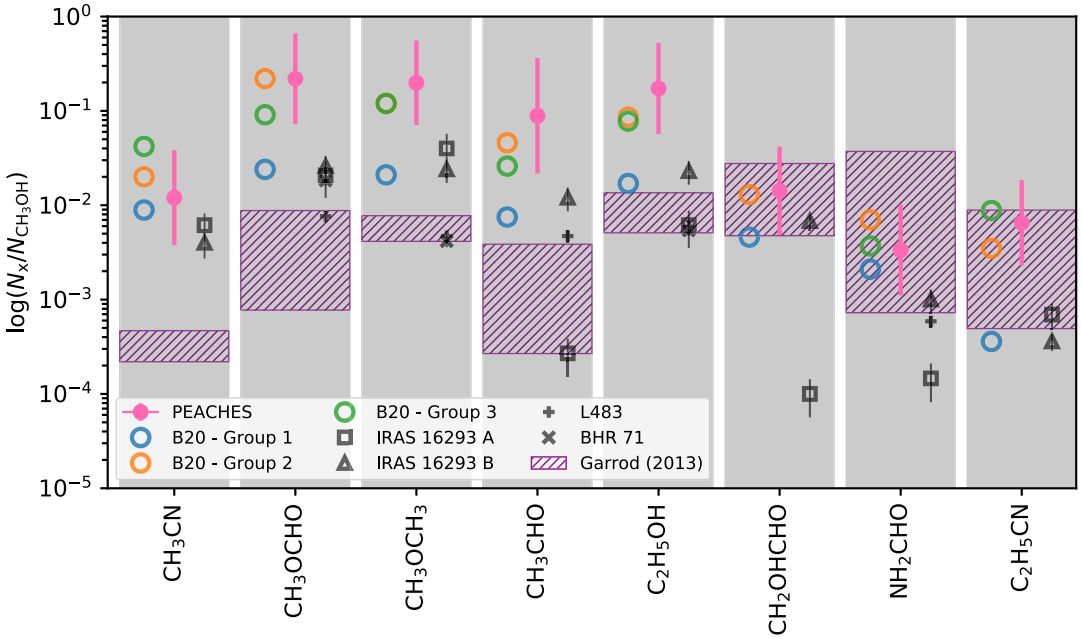

Figure 17. The ratios of the COMs commonly found in the PEACHES and the CALYPSO survey (Belloche et al. 2020), as well as a few selected hot corinos. The CALYPSO sources are categorized into three groups according to their COM abundance to CH_3OH. Group 3 has no detection of CH_2OHCHO. The column densities of COMs toward IRAS 16293−2422 B are taken from Jørgensen et al. (2016) for CH_3OH, Jørgensen et al. (2018) for C_2H_5OH, CH_3OCH_3, CH_3OCHO, CH_3CHO, NH_2CHO, and CH_2OHCHO, and Calcutt et al. (2018) for CH_3CN and CH_3CH_2CN. The column densities of COMs toward IRAS 16293−2422 A are taken from Manigand et al. (2020) for CH_3OH, C_2H_5OH, CH_3OCH_3, CH_3OCHO, CH_3CHO, NH_2CHO, and CH_2OHCHO, and Calcutt et al. (2018) for CH_3CN and CH_3CH_2CN. The column densities of COMs toward L483 are taken from Jacobsen et al. (2019). The column densities of COMs toward BHR 71 are taken from Yang et al. (2020), assuming a T_{ex} of 100 K for CH_3OH. The purple hatched regions indicate the range of the peak abundance ratios to CH_3OH from the warm-up models in Garrod (2013) that have three different speeds of the warm-up process.

abundance ratios in the warm-up models by Garrod (2013). The models underestimate the abundance ratios for most of the O-bearing COMs, while the ratios of CH_2OHCHO and N-bearing COMs agree with the ratios derived from the PEACHES sample (Figure 17). Because we may underestimate the column density of CH_3OH due to the optical depth, the abundance ratio to CH_3OH could be overestimated. If the ratios derived from the PEACHES sample were lower by a factor of 30, they would be consistent with the ratios in Garrod (2013) for the five COMs in the left, but the model would then overestimate the abundance ratios of CH_2OHCHO, NH_2CHO, and CH_3CH_2CN. This disagreement may point to a dominant gas-phase formation of (some) COMs other than CH_3OH, as suggested by other studies (e.g., Balucani et al. 2015; Skouteris et al. 2018; Vazart et al. 2020).

The well-correlated abundance of N-bearing COMs and O-bearing COMs (Figures 12 and 13) indicates no "N-/O-bearing COMs differentiation," which has long been discussed for

Orion-KL, a massive star-forming region (e.g., Friedel & Snyder 2008; Guélin et al. 2008; Feng et al. 2015; Tercero et al. 2018). The N-bearing COMs and O-bearing COMs segregate toward the hot core and the compact ridge of Orion-KL, respectively, which has been interpreted as a result of different temperatures at the prestellar phase or a different chemical evolutionary stage (Caselli et al. 1993; Laas et al. 2011; Neill et al. 2011; Garrod 2013). If the Perseus protostars have different initial conditions at the prestellar stage or are at different chemical stages that would result in a similar differentiation in Orion-KL, we would expect to detect a variety of N-bearing COMs to O-bearing COMs ratios. However, the well-correlated abundance of N-bearing COMs and O-bearing COMs suggests that the Perseus protostars may form from a similar initial condition or be in a similar chemical stage. Further studies of region-to-region comparisons await.

5.3. Origin of the CH_3OH/CH_3CN Correlation

The tight correlation between CH_3OH and CH_3CN is a striking finding of the PEACHES survey, while studies such as Bergner et al. (2017) and Belloche et al. (2020) have shown a similar trend with fewer detections or larger scatter. Belloche et al. (2020) argued that this correlation between CH_3OH and CH_3CN may not be due to chemistry because of the somewhat unrelated formation pathways of two molecules. If the gas-phase chemistry is negligible for the production of CH_3OH and CH_3CN, the tight correlation between CH_3OH and CH_3CN suggests a similar abundance ratio of two molecules on the icy grains prior to being thermally desorbed, hinting at a common chemistry of COMs in the warm protostellar envelope. The tight correlation may also reflect a uniform elemental abundance of O and N in the Perseus molecular cloud before the star formation.

The compact emission of CH_3OH has a well-known icy origin, where CH_3OH forms via subsequent CO hydrogenation on the surface of dust grains (Tielens & Whittet 1997; Watanabe et al. 2003; Rimola et al. 2014). At a cold temperature, the nonthermal desorption and/or the excessive energy from the formation of CH_3OH that kicks it off from dust grains are thought to be responsible for the presence of gaseous CH_3OH (e.g., Garrod et al. 2007; Vasyunin & Herbst 2013; Soma et al. 2015, but see the discussion in Pantaleone et al. (2020) on the chemical desorption probability). CH_3CN can form in the gas phase via radiative association ($HCN + CH_3^+ \rightarrow CH_3CNH^+ + h\nu$) followed by the dissociative recombination of CH_3CNH^+ or on the grain surface. The grain-surface reactions to form CH_3CN can occur at a cold temperature by the hydrogenation of CCN, which can form via C+CN or $C_2 + N$. At a warm temperature, CH_3CN can form directly from reactions between the radicals CH_3 and CN. For embedded protostars, the grain-surface reactions are thought to dominate the production of CH_3CN; however, it remains unclear whether the cold-phase or the warm-phase grain-surface pathway regulates the abundance of CH_3CN.

Assuming an icy grain origin for both CH_3OH and CH_3CN, we can further test the efficiency of the cold- and warm-phase pathways by comparing the ratio of CH_3CN/CH_3OH toward the prestellar and protostellar sources. In prestellar cores, $[CH_3CN/CH_3OH]$ are 0.28, 0.0192 ± 0.0075, and 0.021 ± 0.008 for TMC 1-CP (cyanoployyne peak; Kaifu et al. 2004; Gratier et al. 2016), L1521 E (Nagy et al. 2019), and L1544 (Nagy et al. 2019), respectively. The ratio of TMC1-CP is substantially higher than that in our survey, $0.012^{+0.009}_{-0.005}$, while the mean ratios of L1521 E and L1544 seem higher than the ratio in our survey within 1σ uncertainty. Furthermore, we can divide the PEACHES sample into Class 0 and I according to their T_{bol} (Class 0: $T_{bol} < 70$ K; Class I: $T_{bol} \geqslant 70$ K; Dunham et al. 2014). Only one Class I source has emission of both CH_3OH and CH_3CN, along with another borderline Class I source, which has a T_{bol} of 69 K. The mean value of CH_3CN/CH_3OH for Class I sources ($N = 2$) is $6.5^{+6.0}_{-3.0} \times 10^{-3}$, while the mean value for Class 0 sources ($N = 12$) is $1.4^{+1.1}_{-1.1} \times 10^{-2}$. Only the sources with reliable measurements of T_{bol} were included. Although the difference is within the uncertainty, the tentative decrease of CH_3CN/CH_3OH from Class 0 to Class I phase would be consistent with the tentative decrease of CH_3CN/CH_3OH from prestellar to protostellar phase. This difference provides constraints on the interplay between the production of CH_3CN in the warm and cold phase. Testing the chemical pathways of CH_3CN requires more measurements of CH_3CN and CH_3OH in Class I and prestellar sources.

Alternatively, the desorption process may regulate the number of COMs in the gas phase. Studies find a similar binding energy for CH_3OH and CH_3CN (Collings et al. 2004; McElroy et al. 2013; Wakelam et al. 2015, 2017; Penteado et al. 2017). Recently, Ferrero et al. (2020) showed a similar range of binding energies for CH_3OH (3770–8618 K) and CH_3CN (4745–7652 K) simulated with amorphous solid water. Thus, both molecules may simply desorb from grains at a similar rate if the ice mantles have not completely desorbed. However, the microphysics during the desorption involve the structure of the water ice and how the COMs reside in the ice matrix, requiring further understanding of how the chemical evolution takes place on the grain surface. Furthermore, the distribution of the binding energy can have a crucial effect on the estimate of the desorbed species (Ferrero et al. 2020; Grassi et al. 2020).

6. Conclusions

This work presents the PEACHES survey, an unbiased chemistry survey of COMs toward 50 embedded protostars in the Perseus molecular cloud using ALMA Band 6 observations. The main conclusions are listed below.

1. Perseus Class 0/I protostars commonly (58%) show warm COM emission. CH_3OH is the most frequently detected species of COMs, while our observations show the emission of 12 O-bearing COMs and 4 N-bearing COMs, including isotopologs.
2. Complex organic molecules other than CH_3OH are detected for the first time toward Per-emb 35 A and Per-emb 11 A.
3. The CH_3OH and CH_3CN normalized column density ($N/T_{b,cont}$) has a large diversity (more than two orders of magnitude), suggesting the existence of chemical diversity in the sources in the Perseus molecular cloud. Moreover, the detectability of these COMs is not directly related to protostellar properties such as T_{bol}, L_{bol}, and the gas mass column density.
4. The column density of CH_3OH is tightly correlated with that of CH_3CN with a Pearson r of 0.87, where two molecules may not have a common chemical origin. The abundance of the most frequently detected COMs,

CH_3OH, CH_3CN, CH_3OCHO, and CH_3OCH_3, correlate with other species of COMs, which are detected in fewer sources in the PEACHES sample, hinting at a common chemistry of COMs in the Perseus embedded protostars. Protostellar properties such as L_{bol}, T_{bol}, and the minimum distance to the cloud edge have little impact on the number of detected COMs and the abundance of COMs.

5. CH_3OCHO and CH_3OCH_3 are the most abundant COMs other than CH_3OH, with abundance ratios to CH_3OH of $0.22^{+0.17}_{-0.10}$ and $0.21^{+0.15}_{-0.09}$, respectively. The abundance of COMs to CH_3OH in the PEACHES sample is similar to that in the CALYPSO survey (Belloche et al. 2020), which includes 14 Perseus sources in 26 samples, and 6 of 14 sources exhibit emission of COMs. The abundance ratios of NH_2CHO and CH_3CH_2CN agree with the model predictions by Garrod (2013), which underestimate the abundance of the O-bearing COMs. However, the abundance ratios of O-bearing COMs and CH_3CN (e.g., CH_3CN to CH_3OCHO and CH_3OCHO to CH_3OCH_3) seem to be consistent with the abundance ratios predicted in Garrod (2013) (Figure 17). alternatively, the disagreement may indicate that at least some COMs are the products of gas-phase chemistry (Balucani et al. 2015; Skouteris et al. 2018; Vazart et al. 2020).
6. The CH_3CN/CH_3OH ratio of Perseus sources seems lower than the same ratio for other prestellar cores, especially L1544. For the two Class I sources with detections of both molecules, the ratio is $6.5^{+6.0}_{-3.0} \times 10^{-3}$ compared to $1.4^{+1.1}_{-1.1} \times 10^{-2}$ for the Class 0 sources. This may suggest an evolution of the contributions from the gas-phase chemistry and grain-surface chemistry from the prestellar to protostellar phase.
7. The ratios of more complex COMs, such as CH_3OCHO and CH_3OCH_3, to the less complex COMs, such as CH_3OH and CH_3CN, increase with the averaged continuum brightness temperature, which is a proxy of the gas column density, suggesting an enhanced production of more complex COMs toward the sources with more centrally concentrated mass.

Y.-L. Yang acknowledges support from the JSPS Postdoctoral Fellowship from the Japan Society for the Promotion of Science and the Virginia Initiative of Cosmic Origins Postdoctoral Fellowship. Y.-L. Yang also acknowledges the visitor support from the Institute of Astronomy and Astrophysics, Academia Sinica. Y.-L.Y. thanks L.I. Cleeves for fruitful discussion. This work was supported by JSPS KAKENHI grants 16H03964, 18H05222, and 20H05845. This paper makes use of the following ALMA data: ADS/JAO. ALMA#2016.0.00391.S. ALMA is a partnership of ESO (representing its member states), NSF (USA), and NINS (Japan), together with NRC (Canada), *MOST*, and ASIAA (Taiwan), and KASI (Republic of Korea), in cooperation with the Republic of Chile. The Joint ALMA Observatory is operated by ESO, AUI/NRAO, and NAOJ. The National Radio Astronomy Observatory is a facility of the National Science Foundation operated under cooperative agreement by Associated Universities, Inc.

Facility: ALMA.

Software: astropy (Astropy Collaboration et al. 2018), CASA (McMullin et al. 2007), RADEX (van der Tak et al. 2007), spectral-cube v. 0.5.0 (Robitaille et al. 2016), and XCLASS (Möller et al. 2017).

Appendix A
Catalogs for Molecular Data

The spectroscopic data are taken from the Cologne Database of Molecular Spectroscopy (CDMS; Müller et al. 2001, 2005; Endres et al. 2016) and the Jet Propulsion Laboratory (JPL; Pickett et al. 1998). Table A1 lists only the references that cover the frequencies relevant to this study.

Table A1
Molecular Catalogs

Molecule	References	Molecule	References
C_2H	Sastry et al. (1981), Müller et al. (2000)	c-C_3H_2	Bogey et al. (1986), Vrtilek et al. (1987)
SO_2	Patel et al. (1979), Helminger & De Lucia (1985), Lovas (1985), Alekseev et al. (1996)		
CH_3OH	Xu et al. (2008)	$^{13}CH_3OH$	Plummer et al. (1984), Oesterling et al. (1999), Carvajal et al. (2007), Maeda et al. (2008), Ilyushin et al. (2009)
CH_2DOH	Pearson et al. (2012)	$CH_3^{18}OH$	Fisher et al. (2007)
SO $^3\Sigma$	Powell et al. (1964), Amano & Hirota (1974), Clark & De Lucia (1976), Lovas et al. (1992), Cazzoli et al. (1994)	*t*-HCOOH	Lerner et al. (1957), Trambarulo et al. (1958), Kim et al. (1962), Bellet et al. (1971), Kuze et al. (1982)
$H^{13}CN$	Maiwald et al. (2000), Fuchs et al. (2004), Cazzoli & Puzzarini (2005)	CS	Müller et al. (2005)
HDCO	Bocquet et al. (1999)	CH_3OCHO ($v = 0, 1$)	Ilyushin et al. (2009)
CH_3OCH_3	Endres et al. (2009)	CH_3COCH_3	Groner et al. (2002)
CH_3CN	Cazzoli & Puzzarini (2006), Müller et al. (2009)	CH_2DCN	Nguyen et al. (2013)
CH_3CH_2CN	Pearson et al. (1994), Brauer et al. (2009)	CH_3CHO	Kleiner et al. (1996)
C_2H_5OH	Pearson et al. (1996, 2008)	CH_2OHCHO	Butler et al. (2001)
NH_2CHO	Blanco et al. (2006), Kryvda et al. (2009)		

Appendix B
Identified Species and Transitions

Table B1 lists the species and their transitions identified from the PEACHES spectra.

Table B1
Line Identification

Frequency (MHz)	Transition[a]	log(Einstein-A)	E_u (K)	g_u	Reference
		Ethynyl (CCH)			
262065.00 (0.05)	[3, 5/2, 3] → [2, 3/2, 2][b]	−4.31	25.16	7	CDMS
262067.47 (0.05)	[3, 5/2, 2] → [2, 3/2, 1][b]	−4.35	25.16	5	CDMS
262078.93 (0.02)	[3, 5/2, 2] → [2, 3/2, 2][b]	−5.22	25.16	5	CDMS
		Cyclopropenylidene (c-C_3H_2)			
244222.15 (0.01)	[3, 2, 1] → [2, 1, 2]	−4.23	18.17	21	CDMS
246557.77 (0.02)	[16, 10, 7] → [16, 9, 8]	−3.36	397.83	99	CDMS
260479.75 (0.02)	[5, 3, 2] → [4, 4, 1]	−3.79	44.72	33	CDMS
		Methanol (CH_3OH $v_t = 0$)			
243915.79 (0.01)	[5, 1, 4] → [4, 1, 3] A	−4.22	49.66	44	CDMS
246074.61 (0.02)	[20, 3, 17] → [20, 2, 18] A	−4.08	537.03	164	CDMS
246873.30 (0.02)	[19, 3, 16] → [19, 2, 17] A	−4.08	490.65	156	CDMS
261805.68 (0.01)	[2, 1, 1] → [1, 0, 1] E	−4.25	28.01	20	CDMS
		Methanol ($^{13}CH_3OH$ $v_t = 0$)			
246426.12 (0.22)	[23, 4, 19] → [22, 5, 18]	−4.58	721.02	47	CDMS
247086.3 (0.5)	[23, 3, 20] → [23, 2, 21] A− → A+	−4.07	674.86	47	CDMS
259036.49 (0.17)	[17, 3, 15] → [17, 2, 16] A+ → A−	−4.04	396.48	35	CDMS
		Methanol (CH_2DOH $v_t = 0$)			
243514.31 (0.01)	[9, 2, 8] → [10, 1, 10] o_1	−5.17	131.85	19	JPL
246973.11 (0.01)	[4, 1, 4] → [4, 1, 3] e_1	−4.67	37.69	9	JPL
260543.63 (0.01)	[3, 2, 1] → [3, 1, 2] o_1	−4.65	48.34	7	JPL
		Methanol ($CH_3^{18}OH$ $v_t = 0$)			
246256.60 (0.04)	[11. 2. 10] → [10, 3, 7] A	−4.64	184.27	92	CDMS
		Sulfur monoxide (SO $^3\Sigma$)			
258255.83 (0.01)	[N, J] = [6, 6] → [5, 5]	−3.67	56.50	13	CDMS
261843.72 (0.03)	[N, J] = [7, 6] → [6, 5]	−3.64	47.55	15	CDMS
		Sulfur monoxide (^{34}SO)			
246663.47 (0.1)	[N, J] = [5, 6] → [4, 5]	−3.74	49.89	11	CDMS
		Sulfur dioxide (SO_2)			
244254.22 (0.01)	[14, 0, 14] → [13, 1, 13]	−3.79	93.90	29	CDMS
		Hydrogen cyanide ($H^{13}CN$)			
259010.26 (0.01)	[J, F] = [3, 3] → [2, 3]	−4.07	24.86	7	CDMS
259011.55 (0.01)	[J, F] = [3, 2] → [2, 1]	−3.19	24.86	5	CDMS
259011.80 (0.01)	[J, F] = [3, 3] → [2, 2]	−3.16	24.86	7	CDMS
259011.86 (0.01)	[J, F] = [3, 4] → [2, 3]	−3.11	24.86	9	CDMS
259012.34 (0.01)	[J, F] = [3, 2] → [2, 3]	−5.46	24.86	5	CDMS
259013.89 (0.01)	[J, F] = [3, 2] → [2, 2]	−3.92	24.86	5	CDMS
		Carbon monosulfide (CS)			
244935.56 (0.01)	[J] = [5] → [4]	−3.53	35.27	11	CDMS
		Formaldehyde (HDCO)			
246924.6 (0.1)	[4, 1, 4] → [3, 1, 3]	−3.40	37.60	9	CDMS
259034.9 (0.1)	[4, 2, 2] → [3, 2, 1]	−3.44	62.86	9	CDMS

Table B1
(Continued)

Frequency (MHz)	Transition[a]	log(Einstein-A)	E_u (K)	g_u	Reference
		Methyl formate (CH_3OCHO)			
245883.2 (0.1)	[20, 13, 7] → [19, 13, 6] E	−3.89	235.98	82	JPL
245885.2 (0.1)	[20, 13, 7] → [19, 13, 6] A	−3.89	235.98	82	JPL
245885.2 (0.1)	[20, 13, 8] → [19, 13, 7] A	−3.89	235.98	82	JPL
245903.7 (0.1)	[20, 13, 8] → [19, 13, 7] E	−3.89	235.97	82	JPL
246027.5 (0.1)	[21, 2, 19] → [20, 3, 18] E	−4.63	139.85	86	JPL
246038.9 (0.1)	[21, 2, 19] → [20, 3, 18] A	−4.63	139.85	86	JPL
246054.8 (0.1)	[20, 12, 8] → [19, 12, 7] E	−3.84	219.43	82	JPL
246060.8 (0.1)	[20, 12, 8/9] → [19, 12, 7/8] A	−3.84	219.43	82	JPL
246076.9 (0.1)	[20, 12, 9] → [19, 12, 8] E	−3.84	219.41	82	JPL
246285.4 (0.1)	[20, 11, 9] → [19, 11, 8] E	−3.80	204.21	82	JPL
246295.1 (0.1)	[20, 11, 10] → [19, 11, 9] A	−3.80	204.21	82	JPL
246295.1 (0.1)	[20, 11, 9] → [19, 11, 8] A	−3.80	204.21	82	JPL
246308.3 (0.1)	[20, 11, 10] → [19, 11, 9] E	−3.80	204.20	82	JPL
246456.1 (0.1)	[10, 5, 6] → [9, 4, 5] E	−5.52	49.09	42	JPL
246600.0 (0.1)	[20, 10, 10] → [19, 10, 9] E	−3.77	190.34	82	JPL
246613.4 (0.1)	[20, 10, 11] → [19, 10, 10] A	−3.77	190.34	82	JPL
246613.4 (0.1)	[20, 10, 10] → [19, 10, 9] A	−3.77	190.34	82	JPL
246623.2 (0.1)	[20, 10, 11] → [19, 10, 10] E	−3.77	190.34	82	JPL
246660.5 (0.1)	[10, 5, 6] → [9, 4, 5] A	−4.74	49.08	42	JPL
246675.4 (0.1)	[15, 4, 12] → [14, 3, 11] E	−4.93	81.85	62	JPL
246683.5 (0.1)	[15, 4, 12] → [14, 3, 11] A	−4.93	81.84	62	JPL
246752.9 (0.1)	[10, 5, 5] → [9, 4, 5] E	−4.90	49.10	42	JPL
246891.6 (0.1)	[19, 4, 15] → [18, 4, 14] E	−3.66	126.22	78	JPL
246914.7 (0.1)	[19, 4, 15] → [18, 4, 14] A	−3.66	126.22	78	JPL
246945.7 (0.1)	[10, 5, 6] → [9, 4, 6] E	−4.90	49.09	42	JPL
247040.7 (0.1)	[20, 9, 11] → [19, 9, 10] E	−3.74	177.83	82	JPL
247044.1 (0.1)	[21, 3, 19] → [20, 3, 18] E	−3.66	139.90	86	JPL
247053.5 (0.1)	[21, 3, 19] → [20, 3, 18] A	−3.66	139.89	86	JPL
247057.3 (0.1)	[20, 9, 12] → [19, 9, 11] A	−3.74	177.83	82	JPL
247057.7 (0.1)	[20, 9, 11] → [19, 9, 10] A	−3.74	177.83	82	JPL
247063.7 (0.1)	[20, 9, 12] → [19, 9, 11] E	−3.74	177.83	82	JPL
247124.3 (0.1)	[10, 5, 5] → [9, 4, 6] E	−4.74	49.08	42	JPL
258275.0 (0.1)	[21, 13, 8] → [20, 13, 7] E	−3.79	248.37	86	JPL
258277.4 (0.1)	[21, 13, 8] → [20, 13, 7] A	−3.79	248.37	86	JPL
258277.4 (0.1)	[21, 13, 9] → [20, 13, 8] A	−3.79	248.37	86	JPL
259341.9 (0.1)	[24, 0, 24] → [23, 1, 23] E	−4.37	158.23	98	JPL
259342.0 (0.1)	[24, 1, 24] → [23, 1, 23] E	−3.58	158.23	98	JPL
259342.1 (0.1)	[24, 0, 24] → [23, 0, 23] E	−3.58	158.23	98	JPL
259342.3 (0.1)	[24, 1, 24] → [23, 0, 23] E	−4.37	158.23	98	JPL
259342.7 (0.1)	[24, 0, 24] → [23, 1, 23] A	−4.37	158.22	98	JPL
259342.9 (0.1)	[24, 1, 24] → [23, 1, 23] A	−3.58	158.22	98	JPL
259343.0 (0.1)	[24, 0, 24] → [23, 0, 23] A	−3.58	158.22	98	JPL
259343.2 (0.1)	[24, 1, 24] → [23, 0, 23] A	−4.37	158.22	98	JPL
261822.3 (0.1)	[17, 10, 7] → [17, 9, 8] A	−4.73	156.63	70	JPL
262088.2 (0.1)	[16, 10, 6] → [16, 9, 7] A	−4.76	146.59	66	JPL
262088.2 (0.1)	[16, 10, 7] → [16, 9, 8] A	−4.76	146.59	66	JPL
		Methyl formate (CH_3OCHO $v = 1$)			
243511.5 (0.1)	[20, 12, 8] → [19, 12, 7] E	−3.85	407.25	82	JPL
245846.9 (0.1)	[21, 3, 19] → [20, 3, 18] E	−3.66	326.30	86	JPL
246106.8 (0.1)	[20, 7, 14] → [19, 7, 13] A	−3.70	343.77	82	JPL
246184.2 (0.1)	[20, 8, 13] → [19, 8, 12] E	−3.72	353.27	82	JPL
246187.0 (0.1)	[21, 2, 19] → [20, 2, 18] A	−3.66	326.62	86	JPL
246233.6 (0.1)	[20, 7, 13] → [19, 7, 12] A	−3.70	343.79	82	JPL
246274.9 (0.1)	[20, 7, 13] → [19, 7, 12] E	−3.70	343.86	82	JPL
246410.95 (0.01)	[10, 5, 5] → [9, 4, 6] A	−4.73	236.70	42	JPL
246422.7 (0.1)	[22, 1, 21] → [21, 2, 20] A	−4.51	330.43	90	JPL
246461.2 (0.1)	[22, 2, 21] → [21, 2, 20] A	−3.65	330.43	90	JPL
246488.4 (0.1)	[22, 1, 21] → [21, 1, 20] A	−3.65	330.43	90	JPL
246562.9 (0.1)	[21, 2, 19] → [20, 2, 18] E	−3.66	326.24	86	JPL
246706.5 (0.1)	[22, 2, 21] → [21, 2, 20] E	−3.65	329.89	90	JPL
246731.7 (0.1)	[22, 1, 21] → [21, 1, 20] E	−3.65	329.89	90	JPL

Table B1
(Continued)

Frequency (MHz)	Transition[a]	log(Einstein-A)	E_u (K)	g_u	Reference
246985.2 (0.1)	[20, 6, 15] → [19, 6, 14] A	−3.68	335.37	82	JPL
259003.9 (0.1)	[21, 7, 14] → [20, 7, 13] A	−3.63	356.22	86	JPL
259025.8 (0.1)	[21, 7, 14] → [20, 7, 13] E	−3.63	356.29	86	JPL
260479.6 (0.1)	[44, 9, 36] → [44, 8, 37] A	−4.59	828.74	178	JPL
	Dimethyl ether (CH_3OCH_3)				
246499.29 (0.01)	[37, 6, 31] → [37, 5, 12] AA	−4.01	693.72	750	CDMS
246505.09 (0.01)	[37, 6, 31] → [37, 5, 12] AE	−4.01	693.72	450	CDMS
246505.09 (0.01)	[37, 6, 31] → [37, 5, 12] EA	−4.01	693.72	300	CDMS
246697.43 (0.01)	[27, 4, 23] → [26, 5, 21] AA	−4.70	367.61	330	CDMS
246697.87 (0.01)	[27, 4, 23] → [26, 5, 21] EE	−4.70	367.61	880	CDMS
246698.31 (0.01)	[27, 4, 23] → [26, 5, 21] AE	−4.70	367.61	110	CDMS
246698.31 (0.01)	[27, 4, 23] → [26, 5, 21] EA	−4.70	367.61	220	CDMS
259305.22 (0.01)	[33, 3, 31] → [34, 6, 28] AA	−6.61	563.02	670	CDMS
259308.39 (0.01)	[33, 3, 31] → [34, 6, 28] AE	−6.61	563.02	402	CDMS
259308.39 (0.01)	[33, 3, 31] → [34, 6, 28] EA	−6.61	563.02	268	CDMS
259309.47 (0.01)	[17, 5, 12] → [17, 4, 13] AE	−4.06	174.54	210	CDMS
259309.76 (0.01)	[17, 5, 12] → [17, 4, 13] EA	−4.06	174.54	140	CDMS
259311.95 (0.01)	[17, 5, 12] → [17, 4, 13] EE	−4.06	174.54	560	CDMS
259314.28 (0.01)	[17, 5, 12] → [17, 4, 13] AA	−4.06	174.54	350	CDMS
	Acetone (CH_3COCH_3)				
244218.91 (0.01)	[20, 5, 15] → [19, 6, 14] AE	−3.32	139.69	82	JPL
244218.91 (0.01)	[20, 6, 15] → [19, 5, 14] AE	−3.32	139.69	250	JPL
244218.92 (0.01)	[20, 5, 15] → [19, 6, 14] EA	−3.32	139.69	160	JPL
244218.92 (0.01)	[20, 6, 15] → [19, 5, 14] EA	−3.32	139.69	160	JPL
245831.34 (0.09)	[13, 10, 3] → [12, 9, 4] EE	−3.80	77.84	432	JPL
246400.99 (0.05)	[34, 7, 28] → [34, 5, 29] EE	−4.17	364.98	1100	JPL
246400.99 (0.05)	[34, 6, 28] → [34, 5, 29] EE	−4.03	364.98	1100	JPL
246400.99 (0.05)	[34, 7, 28] → [34, 6, 29] EE	−4.03	364.98	1100	JPL
246400.99 (0.05)	[34, 6, 28] → [34, 6, 29] EE	−4.17	364.98	1100	JPL
246404.27 (0.01)	[22, 3, 19] → [21, 4, 18] AE	−3.23	149.62	90	JPL
246404.27 (0.01)	[22, 4, 19] → [21, 3, 18] AE	−3.23	149.62	270	JPL
246404.29 (0.01)	[22, 3, 19] → [21, 4, 18] EA	−3.23	149.62	180	JPL
246404.29 (0.01)	[22, 4, 19] → [21, 3, 18] EA	−3.23	149.62	180	JPL
246450.40 (0.01)	[22, 4, 19] → [21, 3, 18] EE	−3.23	149.57	720	JPL
246450.40 (0.01)	[22, 3, 19] → [21, 3, 18] EE	−5.09	149.57	720	JPL
246450.40 (0.01)	[22, 3, 19] → [21, 4, 18] EE	−3.24	149.57	720	JPL
246450.40 (0.01)	[22, 4, 19] → [21, 4, 18] EE	−4.92	149.57	720	JPL
246496.17 (0.46)	[25, 14, 12] → [24, 15, 9] AE	−5.01	257.11	100	JPL
246496.47 (0.02)	[22, 3, 19] → [21, 4, 18] AA	−3.23	149.51	270	JPL
246496.47 (0.02)	[22, 4, 19] → [21, 3, 18] AA	−3.23	149.51	450	JPL
246714.12 (0.05)	[9, 8, 1] → [8, 5, 4] EA	−5.84	40.59	76	JPL
246714.94 (0.05)	[32, 4, 28] → [32, 4, 29] EA	−3.97	305.61	260	JPL
246714.94 (0.05)	[32, 5, 28] → [32, 3, 29] EA	−3.97	305.61	260	JPL
246715.04 (0.05)	[32, 5, 28] → [32, 4, 29] AE	−3.97	305.61	390	JPL
246715.04 (0.05)	[32, 4, 28] → [32, 3, 29] EA	−3.97	305.61	130	JPL
246719.92 (0.04)	[33, 6, 28] → [33, 4, 29] EE	−5.62	344.85	1100	JPL
246719.92 (0.04)	[33, 5, 28] → [33, 4, 29] EE	−3.87	344.85	1100	JPL
246719.92 (0.04)	[33, 6, 28] → [33, 5, 29] EE	−3.87	344.85	1100	JPL
246719.92 (0.04)	[33, 5, 28] → [33, 5, 29] EE	−5.61	344.85	1100	JPL
261818.11 (0.01)	[20, 7, 13] → [19, 8, 12] EA	−3.31	151.17	160	JPL
261818.17 (0.01)	[20, 7, 13] → [19, 8, 12] AE	−3.31	151.17	82	JPL
261819.09 (0.01)	[20, 8, 13] → [19, 7, 12] EA	−3.31	151.17	160	JPL
261819.17 (0.01)	[20, 8, 13] → [19, 7, 12] AE	−3.31	151.17	250	JPL
	Methyl cyanide (CH_3CN)				
257507.56 (0.01)	[N, K]=[14, 2] → [13, 2]	−3.00	121.28	58	JPL
257522.43 (0.01)	[N, K]=[14, 1] → [13, 1]	−2.99	99.84	58	JPL
257527.38 (0.01)	[N, K]=[14, 0] → [13, 0]	−2.99	92.70	58	JPL

Table B1
(Continued)

Frequency (MHz)	Transition[a]	log(Einstein-A)	E_u (K)	g_u	Reference
		Acetaldehyde (CH_3CHO $v_t = 0$)			
246330.73 (0.01)	[15, 3, 13] → [15, 2, 14] A	−4.29	131.49	62	JPL
260530.40 (0.01)	[14, 1, 14] → [13, 1, 13] E	−3.20	96.39	58	JPL
260544.02 (0.01)	[14, 1, 14] → [13, 1, 13] A	−3.20	96.32	58	JPL
260547.46 (2.07)	[9, 4, 5] → [9, 3, 7] E, $v_t = 2$	−6.06	456.38	38	JPL
		gauche-Ethanol (g-C_2H_5OH)			
246414.76 (0.05)	[14, 3, 11] → [13, 3, 10] $v_t = 0 \rightarrow 0$	−3.89	155.72	29	JPL
246524.28 (0.01)	[13, 2, 12] → [12, 1, 12] $v_t = 0 \rightarrow 1$	−4.50	136.95	27	JPL
246658.18 (0.01)	[32, 5, 28] → [32, 4, 29] $v_t = 0 \rightarrow 0$	−6.33	527.94	65	JPL
246662.98 (0.01)	[4, 2, 3] → [3, 1, 3] $v_t = 1 \rightarrow 0$	−4.36	74.77	9	JPL
259322.64 (0.01)	[14, 3, 11] → [13, 2, 11] $v_t = 0 \rightarrow 1$	−4.39	155.72	29	JPL
260457.73 (0.01)	[15. 4. 12] → [14, 4, 11] $v_t = 1 \rightarrow 1$	−3.83	181.10	31	JPL
		trans-Ethanol (C_2H_5OH)			
246663.62 (0.05)	[24, 1, 23] → [24, 0, 24]	−3.73	252.35	49	JPL
261815.99 (0.05)	[28, 3, 26] → [28, 2, 27]	−3.96	350.98	57	JPL
		Glycolaldehyde (*cis*-CH_2OHCHO)			
246773.09 (0.02)	[30, 2, 28] → [30, 1, 29]	−4.04	252.68	61	CDMS
246778.28 (0.02)	[30, 3, 28] → [30, 2, 29]	−4.04	252.68	61	CDMS
262056.78 (0.01)	[25, 2, 24] → [24, 1, 23]	−3.34	158.25	51	CDMS
261795.48 (0.01)	[25, 11, 14] → [25, 10, 15]	−3.57	254.23	51	CDMS
261798.96 (0.01)	[25, 11, 15] → [25, 10, 16]	−3.57	254.23	51	CDMS
		Methyl cyanide (CH_2DCN)			
259315.51 (0.01)	[15, 1, 15] → [14, 1, 14]	−2.82	104.97	31	CDMS
260523.05 (0.01)	[15, 2, 13] → [14, 2, 12]	−2.82	121.60	31	CDMS
		Ethyl cyanide (CH_3CH_2CN)			
246268.74 (0.01)	[27, 2, 25] → [26, 2, 24]	−2.90	169.80	55	CDMS
246421.92 (0.01)	[28, 2, 27] → [27, 2, 26]	−2.90	177.26	57	CDMS
246548.70 (0.01)	[27, 3, 24] → [26, 3, 23]	−2.90	174.06	55	CDMS
260535.69 (0.05)	[29, 5, 25] → [28, 5, 24]	−2.84	215.06	59	CDMS
		Formamide (NH_2CHO)			
243521.04 (0.01)	[12, 1, 12] → [11, 1, 11]	−2.98	79.19	25	CDMS
		Formic acid (*t*-HCOOH)			
262103.48 (0.01)	[12, 0, 12] → [11, 0, 11]	−3.69	82.77	25	CDMS

Notes.
[a] The typical quantum numbers are listed as [J, K_a, K_c] unless specified.
[b] The quantum numbers are [N, J, F].

Appendix C
Estimation of the Column and Volume Gas Density

The continuum brightness temperature indirectly measures the gas column density assuming an optically thin emission. Within the extraction region for the 1D spectra, we can estimate the gas column density from the averaged continuum brightness temperature using

$$N_{\rm gas}({\rm g\ cm^{-2}}) = \frac{R_{\rm g2d} < I_\nu >}{\kappa_\nu B_\nu(T_{\rm d})}$$
$$N_{\rm gas}({\rm cm^{-2}}) = \frac{R_{\rm g2d} < I_\nu >}{\kappa_\nu B_\nu(T_{\rm d}) \mu m_{\rm H}}, \quad \text{(C1)}$$

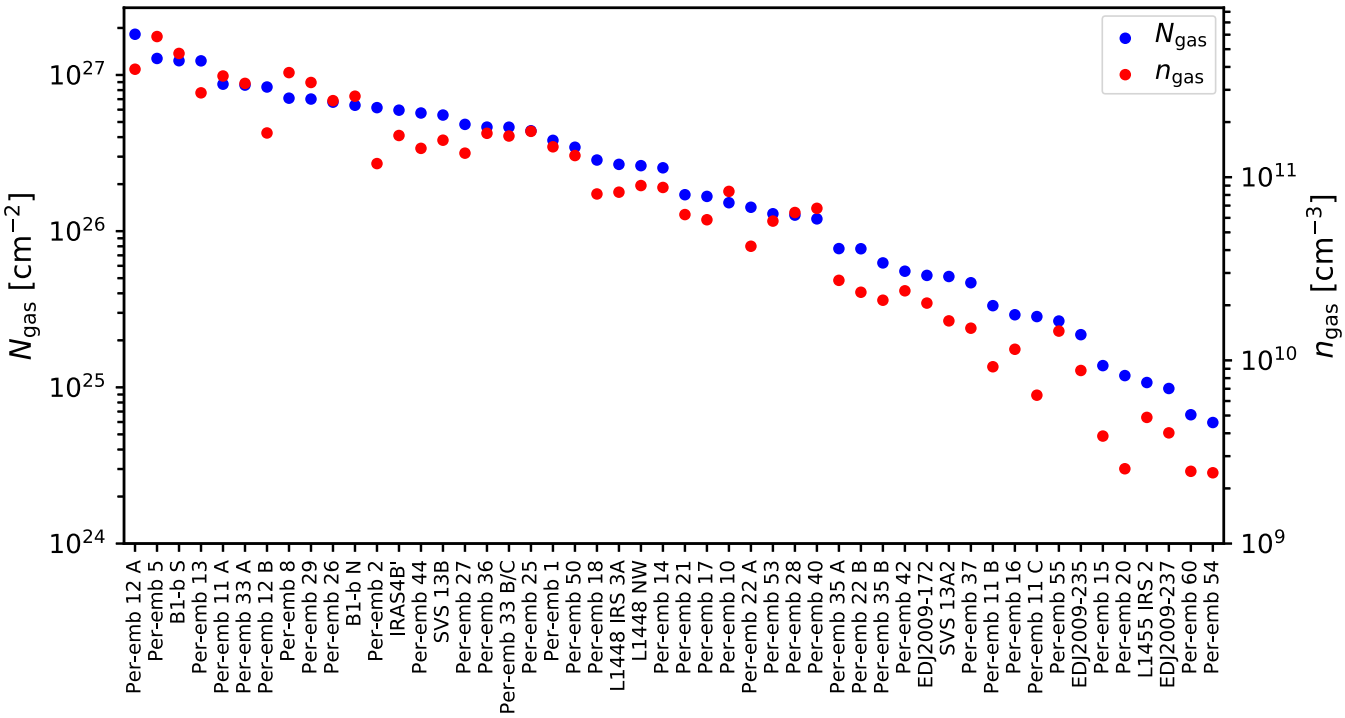

Figure 18. The derived gas column and volume densities for the PEACHES sample sorted by their gas column density.

where R_{g2d} is the gas-to-dust mass ratio of 100, $< I_\nu >$ is the averaged intensity, κ_ν is the dust opacity, $B_\nu(T_d)$ is the Planck function at T_d, which is assumed to be 30 K, and μ is the mean molecular weight of 2.37. We assume a frequency of 250 GHz. Furthermore, we can estimate that the volume density assuming the emitting gas has the same spatial extent along the line of sight as that along the plane of sky. Figure 18 shows the estimated column and volume gas densities of the PEACHES sample.

Appendix D
Excitation Temperatures

D.1. CH_3OH

The excitation temperature is a key parameter for modeling the COM spectra. For most of the identified COMs, our observations only cover one transition or a few blended transitions, making their excitation temperature unconstrained. Thus we assume excitation temperatures ranging from 100 to 300 K in our spectral modeling (Section 3.4). Fortunately, a few molecules have several transitions detected in our observations, such as CH_3OH and CH_3OCHO, allowing us to verify the assumption of the excitation temperature.

Although the difference in the spectral coverage of the continuum spectral window results in different combinations of transitions, our spectra cover three CH_3OH transitions whose upper energy ranges from ∼50 K to ∼500 K, allowing us to estimate the rotational temperature (T_{rot}) of CH_3OH as a proxy of the excitation temperature (T_{ex}). To construct the CH_3OH rotational diagram, we fit the CH_3OH emission with a Gaussian profile; then, we estimated the T_{rot} by fitting a linear line to the rotational diagram (e.g., Goldsmith & Langer 1999). We further assumed that the E- and A-species of CH_3OH have the same rotational temperature so that a single temperature component can describe the rotational diagram, where the statistical weights due to the nuclear spins were considered. This derivation assumes no optical depth correction because we only have three transitions to fit a straight line that has two parameters. The CH_3OH emission at 243915 MHz may be affected by optical depth, especially in Per-emb 44, Per-emb 12 B, Per-emb 18, and Per-emb 29. Therefore we excluded the emission between 243914 MHz and 342918 MHz in the Gaussian fitting to minimize the impact of the optical depth. Figure 19 shows the rotational diagram of Per-emb 22 B along with the fitted rotational temperature. The derived rotational temperature of CH_3OH ranges from 140 to 350 K, consistent with our assumption of T_{ex} for the spectral modeling (Table D1).

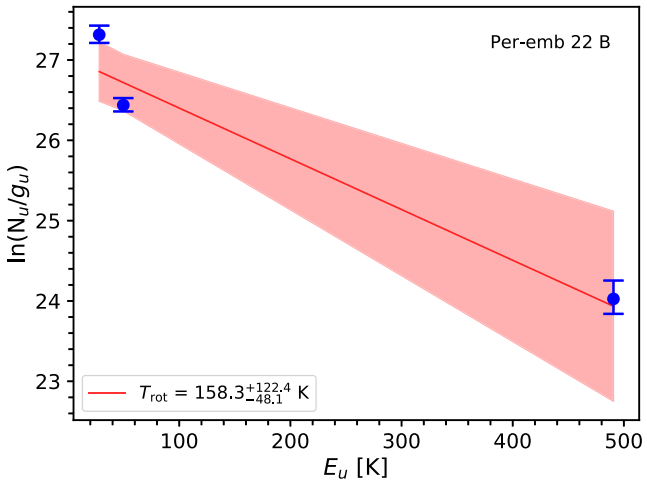

Figure 19. The CH_3OH rotational diagram for Per-emb 22B and the fitted rotational temperature. The shaded red region indicates the uncertainty of the fitting.

Table D1
Rotational Temperatures of CH_3OH

Source	T_{rot} (K)
Per-emb 26	120^{+70}_{-30}
Per-emb 22 A	190^{+60}_{-40}
Per-emb 22 B	160^{+120}_{-50}
Per-emb 20	170^{+70}_{-40}
Per-emb 44	200^{+10}_{-10}
SVS 13 A2	190^{+70}_{-40}
Per-emb 12 B	170^{+20}_{-10}
Per-emb 13	210^{+110}_{-50}
Per-emb 27	190^{+100}_{-50}
Per-emb 21	150^{+10}_{-10}
Per-emb 35 A	140^{+110}_{-40}
Per-emb 18	360^{+140}_{-80}
B1-bS	250^{+290}_{-90}
Per-emb 11 A	240^{+50}_{-40}
Per-emb 11 C	310^{+340}_{-100}
Per-emb 29	190^{+10}_{-10}

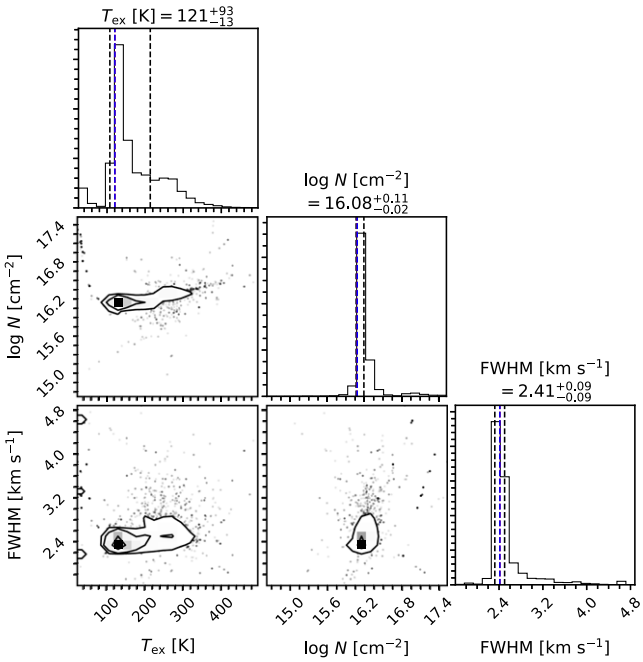

Figure 20. The posterior distributions of the MCMC fitting of the CH_3OCHO emission toward B1-b S.

D.2. CH_3OCHO

Of the identified COMs, CH_3OCHO has more than 10 detected transitions. Thus, we can use the spectra of CH_3OCHO to test our assumption of T_{ex}. With many transitions detected, we can employ a more complex model to constrain the column density and the T_{ex} of CH_3OCHO. We used the XCLASS model described in Section 3.4, which includes the effect of optical depth. The model was optimized with the MCMC method (see description in Section 3.4) instead of a combination of genetic and Levenberg–Marquardt χ^2 minimization to characterize the uncertainties of the fitted properties. Table D2 lists the sources that have sufficient detections of CH_3OCHO and the derived properties of CH_3OCHO. The best-fitting temperatures range from 100-300 K, consistent with our assumption of the excitation temperatures. Figure 20 shows an example of the posterior distributions of the fitting parameters toward B1-b S. The posterior distribution of the excitation temperature has a longer tail toward high temperature, an upper averaged uncertainty of 71.6 K compared to a lower averaged uncertainty of 29.3 K.

Table D2
MCMC Fitting of Methyl Formate

Source	Temperature (K)	log($\mathcal{N}$)[a] (cm^{-2})	Line Width[b] (km s^{-1})	Line Count
Per-emb 26	80^{+50}_{-10}	15.9	$4.8^{+0.2}_{-0.6}$	17
Per-emb 44	210^{+10}_{-20}	17.2	3.8 ± 0.1	17
Per-emb 12 B	200^{+50}_{-10}	16.9	2.4 ± 0.1	17
Per-emb 13	220^{+40}_{-10}	16.6	2.1 ± 0.1	16
Per-emb 27	250^{+40}_{-20}	17.0	$4.2^{+0.1}_{-0.2}$	15
B1-b S	120^{+100}_{-10}	16.1	2.4 ± 0.1	12
Per-emb 29	190^{+60}_{-10}	16.7	3.5 ± 0.1	14
Per-emb 11 A	330^{+60}_{-160}	16.0	$2.4^{+0.2}_{-0.1}$	12

Notes.
[a] The fitting uncertainty is smaller than the calibration uncertainty of 10%. Thus, a 10% uncertainty should be adopted for the fitted column densities.
[b] When the fitting uncertainty is smaller than the channel width, an uncertainty of the channel width, ~0.1 km s^{-1}, is adopted.

Appendix E
The Spectra of C_2H

The C_2H spectra toward the continuum emission have irregular line profiles. Some spectra have strong self-absorption, while some spectra only show blueshifted emission. Due to the absorption and irregular line profile, the XCLASS fitting routine often fails to faithfully reproduce the observed C_2H spectra. C_2H can easily form in the outflow cavity wall due to the abundant CH_4 sublimated from dust grains as well as C^+ ionized by the UV radiation. Thus, the C_2H spectra can have a broad line width and multiple components. Furthermore, the morphology of the C_2H emission traces the outflows, making our extraction from the continuum emission not ideal for representing the nature of the C_2H emission. Figure 21 shows the spectra of C_2H toward the PEACHES sample.

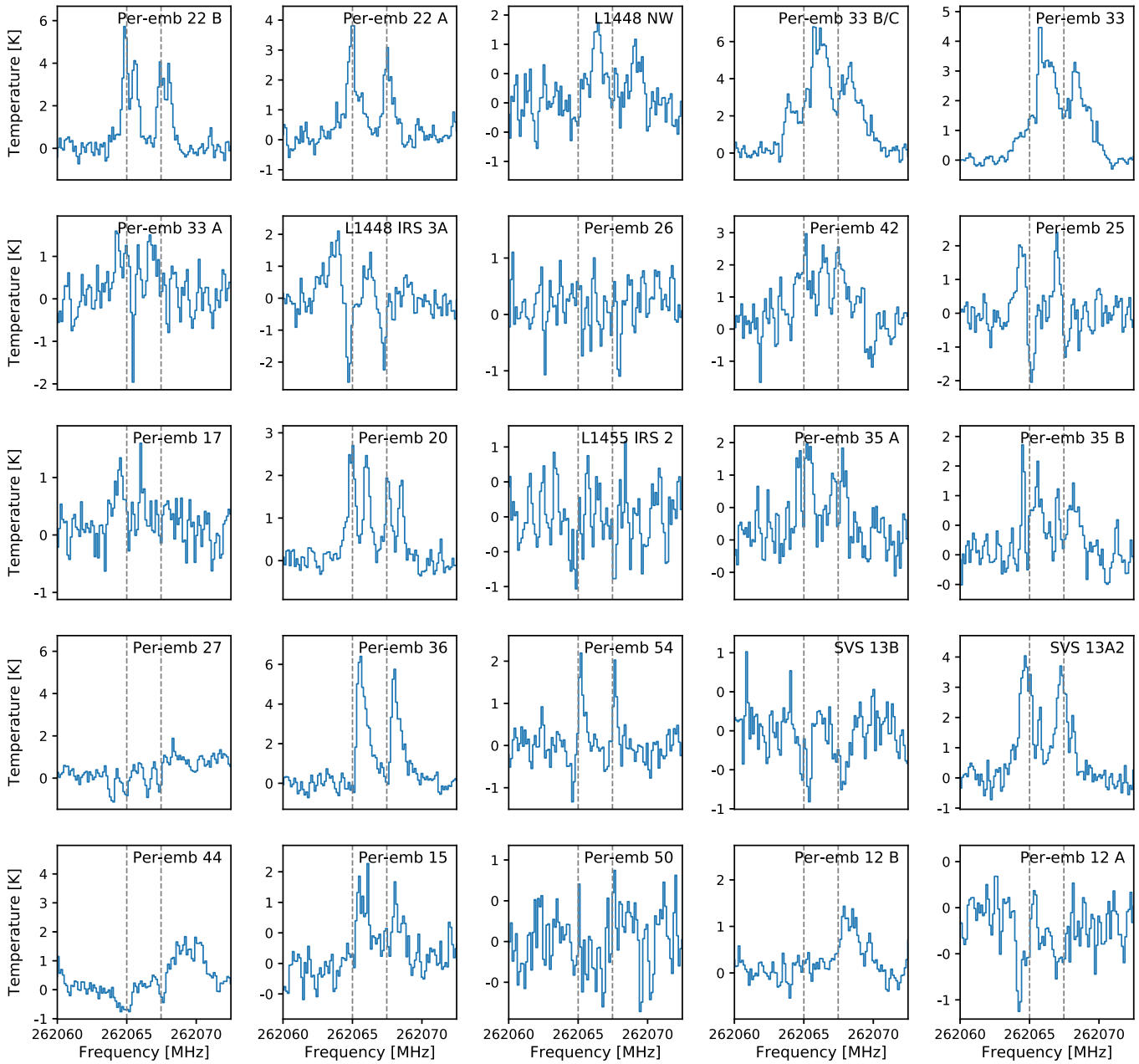

Figure 21. The C_2H spectra of all PEACHES sources extracted from the region of the continuum source. The vertical dashed lines indicate the rest frequencies of C_2H transitions.

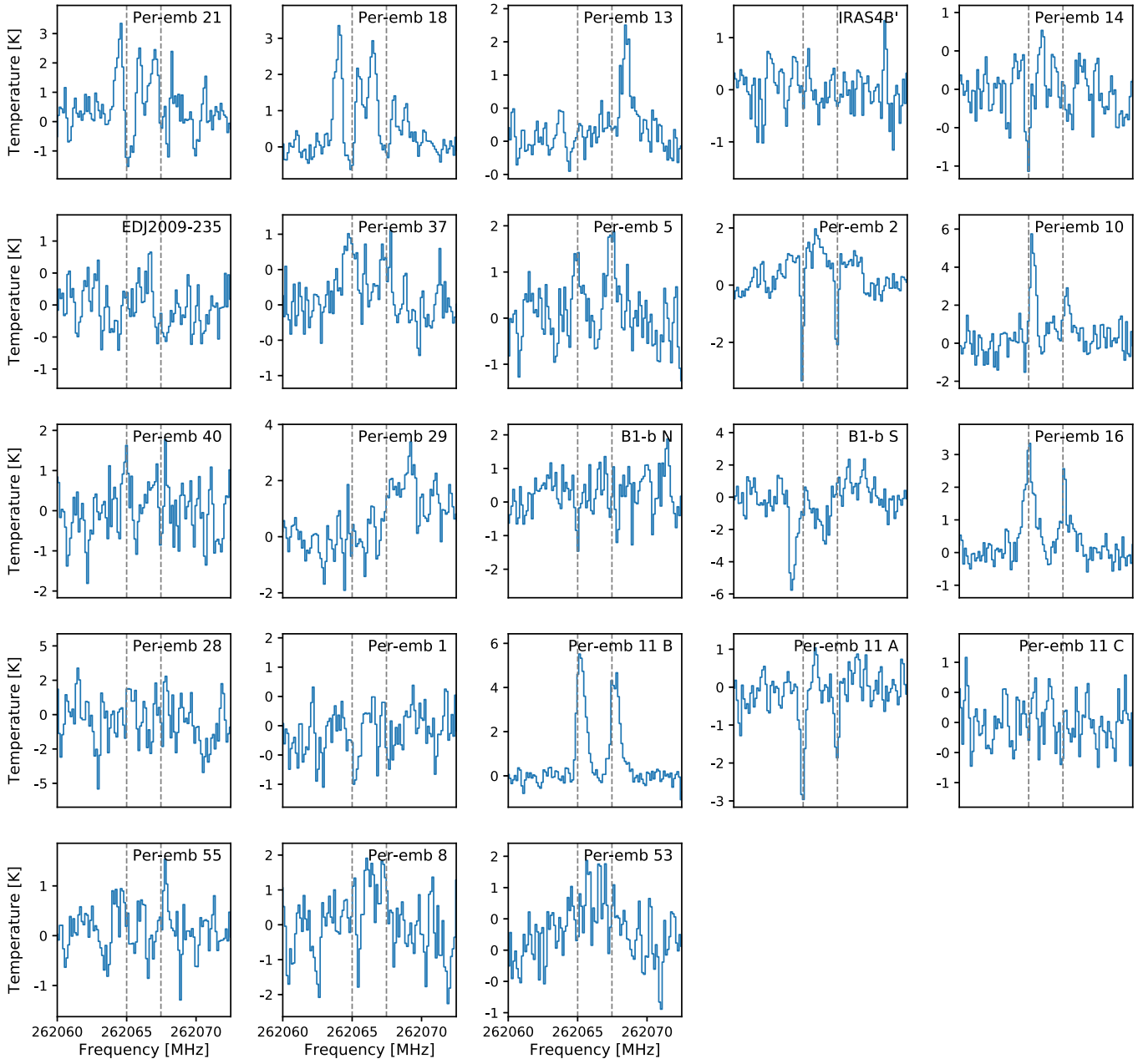

Figure 21. (Continued.)

Appendix F
The Effect of Source Size and Beam Dilution on Column Densities

Our modeling assumes a fixed 0.″5 source size to estimate the column densities because most of the emission of COMs is unresolved or marginally resolved in our observations. To study the impact of this assumption on the resulting correlation and scatter in the derived column densities, we tested whether the correlations shown in Section 4.2.2 still persist in two extreme cases, the column density averaged over the size of the continuum source, and assuming that COMs strictly emit from the $T = 100$ K radius. For the case of the averaged column density, we simply multiplied the modeled column density ($N_{0.''5}$) by $\Omega_{0.''5}/\Omega_{\rm cont.}$, where Ω is the solid angle. Figure 22 shows the averaged column densities of the four most frequently detected COMs. The scatter in the averaged column densities is about 1–3 orders of magnitudes, similar to that in the modeled column densities assuming a size of 0.″5. When we assume that COMs emit from the $T = 100$ K radius where water ice desorbs, we need to multiply the modeled column density by $\Omega_{0.''5}/\Omega_{100\,\rm K}$. Using the equation for hot cores in Bisschop et al. (2007), we have

$$R_{T=100\,\rm K} \approx 15.4\sqrt{\frac{L}{L_\odot}}\,\rm au. \quad \text{(F1)}$$

Thus, $\Omega_{0.''5}/\Omega_{100\,\rm K}$ is proportional to L^{-1}. Figure 23 shows the modeled column densities of the four most frequently detected COMs normalized by $L_{\rm bol}$. The scatter of the normalized column densities is still about 1–3 orders of magnitude, suggesting that the intrinsic variation in the number of COMs

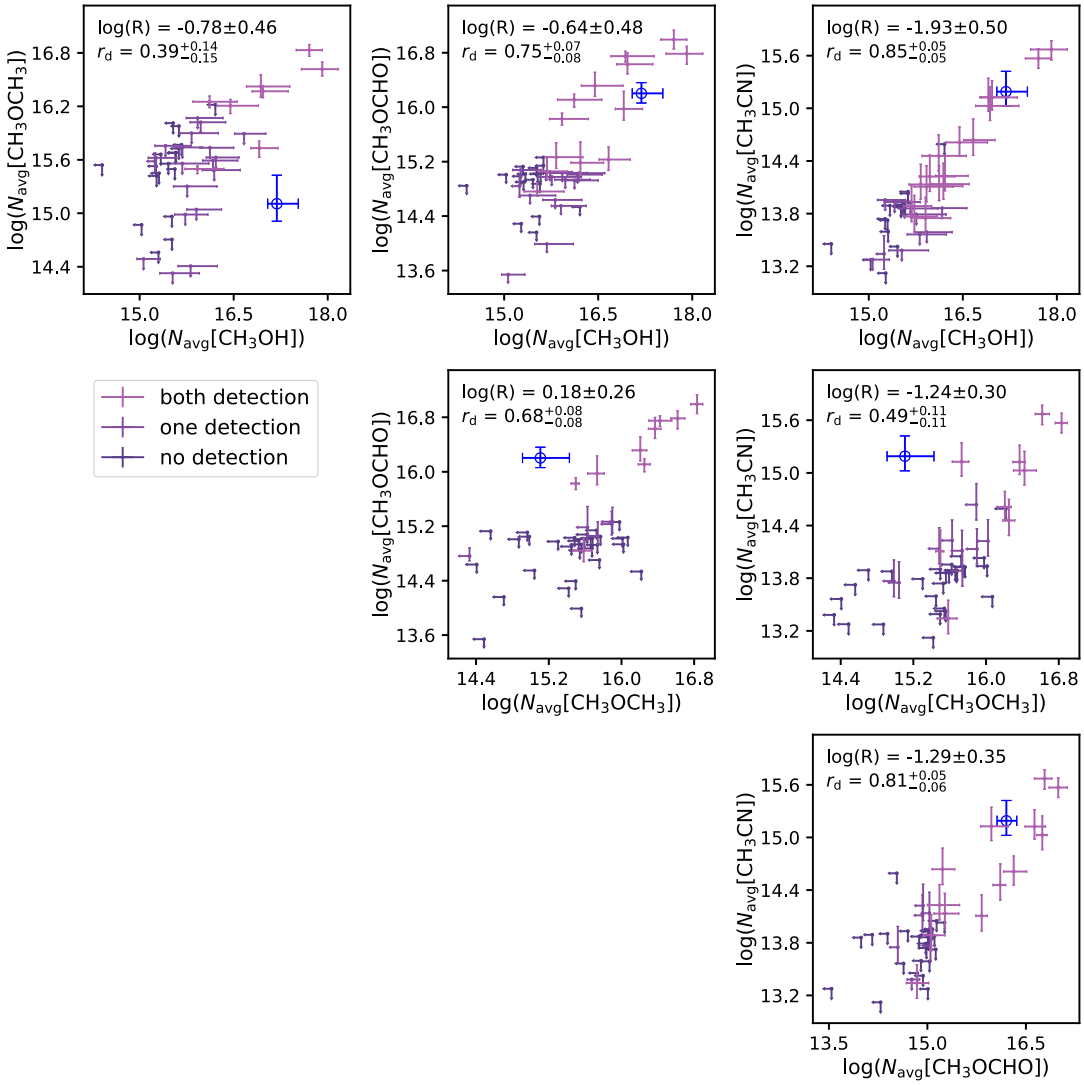

Figure 22. Corner plot of the correlations of the averaged column densities between CH_3OH, CH_3CN, CH_3OCHO, and CH_3OCH_3. The legends and the color code follow the legends in Figures 11 and 12.

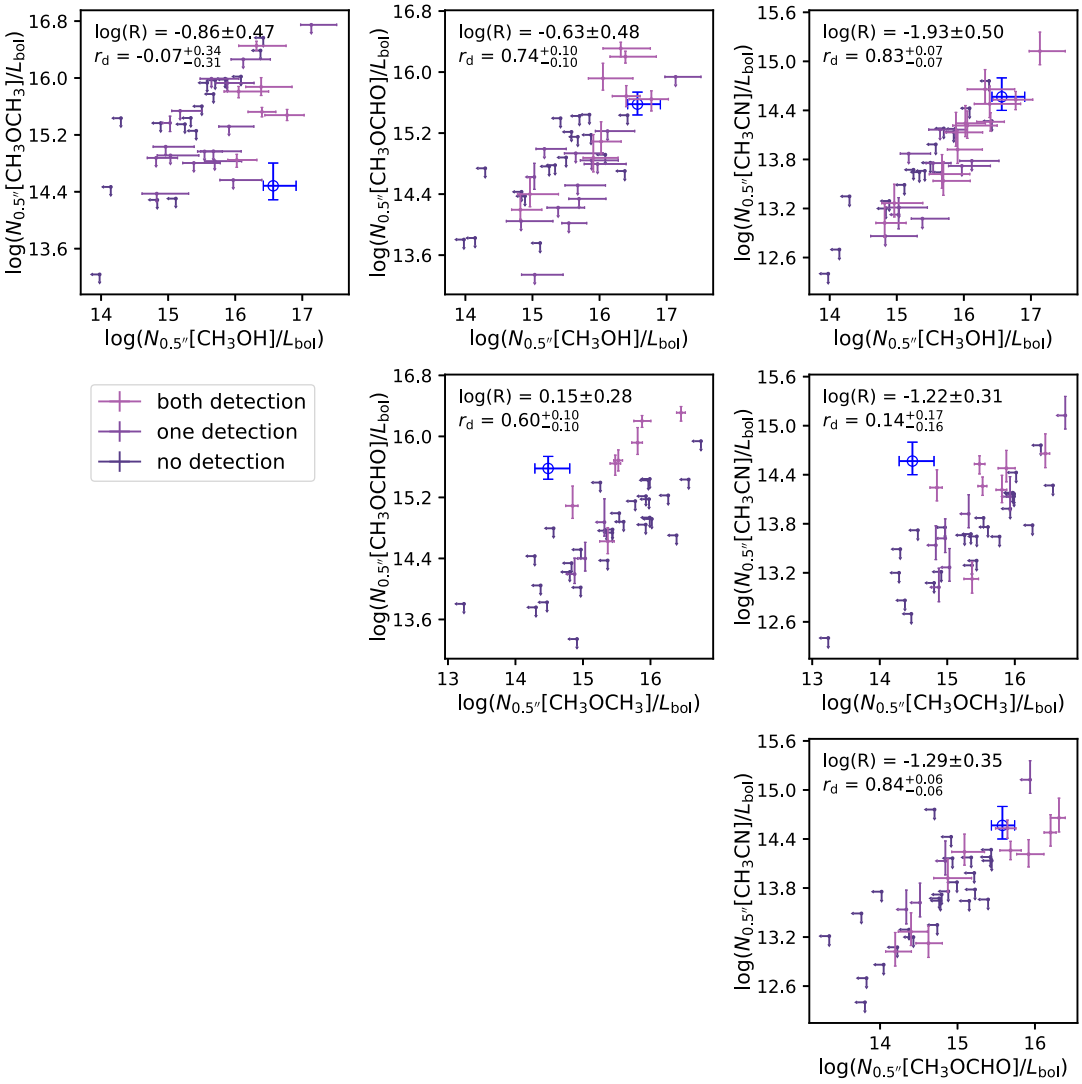

Figure 23. Corner plot of the correlations of the column densities normalized by L_{bol} between CH_3OH, CH_3CN, CH_3OCHO, and CH_3OCH_3. The legends and the color code follow the legends in Figures 11 and 12.

dominates the scatter in the column density. We also note that the L_{bol} may not represent the protostellar luminosity due to the bias of the inclination of the protostars.

ORCID iDs

Yao-Lun Yang https://orcid.org/0000-0001-8227-2816
Nami Sakai https://orcid.org/0000-0002-3297-4497
Yichen Zhang https://orcid.org/0000-0001-7511-0034
Ziwei E. Zhang https://orcid.org/0000-0002-9927-2705
Aya E. Higuchi https://orcid.org/0000-0002-9221-2910
Ana López-Sepulcre https://orcid.org/0000-0002-6729-3640
Mathilde Bouvier https://orcid.org/0000-0003-0167-0746
Cecilia Ceccarelli https://orcid.org/0000-0001-9664-6292
Tomoya Hirota https://orcid.org/0000-0003-1659-095X
Muneaki Imai https://orcid.org/0000-0002-5342-6262
Yoko Oya https://orcid.org/0000-0002-0197-8751
Takeshi Sakai https://orcid.org/0000-0003-4521-7492
Yoshimasa Watanabe https://orcid.org/0000-0002-9668-3592

References

Aikawa, Y. 2013, ChRv, 113, 8961
Aikawa, Y., Furuya, K., Yamamoto, S., & Sakai, N. 2020, ApJ, 897, 110
Alekseev, E. A., Dyubko, S. F., Ilyushin, V. V., & Podnos, S. V. 1996, JMpSp, 176, 316
Amano, T., & Hirota, E. 1974, JMoSp, 53, 346
Arce, H. G., Santiago-García, J., Jørgensen, J. K., Tafalla, M., & Bachiller, R. 2008, ApJL, 681, L21
Artur de la Villarmois, E., Jørgensen, J. K., Kristensen, L. E., et al. 2019, A&A, 626, A71
Astropy Collaboration, Price-Whelan, A. M., Sipőcz, B. M., et al. 2018, AJ, 156, 123
Bachiller, R., Pérez Gutiérrez, M., Kumar, M. S. N., & Tafalla, M. 2001, A&A, 372, 899
Balucani, N., Ceccarelli, C., & Taquet, V. 2015, MNRAS, 449, L16
Bellet, J., Samson, C., Steenbeckliers, G., & Wertheimer, R. 1971, JMoSt, 9, 49
Belloche, A., Maury, A. J., Maret, S., et al. 2020, A&A, 635, A198
Bergner, J. B., Martín-Doménech, R., Öberg, K. I., et al. 2019, ESC, 3, 1564
Bergner, J. B., Öberg, K. I., Garrod, R. T., & Graninger, D. M. 2017, ApJ, 841, 120
Bianchi, E., Codella, C., Ceccarelli, C., et al. 2019, MNRAS, 483, 1850
Bisschop, S. E., Jørgensen, J. K., van Dishoeck, E. F., & de Wachter, E. B. M. 2007, A&A, 465, 913

Blanco, S., López, J. C., Lesarri, A., & Alonso, J. L. 2006, JAChS, 128, 12111
Bocquet, R., Demaison, J., Cosléou, J., et al. 1999, JMoSp, 195, 345
Bogey, M., Demuynck, C., & Destombes, J. L. 1986, CPL, 125, 383
Bottinelli, S., Ceccarelli, C., Lefloch, B., et al. 2004a, ApJ, 615, 354
Bottinelli, S., Ceccarelli, C., Neri, R., et al. 2004b, ApJL, 617, L69
Bottinelli, S., Ceccarelli, C., Williams, J. P., & Lefloch, B. 2007, A&A, 463, 601
Bouvier, M., López-Sepulcre, A., Ceccarelli, C., et al. 2020, A&A, 636, A19
Brauer, C. S., Pearson, J. C., Drouin, B. J., & Yu, S. 2009, ApJS, 184, 133
Butler, R. A. H., De Lucia, F. C., Petkie, D. T., et al. 2001, ApJS, 134, 319
Calcutt, H., Jørgensen, J. K., Müller, H. S. P., et al. 2018, A&A, 616, A90
Carney, M. T., Yıldız, U. A., Mottram, J. C., et al. 2016, A&A, 586, A44
Carvajal, M., Willaert, F., Demaison, J., & Kleiner, I. 2007, JMoSp, 246, 158
Caselli, P., Hasegawa, T. I., & Herbst, E. 1993, ApJ, 408, 548
Caux, E., Kahane, C., Castets, A., et al. 2011, A&A, 532, A23
Cazaux, S., Tielens, A. G. G. M., Ceccarelli, C., et al. 2003, ApJL, 593, L51
Cazzoli, G., Cludi, L., Cotti, G., Esposti, C. D., & Dore, L. 1994, JMoSp, 167, 468
Cazzoli, G., & Puzzarini, C. 2005, JMoSp, 233, 280
Cazzoli, G., & Puzzarini, C. 2006, JMoSp, 240, 153
Ceccarelli, C. 2004, in ASP Conf. Ser. 323, Star Formation in the Interstellar Medium: In Honor of David Hollenbach, ed. D. Johnston et al. (San Francisco, CA: ASP), 195
Ceccarelli, C., Caselli, P., Fontani, F., et al. 2017, ApJ, 850, 176
Ceccarelli, C., Caselli, P., Herbst, E., Tielens, A., & Caux, E. 2007, Protostars and Planets V (Tucson, AZ: Univ. Arizona Press), 47
Chen, H., Myers, P. C., Ladd, E. F., & Wood, D. O. S. 1995, ApJ, 445, 377
Clark, W. W., & De Lucia, F. C. 1976, JMoSp, 60, 332
Codella, C., Ceccarelli, C., Bianchi, E., et al. 2020, A&A, 635, A17
Collings, M. P., Anderson, M. A., Chen, R., et al. 2004, MNRAS, 354, 1133
Csengeri, T., Bontemps, S., Wyrowski, F., et al. 2018, A&A, 617, A89
Curtis, E. I., Richer, J. S., Swift, J. J., & Williams, J. P. 2010, MNRAS, 408, 1516
De Simone, M., Ceccarelli, C., Codella, C., et al. 2020, ApJL, 896, L3
Drozdovskaya, M. N., Walsh, C., Visser, R., Harsono, D., & van Dishoeck, E. F. 2014, MNRAS, 445, 913
Drozdovskaya, M. N., Walsh, C., Visser, R., Harsono, D., & van Dishoeck, E. F. 2015, MNRAS, 451, 3836
Dunham, M. M., Arce, H. G., Allen, L. E., et al. 2013, AJ, 145, 94
Dunham, M. M., Stutz, A. M., Allen, L. E., et al. 2014, in Protostars and Planets VI, ed. H. Beuther et al., Vol. 195 (Tucson, AZ: Univ. Arizona Press), 195
Endres, C. P., Drouin, B. J., Pearson, J. C., et al. 2009, A&A, 504, 635
Endres, C. P., Schlemmer, S., Schilke, P., Stutzki, J., & Müller, H. S. P. 2016, JMoSp, 327, 95
Evans, N. J., II, Dunham, M. M., Jørgensen, J. K., et al. 2009, ApJS, 181, 321
Favre, C., Fedele, D., Semenov, D., et al. 2018, ApJL, 862, L2
Feng, S., Beuther, H., Henning, T., et al. 2015, A&A, 581, A71
Ferrero, S., Zamirri, L., Ceccarelli, C., et al. 2020, ApJ, 904, 11
Fisher, J., Paciga, G., Xu, L.-H., et al. 2007, JMoSp, 245, 7
Foreman-Mackey, D., Hogg, D. W., Lang, D., & Goodman, J. 2013, PASP, 125, 306
Friedel, D. N., & Snyder, L. E. 2008, ApJ, 672, 962
Friesen, R. K., Pineda, J. E., Rosolowsky, E., et al. 2017, ApJ, 843, 63
Fuchs, U., Bruenken, S., Fuchs, G. W., et al. 2004, ZNatA, 59, 861
Garrod, R. T. 2013, ApJ, 765, 60
Garrod, R. T., & Herbst, E. 2006, A&A, 457, 927
Garrod, R. T., Wakelam, V., & Herbst, E. 2007, A&A, 467, 1103
Garrod, R. T., Widicus Weaver, S. L., & Herbst, E. 2008, ApJ, 682, 283
Goldsmith, P. F., & Langer, W. D. 1999, ApJ, 517, 209
Graninger, D. M., Wilkins, O. H., & Öberg, K. I. 2016, ApJ, 833, 125
Grassi, T., Bovino, S., Caselli, P., et al. 2020, A&A, 643, A155
Gratier, P., Majumdar, L., Ohishi, M., et al. 2016, ApJS, 225, 25
Groner, P., Albert, S., Herbst, E., et al. 2002, ApJS, 142, 145
Guélin, M., Brouillet, N., Cernicharo, J., Combes, F., & Wootten, A. 2008, Ap&SS, 313, 45
Hatchell, J., Fuller, G. A., Richer, J. S., Harries, T. J., & Ladd, E. F. 2007, A&A, 468, 1009
Hatchell, J., Richer, J. S., Fuller, G. A., et al. 2005, A&A, 440, 151
Helminger, P. A., & De Lucia, F. C. 1985, JMoSp, 111, 66
Herbst, E., & van Dishoeck, E. F. 2009, ARA&A, 47, 427
Higuchi, A. E., Sakai, N., Watanabe, Y., et al. 2018, ApJS, 236, 52
Hirota, T., Bushimata, T., Choi, Y. K., et al. 2008, PASJ, 60, 37
Ilyushin, V., Kryvda, A., & Alekseev, E. 2009, JMoSp, 255, 32
Imai, M., Oya, Y., Sakai, N., et al. 2019, ApJL, 873, L21
Imai, M., Sakai, N., Oya, Y., et al. 2016, ApJL, 830, L37
Jaber, A. A., Ceccarelli, C., Kahane, C., & Caux, E. 2014, ApJ, 791, 29
Jaber Al-Edhari, A., Ceccarelli, C., Kahane, C., et al. 2017, A&A, 597, A40
Jacobsen, S. K., Jørgensen, J. K., Di Francesco, J., et al. 2019, A&A, 629, A29
Jørgensen, J. K., Johnstone, D., Kirk, H., et al. 2008, ApJ, 683, 822
Jørgensen, J. K., Müller, H. S. P., Calcutt, H., et al. 2018, A&A, 620, A170
Jørgensen, J. K., van der Wiel, M. H. D., Coutens, A., et al. 2016, A&A, 595, A117
Kaifu, N., Ohishi, M., Kawaguchi, K., et al. 2004, PASJ, 56, 69
Kim, H., Keller, R., & Gwinn, W. D. 1962, JChPh, 37, 2748
Kleiner, I., Lovas, F. J., & Godefroid, M. 1996, JPCRD, 25, 1113
Knee, L. B. G., & Sandell, G. 2000, A&A, 361, 671
Ko, C.-L., Liu, H. B., Lai, S.-P., et al. 2020, ApJ, 889, 172
Kryvda, A. V., Gerasimov, V. G., Dyubko, S. F., Alekseev, E. A., & Motiyenko, R. A. 2009, JMoSp, 254, 28
Kuze, H., Kuga, T., & Shimizu, T. 1982, JMoSp, 93, 248
Laas, J. C., Garrod, R. T., Herbst, E., & Widicus Weaver, S. L. 2011, ApJ, 728, 71
Launhardt, R., Stutz, A. M., Schmiedeke, A., et al. 2013, A&A, 551, A98
Law, C. J., Öberg, K. I., Bergner, J. B., & Graninger, D. 2018, ApJ, 863, 88
Lee, C.-F., Hirano, N., Palau, A., et al. 2009, ApJ, 699, 1584
Lee, C.-F., Li, Z.-Y., Ho, P. T. P., et al. 2017, ApJ, 843, 27
Lee, J.-E., Lee, S., Baek, G., et al. 2019, NatAs, 3, 314
Lefloch, B., Bachiller, R., Ceccarelli, C., et al. 2018, MNRAS, 477, 4792
Lefloch, B., Ceccarelli, C., Codella, C., et al. 2017, MNRAS, 469, L73
Lerner, R. G., Dailey, B. P., & Friend, J. P. 1957, JChPh, 26, 680
López-Sepulcre, A., Sakai, N., Neri, R., et al. 2017, A&A, 606, A121
Lovas, F. J. 1985, JPCRD, 14, 395
Lovas, F. J., Suenram, R. D., Ogata, T., & Yamamoto, S. 1992, ApJ, 399, 325
Luhman, K. L., Esplin, T. L., & Loutrel, N. P. 2016, ApJ, 827, 52
Maeda, A., De Lucia, F. C., & Herbst, E. 2008, JMoSp, 251, 293
Maiwald, F., Lewen, F., Ahrens, V., et al. 2000, JMoSp, 202, 166
Manigand, S., Jørgensen, J. K., Calcutt, H., et al. 2020, A&A, 635, A48
Marcelino, N., Cernicharo, J., Roueff, E., Gerin, M., & Mauersberger, R. 2005, ApJ, 620, 308
Marcelino, N., Gerin, M., Cernicharo, J., et al. 2018, A&A, 620, A80
McElroy, D., Walsh, C., Markwick, A. J., et al. 2013, A&A, 550, A36
McGuire, B. A. 2018, ApJS, 239, 17
McMullin, J. P., Waters, B., Schiebel, D., Young, W., & Golap, K. 2007, in ASP Conf. Ser. 376, Astronomical Data Analysis Software and Systems XVI, ed. R. A. Shaw, F. Hill, & D. J. Bell (San Francisco, CA: ASP), 127
Miura, H., Yamamoto, T., Nomura, H., et al. 2017, ApJ, 839, 47
Möller, T., Endres, C., & Schilke, P. 2017, A&A, 598, A7
Müller, H. S. P., Drouin, B. J., & Pearson, J. C. 2009, A&A, 506, 1487
Müller, H. S. P., Klaus, T., & Winnewisser, G. 2000, A&A, 357, L65
Müller, H. S. P., Schlöder, F., Stutzki, J., & Winnewisser, G. 2005, JMoSt, 742, 215
Müller, H. S. P., Thorwirth, S., Roth, D. A., & Winnewisser, G. 2001, A&A, 370, L49
Murillo, N. M., van Dishoeck, E. F., Tobin, J. J., & Fedele, D. 2016, A&A, 592, A56
Murillo, N. M., van Dishoeck, E. F., van der Wiel, M. H. D., et al. 2018, A&A, 617, A120
Myers, P. C., & Ladd, E. F. 1993, ApJL, 413, L47
Nagy, Z., Spezzano, S., Caselli, P., et al. 2019, A&A, 630, A136
Neill, J. L., Steber, A. L., Muckle, M. T., et al. 2011, JPCA, 115, 6472
Nguyen, L., Walters, A., Margulès, L., et al. 2013, A&A, 553, A84
Öberg, K. I., Guzmán, V. V., Furuya, K., et al. 2015, Natur, 520, 198
Oesterling, L. C., Albert, S., De Lucia, F. C., Sastry, K. V. L. N., & Herbst, E. 1999, ApJ, 521, 255
Okoda, Y., Oya, Y., Sakai, N., et al. 2018, ApJL, 864, L25
Ortiz-León, G. N., Loinard, L., Dzib, S. A., et al. 2018, ApJ, 865, 73
Oya, Y., Sakai, N., López-Sepulcre, A., et al. 2016, ApJ, 824, 88
Oya, Y., Sakai, N., Sakai, T., et al. 2014, ApJ, 795, 152
Oya, Y., Sakai, N., Watanabe, Y., et al. 2017, ApJ, 837, 174
Pantaleone, S., Enrique-Romero, J., Ceccarelli, C., et al. 2020, ApJ, 897, 56
Patel, D., Margolese, D., & Dyke, T. R. 1979, JChPh, 70, 2740
Pearson, J. C., Brauer, C. S., & Drouin, B. J. 2008, JMoSp, 251, 394
Pearson, J. C., Sastry, K. V. L. N., Herbst, E., & De Lucia, F. C. 1994, ApJS, 93, 589
Pearson, J. C., Sastry, K. V. L. N., Herbst, E., & De Lucia, F. C. 1996, JMoSp, 175, 246
Pearson, J. C., Yu, S., & Drouin, B. J. 2012, JMoSp, 280, 119
Penteado, E. M., Walsh, C., & Cuppen, H. M. 2017, ApJ, 844, 71
Pickett, H. M., Poynter, R. L., Cohen, E. A., et al. 1998, JQSRT, 60, 883
Pineda, J. E., Caselli, P., & Goodman, A. A. 2008, ApJ, 679, 481
Pineda, J. E., Offner, S. S. R., Parker, R. J., et al. 2015, Natur, 518, 213

Plummer, G. M., Herbst, E., De Lucia, F., & Blake, G. A. 1984, ApJS, 55, 633
Plunkett, A. L., Arce, H. G., Corder, S. A., et al. 2013, ApJ, 774, 22
Podio, L., Garufi, A., Codella, C., et al. 2020, A&A, 642, L7
Powell, F. X., & Lide, D. R. 1964, JChPh, 41, 1413
Rabli, D., & Flower, D. R. 2010, MNRAS, 406, 95
Rimola, A., Taquet, V., Ugliengo, P., Balucani, N., & Ceccarelli, C. 2014, A&A, 572, A70
Robitaille, T., Ginsburg, A., Beaumont, C., Leroy, A., & Rosolowsky, E. 2016, Spectral-Cube: Read and Analyze Astrophysical Spectral Data Cubes, Astrophysics Source Code Library v. 0.5.0, ascl:1609.017
Roueff, E., Lis, D. C., van der Tak, F. F. S., Gerin, M., & Goldsmith, P. F. 2005, A&A, 438, 585
Sahu, D., Liu, S.-Y., Su, Y.-N., et al. 2019, ApJ, 872, 196
Sakai, N., Sakai, T., Hirota, T., et al. 2014, Natur, 507, 78
Sakai, N., Sakai, T., Hirota, T., Burton, M., & Yamamoto, S. 2009, ApJ, 697, 769
Sakai, N., Sakai, T., Hirota, T., & Yamamoto, S. 2010, ApJ, 722, 1633
Sakai, N., Sakai, T., & Yamamoto, S. 2006, PASJ, 58, L15
Sakai, N., & Yamamoto, S. 2013, ChRv, 113, 8981
Sastry, K. V. L. N., Helminger, P., Charo, A., Herbst, E., & De Lucia, F. C. 1981, ApJL, 251, L119
Schöier, F. L., van der Tak, F. F. S., van Dishoeck, E. F., & Black, J. H. 2005, A&A, 432, 369
Segura-Cox, D. M., Looney, L. W., Tobin, J. J., et al. 2018, ApJ, 866, 161
Skouteris, D., Balucani, N., Ceccarelli, C., et al. 2018, ApJ, 854, 135
Soma, T., Sakai, N., Watanabe, Y., & Yamamoto, S. 2015, ApJ, 802, 74
Stahler, S. W., & Palla, F. 2004, The Formation of Stars (New York: Wiley)
Stephens, I. W., Bourke, T. L., Dunham, M. M., et al. 2019, ApJS, 245, 21
Stephens, I. W., Dunham, M. M., Myers, P. C., et al. 2018, ApJS, 237, 22
Tercero, B., Cuadrado, S., López, A., et al. 2018, A&A, 620, L6
Tielens, A. G. G. M., & Whittet, D. C. B. 1997, in IAU Symp. 178, Molecules in Astrophysics: Probes & Processes, ed. E. F. van Dishoeck (Cambridge: Cambridge Univ. Press), 45
Tobin, J. J., Looney, L. W., Li, Z.-Y., et al. 2016, ApJ, 818, 73
Tobin, J. J., Looney, L. W., Li, Z.-Y., et al. 2018, ApJ, 867, 43
Trambarulo, R., Clark, A., & Hearns, C. 1958, JChPh, 28, 736
Tychoniec, Ł., Manara, C. F., Rosotti, G. P., et al. 2020, A&A, 640, A19
Tychoniec, Ł., Tobin, J. J., Karska, A., et al. 2018, ApJS, 238, 19
van der Tak, F. F. S., Black, J. H., Schöier, F. L., Jansen, D. J., & van Dishoeck, E. F. 2007, A&A, 468, 627
van Gelder, M. L., Tabone, B., Tychoniec, Ł., et al. 2020, A&A, 639, A87
van't Hoff, M. L. R., Harsono, D., Tobin, J. J., et al. 2020a, ApJ, 901, 166
van't Hoff, M. L. R., Tobin, J. J., Harsono, D., & van Dishoeck, E. F. 2018a, A&A, 615, A83
van't Hoff, M. L. R., Tobin, J. J., Trapman, L., et al. 2018b, ApJL, 864, L23
van't Hoff, M. L. R., van Dishoeck, E. F., Jørgensen, J. K., & Calcutt, H. 2020b, A&A, 633, A7
Vasyunin, A. I., & Herbst, E. 2013, ApJ, 769, 34
Vazart, F., Ceccarelli, C., Balucani, N., Bianchi, E., & Skouteris, D. 2020, MNRAS, 499, 5547
Vrtilek, J. M., Gottlieb, C. A., & Thaddeus, P. 1987, ApJ, 314, 716
Wakelam, V., Loison, J. C., Herbst, E., et al. 2015, ApJS, 217, 20
Wakelam, V., Loison, J. C., Mereau, R., & Ruaud, M. 2017, MolAs, 6, 22
Walsh, C., Loomis, R. A., Öberg, K. I., et al. 2016, ApJL, 823, L10
Watanabe, N., Shiraki, T., & Kouchi, A. 2003, ApJL, 588, L121
Xu, L.-H., Fisher, J., Lees, R. M., et al. 2008, JMoSp, 251, 305
Yang, Y.-L., Evans, N. J., Smith, A. L., et al. 2020, ApJ, 891, 61
Zhang, Y., Higuchi, A. E., Sakai, N., et al. 2018, ApJ, 864, 76
Zucker, C., Speagle, J. S., Schlafly, E. F., et al. 2020, A&A, 633, A51

The Astrophysical Journal, 913:155 (3pp), 2021 June 1 https://doi.org/10.3847/1538-4357/abff4e

Erratum: "The Perseus ALMA Chemistry Survey (PEACHES). I. The Complex Organic Molecules in Perseus Embedded Protostars" (2021, ApJ, 910, 20)

Yao-Lun Yang[1,2], Nami Sakai[2], Yichen Zhang[2], Nadia M. Murillo[2], Ziwei E. Zhang[2], Aya E. Higuchi[3], Shaoshan Zeng[2], Ana López-Sepulcre[4], Satoshi Yamamoto[5], Bertrand Lefloch[4], Mathilde Bouvier[4], Cecilia Ceccarelli[4], Tomoya Hirota[3], Muneaki Imai[5], Yoko Oya[5], Takeshi Sakai[6], and Yoshimasa Watanabe[7]
[1] Department of Astronomy, University of Virginia, Charlottesville, VA 22904-4235, USA; yaolunyang.astro@gmail.com
[2] RIKEN Cluster for Pioneering Research, Wako-shi, Saitama, 351-0106, Japan
[3] National Astronomical Observatory of Japan, Osawa, Mitaka, Tokyo 181-8588, Japan
[4] Univ. Grenoble Alpes, CNRS, Institut de Planétologie et d'Astrophysique de Grenoble (IPAG), F-38000 Grenoble, France
[5] Department of Physics, The University of Tokyo, 7-3-1, Hongo, Bunkyo-ku, Tokyo 113-0033, Japan
[6] Department of Communication Engineering and Informatics, Graduate School of Informatics and Engineering, The University of Electro-Communications, Chofugaoka, Chofu, Tokyo 182-8585, Japan
[7] Shibaura Institute of Technology, 3-9-14 Shibaura, Minato-ku, Tokyo 108-8548, Japan
Received 2021 May 6; published 2021 June 7

We have identified an error in the uncertainties of the fitted column densities of complex organic molecules (Table 5 in the published article). In particular, a few upper or lower uncertainties were underestimated by a factor of 10. A script was used to generate the table from the results of radiative transfer modeling (Section 3.4 in the published article). This script assumed the same order of magnitude for both upper and lower uncertainties, which is true in most cases. In a few cases, for example, the CH_3OH column density in L1448 NW, $2.1^{+0.7}_{-1.1} \times 10^{15}$ cm^{-2}, has different orders of magnitude in its upper and lower uncertainties. Thus, it was erroneously reported as $2.1^{+0.7}_{-0.1} \times 10^{15}$ cm^{-2}, because the script assumed an order of 10^{14} for both uncertainties. This error affects neither the conclusions nor the results and figures in the published article, because the error only occurred in the making of this table. A corrected version of Table 5 is provided here.

Table 5
Column Densities of Molecules

Source	CH_3OH (cm^{-2})	CH_3CN (cm^{-2})	CH_3OCHO (cm^{-2})	CH_3OCH_3 (cm^{-2})	CH_3CHO (cm^{-2})	C_2H_5OH (cm^{-2})
L1448 NW	$2.1^{+0.7}_{-1.1} \times 10^{15}$	$<1.0 \times 10^{14}$	$<1.4 \times 10^{15}$	$<4.8 \times 10^{15}$	$<6.9 \times 10^{14}$	$<3.3 \times 10^{15}$
Per-emb 33 A	$5.3^{+1.9}_{-2.8} \times 10^{15}$	$8.5^{+4.3}_{-3.5} \times 10^{13}$	$1.3^{+0.4}_{-0.5} \times 10^{15}$	$<6.1 \times 10^{15}$	$<5.2 \times 10^{14}$	$<1.4 \times 10^{15}$
Per-emb 33 B/C	$<3.9 \times 10^{15}$	$<9.8 \times 10^{13}$	$<1.2 \times 10^{15}$	$<1.2 \times 10^{16}$	$<8.5 \times 10^{14}$	$<1.3 \times 10^{15}$
L1448 IRS 3A	$8.4^{+4.5}_{-5.3} \times 10^{15}$	$1.7^{+0.8}_{-0.7} \times 10^{14}$	$2.3^{+1.1}_{-0.9} \times 10^{15}$	$<9.9 \times 10^{15}$	$<3.3 \times 10^{14}$	$<2.5 \times 10^{15}$
Per-emb 26	$8.9^{+3.2}_{-4.4} \times 10^{16}$	$1.5^{+0.7}_{-0.6} \times 10^{15}$	$1.0^{+0.5}_{-0.5} \times 10^{16}$	$5.9^{+1.6}_{-1.0} \times 10^{15}$	$<2.4 \times 10^{15}$	$<2.1 \times 10^{15}$
Per-emb 42	$9.0^{+4.6}_{-5.4} \times 10^{15}$	$<4.1 \times 10^{13}$	$<1.1 \times 10^{15}$	$<1.2 \times 10^{16}$	$<4.5 \times 10^{14}$	$<4.4 \times 10^{15}$
Per-emb 22 A	$2.0^{+1.1}_{-1.2} \times 10^{16}$	$1.8^{+0.9}_{-0.8} \times 10^{14}$	$<1.4 \times 10^{15}$	$<4.0 \times 10^{15}$	$<3.3 \times 10^{14}$	$<2.7 \times 10^{15}$
Per-emb 22 B	$1.6^{+0.7}_{-1.0} \times 10^{16}$	$1.6^{+0.7}_{-0.7} \times 10^{14}$	$<1.0 \times 10^{15}$	$<6.7 \times 10^{15}$	$<1.4 \times 10^{13}$	$<1.5 \times 10^{15}$
Per-emb 25	$<4.6 \times 10^{15}$	$<1.2 \times 10^{14}$	$<2.0 \times 10^{15}$	$<1.0 \times 10^{16}$	$<5.6 \times 10^{14}$	$<3.0 \times 10^{15}$
Per-emb 20	$1.3^{+0.8}_{-0.8} \times 10^{16}$	$<7.4 \times 10^{13}$	$<8.7 \times 10^{14}$	$<5.1 \times 10^{14}$	$<1.5 \times 10^{14}$	$<2.8 \times 10^{15}$
L1455 IRS 2	$<4.4 \times 10^{15}$	$<1.2 \times 10^{14}$	$<1.5 \times 10^{15}$	$<5.6 \times 10^{15}$	$<4.9 \times 10^{14}$	$<2.6 \times 10^{15}$
Per-emb 44	$8.1^{+5.0}_{-3.1} \times 10^{17}$	$5.9^{+1.8}_{-1.3} \times 10^{15}$	$1.6^{+0.6}_{-0.4} \times 10^{17}$	$1.1^{+0.2}_{-0.1} \times 10^{17}$	$2.5^{+1.7}_{-1.4} \times 10^{16}$	$9.6^{+1.8}_{-3.1} \times 10^{16}$
SVS 13A2	$6.9^{+4.5}_{-4.6} \times 10^{15}$	$<7.5 \times 10^{13}$	$<1.1 \times 10^{15}$	$<2.4 \times 10^{15}$	$<5.5 \times 10^{14}$	$<2.0 \times 10^{15}$
Per-emb 12 A	$7.3^{+6.4}_{-4.9} \times 10^{15}$	$<5.4 \times 10^{13}$	$1.3^{+1.2}_{-0.7} \times 10^{14}$	$<6.8 \times 10^{15}$	$<6.0 \times 10^{14}$	$<1.4 \times 10^{15}$
Per-emb 12 B	$2.0^{+1.0}_{-1.2} \times 10^{17}$	$2.9^{+1.1}_{-1.0} \times 10^{15}$	$9.2^{+3.6}_{-3.0} \times 10^{16}$	$5.1^{+0.9}_{-0.7} \times 10^{16}$	$1.7^{+1.1}_{-0.9} \times 10^{16}$	$5.2^{+1.2}_{-1.1} \times 10^{16}$
Per-emb 13	$5.0^{+3.3}_{-3.2} \times 10^{16}$	$7.3^{+3.2}_{-2.5} \times 10^{14}$	$3.7^{+1.6}_{-1.4} \times 10^{16}$	$2.9^{+0.6}_{-0.4} \times 10^{16}$	$1.1^{+0.6}_{-0.6} \times 10^{16}$	$1.5^{+0.4}_{-0.3} \times 10^{16}$
IRAS4B'	$<3.5 \times 10^{14}$	$<3.9 \times 10^{13}$	$<9.6 \times 10^{14}$	$<4.8 \times 10^{15}$	$<1.5 \times 10^{15}$	$<1.7 \times 10^{15}$
Per-emb 27	$1.1^{+1.3}_{-0.5} \times 10^{18}$	$6.5^{+2.1}_{-1.3} \times 10^{15}$	$8.4^{+3.6}_{-1.9} \times 10^{16}$	$5.7^{+1.1}_{-1.0} \times 10^{16}$	$2.9^{+1.8}_{-1.6} \times 10^{16}$	$4.8^{+1.3}_{-2.3} \times 10^{16}$
Per-emb 54	$<2.3 \times 10^{15}$	$<8.4 \times 10^{13}$	$<1.1 \times 10^{15}$	$<4.9 \times 10^{15}$	$<6.1 \times 10^{14}$	$<2.7 \times 10^{15}$
Per-emb 21	$1.7^{+0.8}_{-1.0} \times 10^{16}$	$<8.2 \times 10^{13}$	$<1.2 \times 10^{15}$	$<4.4 \times 10^{15}$	$<3.2 \times 10^{14}$	$<3.5 \times 10^{15}$
Per-emb 14	$<3.3 \times 10^{15}$	$<3.1 \times 10^{13}$	$<9.9 \times 10^{14}$	$<4.2 \times 10^{15}$	$<7.8 \times 10^{13}$	$<1.9 \times 10^{15}$
Per-emb 35 A	$5.3^{+2.2}_{-2.9} \times 10^{16}$	$5.0^{+2.5}_{-2.1} \times 10^{14}$	$2.0^{+0.9}_{-0.7} \times 10^{15}$	$<9.0 \times 10^{15}$	$<2.6 \times 10^{14}$	$<2.9 \times 10^{15}$
Per-emb 35 B	$6.3^{+3.0}_{-3.5} \times 10^{15}$	$6.9^{+3.5}_{-2.9} \times 10^{13}$	$<1.3 \times 10^{15}$	$<1.1 \times 10^{15}$	$<8.1 \times 10^{14}$	$<3.3 \times 10^{15}$
SVS 13B	$<2.4 \times 10^{15}$	$3.0^{+1.5}_{-1.1} \times 10^{13}$	$9.4^{+4.2}_{-3.2} \times 10^{14}$	$5.2^{+1.7}_{-1.0} \times 10^{15}$	$<4.1 \times 10^{15}$	$<1.6 \times 10^{15}$

Table 5
(Continued)

Source	CH_3OH (cm^{-2})	CH_3CN (cm^{-2})	CH_3OCHO (cm^{-2})	CH_3OCH_3 (cm^{-2})	CH_3CHO (cm^{-2})	C_2H_5OH (cm^{-2})
Per-emb 15	$<2.8 \times 10^{15}$	$<5.5 \times 10^{13}$	$<1.1 \times 10^{15}$	$<3.9 \times 10^{15}$	$<3.6 \times 10^{14}$	$<2.0 \times 10^{15}$
Per-emb 50	$<2.2 \times 10^{15}$	$<5.9 \times 10^{13}$	$<1.5 \times 10^{15}$	$<4.0 \times 10^{14}$	$<8.4 \times 10^{14}$	$<3.7 \times 10^{15}$
Per-emb 18	$2.3^{+1.0}_{-1.3} \times 10^{16}$	$2.3^{+1.1}_{-1.0} \times 10^{14}$	$2.1^{+1.1}_{-1.1} \times 10^{15}$	$<5.8 \times 10^{15}$	$<5.3 \times 10^{14}$	$<1.2 \times 10^{15}$
Per-emb 37	$<1.3 \times 10^{15}$	$<2.3 \times 10^{13}$	$<1.2 \times 10^{15}$	$<9.0 \times 10^{14}$	$<4.7 \times 10^{14}$	$<1.2 \times 10^{15}$
EDJ2009-235	$<4.0 \times 10^{15}$	$<8.1 \times 10^{13}$	$<8.1 \times 10^{14}$	$<5.1 \times 10^{15}$	$<1.0 \times 10^{15}$	$<2.3 \times 10^{15}$
Per-emb 36	$<3.6 \times 10^{15}$	$<8.4 \times 10^{13}$	$<1.4 \times 10^{15}$	$<1.0 \times 10^{15}$	$<1.1 \times 10^{13}$	$<3.3 \times 10^{15}$
B1-b S	$1.5^{+1.2}_{-0.9} \times 10^{16}$	$3.2^{+1.6}_{-1.4} \times 10^{14}$	$1.4^{+0.4}_{-0.2} \times 10^{16}$	$2.0^{+0.3}_{-0.3} \times 10^{16}$	$2.1^{+1.5}_{-1.2} \times 10^{15}$	$<1.5 \times 10^{15}$
B1-b N	$<3.9 \times 10^{15}$	$<8.5 \times 10^{13}$	$<2.6 \times 10^{14}$	$<3.4 \times 10^{15}$	$<2.2 \times 10^{12}$	$<2.1 \times 10^{15}$
Per-emb 29	$9.0^{+6.3}_{-5.9} \times 10^{16}$	$1.1^{+0.5}_{-0.4} \times 10^{15}$	$5.9^{+1.3}_{-0.9} \times 10^{16}$	$2.8^{+0.9}_{-0.7} \times 10^{16}$	$2.1^{+1.2}_{-1.3} \times 10^{15}$	$3.6^{+1.3}_{-1.0} \times 10^{16}$
Per-emb 10	$2.7^{+1.3}_{-1.6} \times 10^{15}$	$<8.8 \times 10^{13}$	$<5.2 \times 10^{14}$	$<5.9 \times 10^{15}$	$<1.4 \times 10^{15}$	$<2.9 \times 10^{15}$
Per-emb 40	$<4.8 \times 10^{15}$	$<8.6 \times 10^{13}$	$<1.1 \times 10^{15}$	$<6.0 \times 10^{15}$	$<4.5 \times 10^{14}$	$<3.5 \times 10^{15}$
Per-emb 2	$3.1^{+0.9}_{-1.4} \times 10^{15}$	$<5.1 \times 10^{13}$	$<9.4 \times 10^{13}$	$<8.3 \times 10^{14}$	$<2.0 \times 10^{14}$	$<1.9 \times 10^{15}$
Per-emb 5	$9.9^{+4.7}_{-6.0} \times 10^{15}$	$1.8^{+0.8}_{-0.8} \times 10^{14}$	$<9.1 \times 10^{14}$	$<1.1 \times 10^{16}$	$<4.7 \times 10^{12}$	$<2.6 \times 10^{15}$
Per-emb 1	$8.9^{+3.8}_{-5.4} \times 10^{15}$	$6.2^{+3.1}_{-2.6} \times 10^{13}$	$<3.9 \times 10^{14}$	$<1.2 \times 10^{15}$	$<4.8 \times 10^{15}$	$<3.4 \times 10^{15}$
Per-emb 11 A	$9.1^{+5.3}_{-5.6} \times 10^{15}$	$1.4^{+0.7}_{-0.6} \times 10^{14}$	$7.3^{+1.7}_{-1.3} \times 10^{15}$	$3.4^{+0.4}_{-0.3} \times 10^{15}$	$8.4^{+3.7}_{-3.8} \times 10^{15}$	$<2.3 \times 10^{15}$
Per-emb 11 B	$<2.6 \times 10^{15}$	$<1.9 \times 10^{13}$	$<2.7 \times 10^{14}$	$<3.7 \times 10^{15}$	$<4.2 \times 10^{12}$	$<9.3 \times 10^{14}$
Per-emb 11 C	$6.4^{+3.9}_{-4.0} \times 10^{15}$	$<4.6 \times 10^{13}$	$1.1^{+0.2}_{-0.3} \times 10^{15}$	$<4.0 \times 10^{14}$	$<5.1 \times 10^{14}$	$<2.4 \times 10^{15}$
Per-emb 8	$<3.4 \times 10^{15}$	$<8.0 \times 10^{13}$	$<1.5 \times 10^{14}$	$<5.2 \times 10^{14}$	$<5.2 \times 10^{13}$	$<4.2 \times 10^{15}$
Per-emb 55	$<3.9 \times 10^{15}$	$<7.9 \times 10^{13}$	$<1.1 \times 10^{15}$	$<4.9 \times 10^{15}$	$<5.7 \times 10^{14}$	$<3.0 \times 10^{15}$
Per-emb 16	$<2.0 \times 10^{15}$	$<6.1 \times 10^{13}$	$<1.1 \times 10^{15}$	$<3.7 \times 10^{15}$	$<5.6 \times 10^{12}$	$<3.3 \times 10^{15}$
Per-emb 28	$<1.7 \times 10^{16}$	$<4.0 \times 10^{14}$	$<3.5 \times 10^{14}$	$<1.7 \times 10^{16}$	$<1.8 \times 10^{13}$	$<7.1 \times 10^{15}$
Per-emb 53	$5.1^{+2.9}_{-3.2} \times 10^{15}$	$<7.7 \times 10^{13}$	$<1.0 \times 10^{14}$	$<3.8 \times 10^{15}$	$<4.5 \times 10^{12}$	$<1.5 \times 10^{15}$

Source	CH_3OCHO $v = 1$ (cm^{-2})	CH_3COCH_3 (cm^{-2})	t-HCOOH (cm^{-2})	C_2H_5CN (cm^{-2})	NH_2CHO (cm^{-2})	CH_2DCN (cm^{-2})
L1448 NW	$<1.7 \times 10^{16}$	$<5.0 \times 10^{14}$	$<1.2 \times 10^{15}$	$<2.5 \times 10^{14}$	$<2.1 \times 10^{14}$	$<7.5 \times 10^{13}$
Per-emb 33 A	$<7.6 \times 10^{15}$	$<7.6 \times 10^{14}$	$<4.3 \times 10^{14}$	$<2.3 \times 10^{14}$	$<2.0 \times 10^{14}$	$<1.2 \times 10^{14}$
Per-emb 33 B/C	$<4.7 \times 10^{15}$	$<1.0 \times 10^{15}$	$<1.2 \times 10^{15}$	$<2.3 \times 10^{14}$	$<5.1 \times 10^{13}$	$<1.5 \times 10^{14}$
L1448 IRS 3A	$<9.0 \times 10^{15}$	$<5.2 \times 10^{14}$	$<9.8 \times 10^{14}$	$<2.0 \times 10^{14}$	$<9.4 \times 10^{13}$	$<7.3 \times 10^{13}$
Per-emb 26	$<1.2 \times 10^{16}$	$<9.8 \times 10^{14}$	$1.0^{+0.6}_{-0.5} \times 10^{15}$	$2.6^{+0.8}_{-0.5} \times 10^{14}$	$1.4^{+0.5}_{-0.5} \times 10^{14}$	$1.5^{+0.7}_{-0.6} \times 10^{14}$
Per-emb 42	$<5.3 \times 10^{15}$	$<1.3 \times 10^{15}$	$<1.2 \times 10^{15}$	$<2.7 \times 10^{14}$	$<2.3 \times 10^{14}$	$<1.1 \times 10^{14}$
Per-emb 22 A	$<1.4 \times 10^{16}$	$<3.9 \times 10^{13}$	$<7.8 \times 10^{14}$	$<1.4 \times 10^{14}$	$<1.8 \times 10^{14}$	$<1.3 \times 10^{14}$
Per-emb 22 B	$<9.4 \times 10^{15}$	$<9.9 \times 10^{14}$	$<1.0 \times 10^{15}$	$<2.3 \times 10^{14}$	$<1.9 \times 10^{14}$	$<6.7 \times 10^{13}$
Per-emb 25	$<4.3 \times 10^{15}$	$<1.2 \times 10^{15}$	$<9.4 \times 10^{14}$	$<1.9 \times 10^{14}$	$<8.9 \times 10^{13}$	$<1.4 \times 10^{14}$
Per-emb 20	$<8.0 \times 10^{15}$	$<4.9 \times 10^{14}$	$<3.8 \times 10^{14}$	$<1.8 \times 10^{14}$	$9.6^{+3.1}_{-3.6} \times 10^{13}$	$<8.6 \times 10^{13}$
L1455 IRS 2	$<1.1 \times 10^{16}$	$<5.6 \times 10^{14}$	$<1.4 \times 10^{15}$	$<2.7 \times 10^{14}$	$<7.7 \times 10^{13}$	$<7.9 \times 10^{13}$
Per-emb 44	$1.7^{+0.6}_{-0.2} \times 10^{17}$	$6.3^{+3.7}_{-4.4} \times 10^{16}$	$1.5^{+0.6}_{-0.7} \times 10^{16}$	$2.8^{+0.9}_{-0.6} \times 10^{15}$	$1.9^{+0.6}_{-0.7} \times 10^{15}$	$1.9^{+1.0}_{-0.8} \times 10^{15}$
SVS 13A2	$<3.3 \times 10^{15}$	$<7.9 \times 10^{14}$	$<6.3 \times 10^{14}$	$<2.1 \times 10^{14}$	$<1.9 \times 10^{14}$	$<1.2 \times 10^{14}$
Per-emb 12 A	$<6.6 \times 10^{15}$	$<6.5 \times 10^{14}$	$<7.5 \times 10^{14}$	$<1.5 \times 10^{14}$	$<1.4 \times 10^{14}$	$<7.8 \times 10^{13}$
Per-emb 12 B	$1.1^{+0.3}_{-0.2} \times 10^{17}$	$3.9^{+5.5}_{-3.0} \times 10^{16}$	$9.1^{+4.8}_{-4.2} \times 10^{15}$	$2.3^{+0.6}_{-0.5} \times 10^{15}$	$1.1^{+0.4}_{-0.4} \times 10^{15}$	$1.3^{+0.6}_{-0.5} \times 10^{15}$
Per-emb 13	$3.8^{+1.4}_{-0.6} \times 10^{16}$	$9.6^{+14.4}_{-7.8} \times 10^{15}$	$1.4^{+0.8}_{-0.7} \times 10^{15}$	$5.7^{+1.5}_{-1.2} \times 10^{14}$	$2.3^{+0.8}_{-0.9} \times 10^{14}$	$2.3^{+1.1}_{-0.9} \times 10^{14}$
IRAS4B'	$<8.2 \times 10^{15}$	$<5.5 \times 10^{14}$	$<3.8 \times 10^{14}$	$<1.9 \times 10^{14}$	$<1.5 \times 10^{14}$	… [a]
Per-emb 27	$6.9^{+3.7}_{-1.2} \times 10^{16}$	$3.0^{+4.3}_{-2.4} \times 10^{16}$	$1.6^{+0.8}_{-0.7} \times 10^{16}$	$3.1^{+1.0}_{-0.8} \times 10^{15}$	$2.1^{+0.7}_{-0.8} \times 10^{15}$	$1.4^{+0.7}_{-0.5} \times 10^{15}$
Per-emb 54	$<1.6 \times 10^{16}$	$<1.0 \times 10^{15}$	$<4.0 \times 10^{14}$	$<2.4 \times 10^{14}$	$<2.4 \times 10^{14}$	$<1.0 \times 10^{14}$
Per-emb 21	$<1.4 \times 10^{16}$	$<9.0 \times 10^{14}$	$<3.5 \times 10^{14}$	$<2.2 \times 10^{14}$	$<2.1 \times 10^{14}$	$<4.3 \times 10^{13}$
Per-emb 14	$<1.5 \times 10^{16}$	$<7.4 \times 10^{14}$	$<9.8 \times 10^{14}$	$<1.2 \times 10^{14}$	$<1.2 \times 10^{14}$	$<8.8 \times 10^{13}$
Per-emb 35 A	$<8.8 \times 10^{15}$	$<8.0 \times 10^{14}$	$9.1^{+5.0}_{-4.5} \times 10^{14}$	$<1.5 \times 10^{14}$	$1.3^{+0.4}_{-0.5} \times 10^{14}$	$<1.0 \times 10^{14}$
Per-emb 35 B	$<8.6 \times 10^{15}$	$<9.1 \times 10^{14}$	$<8.5 \times 10^{14}$	$<1.9 \times 10^{14}$	$<2.0 \times 10^{14}$	$<6.8 \times 10^{13}$
SVS 13B	$<1.9 \times 10^{15}$	$<7.6 \times 10^{14}$	$<2.4 \times 10^{14}$	$<1.7 \times 10^{14}$	$<5.3 \times 10^{13}$	… [a]
Per-emb 15	$<9.5 \times 10^{15}$	$<7.9 \times 10^{14}$	$<7.6 \times 10^{14}$	$<6.2 \times 10^{13}$	$<1.7 \times 10^{14}$	$<1.2 \times 10^{14}$
Per- emb 50	$<8.1 \times 10^{15}$	$<3.6 \times 10^{14}$	$<8.6 \times 10^{14}$	$<2.3 \times 10^{14}$	$<6.9 \times 10^{13}$	$<6.2 \times 10^{13}$
Per-emb 18	$<3.2 \times 10^{15}$	$<6.9 \times 10^{14}$	$<2.9 \times 10^{14}$	$<1.6 \times 10^{14}$	$<1.6 \times 10^{14}$	$<8.2 \times 10^{13}$
Per-emb 37	$<1.3 \times 10^{16}$	$<2.7 \times 10^{13}$	$<9.2 \times 10^{14}$	$<1.8 \times 10^{14}$	$<1.8 \times 10^{14}$	$<5.6 \times 10^{13}$
EDJ2009-235	$<1.5 \times 10^{16}$	$<1.1 \times 10^{15}$	$<1.1 \times 10^{15}$	$<2.5 \times 10^{14}$	$<1.6 \times 10^{14}$	$<8.1 \times 10^{13}$
Per-emb 36	$<4.6 \times 10^{15}$	$<6.8 \times 10^{14}$	$<5.8 \times 10^{14}$	$<1.5 \times 10^{14}$	$<1.1 \times 10^{14}$	$<8.2 \times 10^{13}$
B1-b S	$2.1^{+0.8}_{-0.3} \times 10^{16}$	$6.4^{+8.8}_{-5.0} \times 10^{15}$	$<7.8 \times 10^{14}$	$2.9^{+0.7}_{-0.7} \times 10^{14}$	$<1.6 \times 10^{14}$	$2.2^{+1.2}_{-0.9} \times 10^{14}$
B1-b N	$<8.5 \times 10^{15}$	$<9.5 \times 10^{14}$	$<3.7 \times 10^{14}$	$<1.7 \times 10^{14}$	$<2.0 \times 10^{14}$	$<1.1 \times 10^{14}$
Per-emb 29	$7.0^{+2.8}_{-1.1} \times 10^{16}$	$2.5^{+3.7}_{-2.0} \times 10^{16}$	$1.5^{+0.8}_{-0.7} \times 10^{15}$	$1.5^{+0.4}_{-0.2} \times 10^{15}$	$3.5^{+1.2}_{-1.3} \times 10^{14}$	$5.3^{+2.6}_{-2.1} \times 10^{14}$
Per-emb 10	$<1.9 \times 10^{16}$	$<1.3 \times 10^{15}$	$<1.4 \times 10^{15}$	$<2.7 \times 10^{14}$	$<2.2 \times 10^{14}$	$<2.2 \times 10^{14}$
Per-emb 40	$<2.0 \times 10^{16}$	$<1.3 \times 10^{15}$	$<1.4 \times 10^{15}$	$<2.9 \times 10^{14}$	$<2.4 \times 10^{14}$	$<1.0 \times 10^{14}$
Per-emb 2	$<8.6 \times 10^{15}$	$<6.0 \times 10^{14}$	$<2.3 \times 10^{14}$	$<1.3 \times 10^{14}$	$<1.2 \times 10^{14}$	$<8.7 \times 10^{13}$

Table 5
(Continued)

Source	CH_3OCHO $v = 1$ (cm^{-2})	CH_3COCH_3 (cm^{-2})	*t*-HCOOH (cm^{-2})	C_2H_5CN (cm^{-2})	NH_2CHO (cm^{-2})	CH_2DCN (cm^{-2})
Per-emb 5	$<1.5 \times 10^{16}$	$<1.0 \times 10^{15}$	$<1.1 \times 10^{15}$	$<1.8 \times 10^{14}$	$<1.8 \times 10^{14}$	$<1.6 \times 10^{14}$
Per-emb 1	$<7.1 \times 10^{15}$	$<8.3 \times 10^{14}$	$<3.3 \times 10^{14}$	$<2.2 \times 10^{14}$	$<1.7 \times 10^{14}$	… [a]
Per-emb 11 A	$8.7^{+3.8}_{-1.6} \times 10^{15}$	$2.0^{+2.9}_{-1.6} \times 10^{15}$	$<8.5 \times 10^{14}$	$<1.3 \times 10^{14}$	$<1.7 \times 10^{14}$	… [a]
Per-emb 11 B	$<1.1 \times 10^{16}$	$<6.8 \times 10^{14}$	$<2.6 \times 10^{14}$	$<6.0 \times 10^{13}$	$<1.3 \times 10^{14}$	$<4.8 \times 10^{13}$
Per-emb 11 C	$<5.5 \times 10^{15}$	$<3.8 \times 10^{14}$	$<6.3 \times 10^{14}$	$<1.5 \times 10^{14}$	$<1.1 \times 10^{14}$	$<3.5 \times 10^{13}$
Per-emb 8	$<2.0 \times 10^{16}$	$<5.6 \times 10^{14}$	$<1.1 \times 10^{15}$	$<3.0 \times 10^{14}$	$<1.9 \times 10^{14}$	$<9.6 \times 10^{13}$
Per-emb 55	$<1.4 \times 10^{16}$	$<1.3 \times 10^{15}$	$<1.1 \times 10^{15}$	$<1.9 \times 10^{14}$	$<6.1 \times 10^{13}$	$<1.8 \times 10^{14}$
Per-emb 16	$<1.3 \times 10^{16}$	$<5.2 \times 10^{14}$	$<7.8 \times 10^{14}$	$<1.3 \times 10^{14}$	$<1.4 \times 10^{14}$	$<8.1 \times 10^{13}$
Per-emb 28	$<3.4 \times 10^{16}$	$<2.0 \times 10^{15}$	$<4.5 \times 10^{15}$	$<1.3 \times 10^{15}$	$<8.5 \times 10^{14}$	$<2.9 \times 10^{14}$
Per-emb 53	$<8.1 \times 10^{15}$	$<1.6 \times 10^{14}$	$<6.7 \times 10^{14}$	$<1.2 \times 10^{14}$	$<1.5 \times 10^{14}$	$<5.4 \times 10^{13}$

Notes. The column density is fitted with a source size of $0\farcs5$ and an aperture of the averaged convolved continuum size listed in Table 4 of the published article.
[a] The column densities of molecules are unconstrained due to the exclusion of the spectral window contaminated by the SiO emission.

The authors gratefully thank Shih-Ying Hsu for noticing this error and bringing it to our attention.

ORCID iDs

Yao-Lun Yang https://orcid.org/0000-0001-8227-2816
Nami Sakai https://orcid.org/0000-0002-3297-4497
Yichen Zhang https://orcid.org/0000-0001-7511-0034
Ziwei E. Zhang https://orcid.org/0000-0002-9927-2705
Aya E. Higuchi https://orcid.org/0000-0002-9221-2910
Ana López-Sepulcre https://orcid.org/0000-0002-6729-3640
Satoshi Yamamoto https://orcid.org/0000-0002-9865-0970
Bertrand Lefloch https://orcid.org/0000-0002-9397-3826
Mathilde Bouvier https://orcid.org/0000-0003-0167-0746
Cecilia Ceccarelli https://orcid.org/0000-0001-9664-6292
Tomoya Hirota https://orcid.org/0000-0003-1659-095X
Muneaki Imai https://orcid.org/0000-0002-5342-6262
Yoko Oya https://orcid.org/0000-0002-0197-8751
Takeshi Sakai https://orcid.org/0000-0003-4521-7492
Yoshimasa Watanabe https://orcid.org/0000-0002-9668-3592

The Astrophysical Journal, 913:155 (3pp), 2021 June 1 https://doi.org/10.3847/1538-4357/abff4e

Erratum: "The Perseus ALMA Chemistry Survey (PEACHES). I. The Complex Organic Molecules in Perseus Embedded Protostars" (2021, ApJ, 910, 20)

Yao-Lun Yang[1,2], Nami Sakai[2], Yichen Zhang[2], Nadia M. Murillo[2], Ziwei E. Zhang[2], Aya E. Higuchi[3], Shaoshan Zeng[2], Ana López-Sepulcre[4], Satoshi Yamamoto[5], Bertrand Lefloch[4], Mathilde Bouvier[4], Cecilia Ceccarelli[4], Tomoya Hirota[3], Muneaki Imai[5], Yoko Oya[5], Takeshi Sakai[6], and Yoshimasa Watanabe[7]
[1] Department of Astronomy, University of Virginia, Charlottesville, VA 22904-4235, USA; yaolunyang.astro@gmail.com
[2] RIKEN Cluster for Pioneering Research, Wako-shi, Saitama, 351-0106, Japan
[3] National Astronomical Observatory of Japan, Osawa, Mitaka, Tokyo 181-8588, Japan
[4] Univ. Grenoble Alpes, CNRS, Institut de Planétologie et d'Astrophysique de Grenoble (IPAG), F-38000 Grenoble, France
[5] Department of Physics, The University of Tokyo, 7-3-1, Hongo, Bunkyo-ku, Tokyo 113-0033, Japan
[6] Department of Communication Engineering and Informatics, Graduate School of Informatics and Engineering, The University of Electro-Communications, Chofugaoka, Chofu, Tokyo 182-8585, Japan
[7] Shibaura Institute of Technology, 3-9-14 Shibaura, Minato-ku, Tokyo 108-8548, Japan
Received 2021 May 6; published 2021 June 7

We have identified an error in the uncertainties of the fitted column densities of complex organic molecules (Table 5 in the published article). In particular, a few upper or lower uncertainties were underestimated by a factor of 10. A script was used to generate the table from the results of radiative transfer modeling (Section 3.4 in the published article). This script assumed the same order of magnitude for both upper and lower uncertainties, which is true in most cases. In a few cases, for example, the CH_3OH column density in L1448 NW, $2.1^{+0.7}_{-1.1} \times 10^{15}$ cm^{-2}, has different orders of magnitude in its upper and lower uncertainties. Thus, it was erroneously reported as $2.1^{+0.7}_{-0.1} \times 10^{15}$ cm^{-2}, because the script assumed an order of 10^{14} for both uncertainties. This error affects neither the conclusions nor the results and figures in the published article, because the error only occurred in the making of this table. A corrected version of Table 5 is provided here.

Table 5
Column Densities of Molecules

Source	CH_3OH (cm^{-2})	CH_3CN (cm^{-2})	CH_3OCHO (cm^{-2})	CH_3OCH_3 (cm^{-2})	CH_3CHO (cm^{-2})	C_2H_5OH (cm^{-2})
L1448 NW	$2.1^{+0.7}_{-1.1} \times 10^{15}$	$<1.0 \times 10^{14}$	$<1.4 \times 10^{15}$	$<4.8 \times 10^{15}$	$<6.9 \times 10^{14}$	$<3.3 \times 10^{15}$
Per-emb 33 A	$5.3^{+1.9}_{-2.8} \times 10^{15}$	$8.5^{+4.3}_{-3.5} \times 10^{13}$	$1.3^{+0.4}_{-0.5} \times 10^{15}$	$<6.1 \times 10^{15}$	$<5.2 \times 10^{14}$	$<1.4 \times 10^{15}$
Per-emb 33 B/C	$<3.9 \times 10^{15}$	$<9.8 \times 10^{13}$	$<1.2 \times 10^{15}$	$<1.2 \times 10^{16}$	$<8.5 \times 10^{14}$	$<1.3 \times 10^{15}$
L1448 IRS 3A	$8.4^{+4.5}_{-5.3} \times 10^{15}$	$1.7^{+0.8}_{-0.7} \times 10^{14}$	$2.3^{+1.1}_{-0.9} \times 10^{15}$	$<9.9 \times 10^{15}$	$<3.3 \times 10^{14}$	$<2.5 \times 10^{15}$
Per-emb 26	$8.9^{+3.2}_{-4.4} \times 10^{16}$	$1.5^{+0.7}_{-0.6} \times 10^{15}$	$1.0^{+0.5}_{-0.5} \times 10^{16}$	$5.9^{+1.6}_{-1.0} \times 10^{15}$	$<2.4 \times 10^{15}$	$<2.1 \times 10^{15}$
Per-emb 42	$9.0^{+4.6}_{-5.4} \times 10^{15}$	$<4.1 \times 10^{13}$	$<1.1 \times 10^{15}$	$<1.2 \times 10^{16}$	$<4.5 \times 10^{14}$	$<4.4 \times 10^{15}$
Per-emb 22 A	$2.0^{+1.1}_{-1.2} \times 10^{16}$	$1.8^{+0.9}_{-0.8} \times 10^{14}$	$<1.4 \times 10^{15}$	$<4.0 \times 10^{15}$	$<3.3 \times 10^{14}$	$<2.7 \times 10^{15}$
Per-emb 22 B	$1.6^{+0.7}_{-1.0} \times 10^{16}$	$1.6^{+0.7}_{-0.7} \times 10^{14}$	$<1.0 \times 10^{15}$	$<6.7 \times 10^{15}$	$<1.4 \times 10^{13}$	$<1.5 \times 10^{15}$
Per-emb 25	$<4.6 \times 10^{15}$	$<1.2 \times 10^{14}$	$<2.0 \times 10^{15}$	$<1.0 \times 10^{16}$	$<5.6 \times 10^{14}$	$<3.0 \times 10^{15}$
Per-emb 20	$1.3^{+0.8}_{-0.8} \times 10^{16}$	$<7.4 \times 10^{13}$	$<8.7 \times 10^{14}$	$<5.1 \times 10^{14}$	$<1.5 \times 10^{14}$	$<2.8 \times 10^{15}$
L1455 IRS 2	$<4.4 \times 10^{15}$	$<1.2 \times 10^{14}$	$<1.5 \times 10^{15}$	$<5.6 \times 10^{15}$	$<4.9 \times 10^{14}$	$<2.6 \times 10^{15}$
Per-emb 44	$8.1^{+5.0}_{-3.1} \times 10^{17}$	$5.9^{+1.8}_{-1.3} \times 10^{15}$	$1.6^{+0.6}_{-0.4} \times 10^{17}$	$1.1^{+0.2}_{-0.1} \times 10^{17}$	$2.5^{+1.7}_{-1.4} \times 10^{16}$	$9.6^{+1.8}_{-3.1} \times 10^{16}$
SVS 13A2	$6.9^{+4.5}_{-4.6} \times 10^{15}$	$<7.5 \times 10^{13}$	$<1.1 \times 10^{15}$	$<2.4 \times 10^{15}$	$<5.5 \times 10^{14}$	$<2.0 \times 10^{15}$
Per-emb 12 A	$7.3^{+6.4}_{-4.9} \times 10^{15}$	$<5.4 \times 10^{13}$	$1.3^{+1.2}_{-0.7} \times 10^{14}$	$<6.8 \times 10^{15}$	$<6.0 \times 10^{14}$	$<1.4 \times 10^{15}$
Per-emb 12 B	$2.0^{+1.0}_{-1.2} \times 10^{17}$	$2.9^{+1.1}_{-1.0} \times 10^{15}$	$9.2^{+3.6}_{-3.0} \times 10^{16}$	$5.1^{+0.9}_{-0.7} \times 10^{16}$	$1.7^{+1.1}_{-0.9} \times 10^{16}$	$5.2^{+1.2}_{-1.1} \times 10^{16}$
Per-emb 13	$5.0^{+3.3}_{-3.2} \times 10^{16}$	$7.3^{+3.2}_{-2.5} \times 10^{14}$	$3.7^{+1.6}_{-1.4} \times 10^{16}$	$2.9^{+0.6}_{-0.4} \times 10^{16}$	$1.1^{+0.6}_{-0.6} \times 10^{16}$	$1.5^{+0.4}_{-0.3} \times 10^{16}$
IRAS4B'	$<3.5 \times 10^{14}$	$<3.9 \times 10^{13}$	$<9.6 \times 10^{14}$	$<4.8 \times 10^{15}$	$<1.5 \times 10^{15}$	$<1.7 \times 10^{15}$
Per-emb 27	$1.1^{+1.3}_{-0.5} \times 10^{18}$	$6.5^{+2.1}_{-1.3} \times 10^{15}$	$8.4^{+3.6}_{-1.9} \times 10^{16}$	$5.7^{+1.1}_{-1.0} \times 10^{16}$	$2.9^{+1.8}_{-1.6} \times 10^{16}$	$4.8^{+1.3}_{-2.3} \times 10^{16}$
Per-emb 54	$<2.3 \times 10^{15}$	$<8.4 \times 10^{13}$	$<1.1 \times 10^{15}$	$<4.9 \times 10^{15}$	$<6.1 \times 10^{14}$	$<2.7 \times 10^{15}$
Per-emb 21	$1.7^{+0.8}_{-1.0} \times 10^{16}$	$<8.2 \times 10^{13}$	$<1.2 \times 10^{15}$	$<4.4 \times 10^{15}$	$<3.2 \times 10^{14}$	$<3.5 \times 10^{15}$
Per-emb 14	$<3.3 \times 10^{15}$	$<3.1 \times 10^{13}$	$<9.9 \times 10^{14}$	$<4.2 \times 10^{15}$	$<7.8 \times 10^{13}$	$<1.9 \times 10^{15}$
Per-emb 35 A	$5.3^{+2.2}_{-2.9} \times 10^{16}$	$5.0^{+2.5}_{-2.1} \times 10^{14}$	$2.0^{+0.9}_{-0.7} \times 10^{15}$	$<9.0 \times 10^{15}$	$<2.6 \times 10^{14}$	$<2.9 \times 10^{15}$
Per-emb 35 B	$6.3^{+3.0}_{-3.5} \times 10^{15}$	$6.9^{+3.5}_{-2.9} \times 10^{13}$	$<1.3 \times 10^{15}$	$<1.1 \times 10^{15}$	$<8.1 \times 10^{14}$	$<3.3 \times 10^{15}$
SVS 13B	$<2.4 \times 10^{15}$	$3.0^{+1.5}_{-1.1} \times 10^{13}$	$9.4^{+4.2}_{-3.2} \times 10^{14}$	$5.2^{+1.7}_{-1.0} \times 10^{15}$	$<4.1 \times 10^{15}$	$<1.6 \times 10^{15}$

Table 5
(Continued)

Source	CH_3OH (cm^{-2})	CH_3CN (cm^{-2})	CH_3OCHO (cm^{-2})	CH_3OCH_3 (cm^{-2})	CH_3CHO (cm^{-2})	C_2H_5OH (cm^{-2})
Per-emb 15	$<2.8 \times 10^{15}$	$<5.5 \times 10^{13}$	$<1.1 \times 10^{15}$	$<3.9 \times 10^{15}$	$<3.6 \times 10^{14}$	$<2.0 \times 10^{15}$
Per-emb 50	$<2.2 \times 10^{15}$	$<5.9 \times 10^{13}$	$<1.5 \times 10^{15}$	$<4.0 \times 10^{14}$	$<8.4 \times 10^{14}$	$<3.7 \times 10^{15}$
Per-emb 18	$2.3^{+1.0}_{-1.3} \times 10^{16}$	$2.3^{+1.1}_{-1.0} \times 10^{14}$	$2.1^{+1.1}_{-1.1} \times 10^{15}$	$<5.8 \times 10^{15}$	$<5.3 \times 10^{14}$	$<1.2 \times 10^{15}$
Per-emb 37	$<1.3 \times 10^{15}$	$<2.3 \times 10^{13}$	$<1.2 \times 10^{15}$	$<9.0 \times 10^{14}$	$<4.7 \times 10^{14}$	$<1.2 \times 10^{15}$
EDJ2009-235	$<4.0 \times 10^{15}$	$<8.1 \times 10^{13}$	$<8.1 \times 10^{14}$	$<5.1 \times 10^{15}$	$<1.0 \times 10^{15}$	$<2.3 \times 10^{15}$
Per-emb 36	$<3.6 \times 10^{15}$	$<8.4 \times 10^{13}$	$<1.4 \times 10^{15}$	$<1.0 \times 10^{15}$	$<1.1 \times 10^{13}$	$<3.3 \times 10^{15}$
B1-b S	$1.5^{+1.2}_{-0.9} \times 10^{16}$	$3.2^{+1.6}_{-1.4} \times 10^{14}$	$1.4^{+0.4}_{-0.2} \times 10^{16}$	$2.0^{+0.3}_{-0.3} \times 10^{16}$	$2.1^{+1.5}_{-1.2} \times 10^{15}$	$<1.5 \times 10^{15}$
B1-b N	$<3.9 \times 10^{15}$	$<8.5 \times 10^{13}$	$<2.6 \times 10^{14}$	$<3.4 \times 10^{15}$	$<2.2 \times 10^{12}$	$<2.1 \times 10^{15}$
Per-emb 29	$9.0^{+6.3}_{-5.9} \times 10^{16}$	$1.1^{+0.5}_{-0.4} \times 10^{15}$	$5.9^{+1.3}_{-0.9} \times 10^{16}$	$2.8^{+0.9}_{-0.7} \times 10^{16}$	$2.1^{+1.2}_{-1.3} \times 10^{15}$	$3.6^{+1.3}_{-1.0} \times 10^{16}$
Per-emb 10	$2.7^{+1.3}_{-1.6} \times 10^{15}$	$<8.8 \times 10^{13}$	$<5.2 \times 10^{14}$	$<5.9 \times 10^{15}$	$<1.4 \times 10^{15}$	$<2.9 \times 10^{15}$
Per-emb 40	$<4.8 \times 10^{15}$	$<8.6 \times 10^{13}$	$<1.1 \times 10^{15}$	$<6.0 \times 10^{15}$	$<4.5 \times 10^{14}$	$<3.5 \times 10^{15}$
Per-emb 2	$3.1^{+0.9}_{-1.4} \times 10^{15}$	$<5.1 \times 10^{13}$	$<9.4 \times 10^{13}$	$<8.3 \times 10^{14}$	$<2.0 \times 10^{14}$	$<1.9 \times 10^{15}$
Per-emb 5	$9.9^{+4.7}_{-6.0} \times 10^{15}$	$1.8^{+0.8}_{-0.8} \times 10^{14}$	$<9.1 \times 10^{14}$	$<1.1 \times 10^{16}$	$<4.7 \times 10^{12}$	$<2.6 \times 10^{15}$
Per-emb 1	$8.9^{+3.8}_{-5.4} \times 10^{15}$	$6.2^{+3.1}_{-2.6} \times 10^{13}$	$<3.9 \times 10^{14}$	$<1.2 \times 10^{15}$	$<4.8 \times 10^{15}$	$<3.4 \times 10^{15}$
Per-emb 11 A	$9.1^{+5.3}_{-5.6} \times 10^{15}$	$1.4^{+0.7}_{-0.6} \times 10^{14}$	$7.3^{+1.7}_{-1.3} \times 10^{15}$	$3.4^{+0.4}_{-0.3} \times 10^{15}$	$8.4^{+3.7}_{-3.8} \times 10^{15}$	$<2.3 \times 10^{15}$
Per-emb 11 B	$<2.6 \times 10^{15}$	$<1.9 \times 10^{13}$	$<2.7 \times 10^{14}$	$<3.7 \times 10^{15}$	$<4.2 \times 10^{12}$	$<9.3 \times 10^{14}$
Per-emb 11 C	$6.4^{+3.9}_{-4.0} \times 10^{15}$	$<4.6 \times 10^{13}$	$1.1^{+0.2}_{-0.3} \times 10^{15}$	$<4.0 \times 10^{14}$	$<5.1 \times 10^{14}$	$<2.4 \times 10^{15}$
Per-emb 8	$<3.4 \times 10^{15}$	$<8.0 \times 10^{13}$	$<1.5 \times 10^{14}$	$<5.2 \times 10^{14}$	$<5.2 \times 10^{13}$	$<4.2 \times 10^{15}$
Per-emb 55	$<3.9 \times 10^{15}$	$<7.9 \times 10^{13}$	$<1.1 \times 10^{15}$	$<4.9 \times 10^{15}$	$<5.7 \times 10^{14}$	$<3.0 \times 10^{15}$
Per-emb 16	$<2.0 \times 10^{15}$	$<6.1 \times 10^{13}$	$<1.1 \times 10^{15}$	$<3.7 \times 10^{15}$	$<5.6 \times 10^{12}$	$<3.3 \times 10^{15}$
Per-emb 28	$<1.7 \times 10^{16}$	$<4.0 \times 10^{14}$	$<3.5 \times 10^{14}$	$<1.7 \times 10^{16}$	$<1.8 \times 10^{13}$	$<7.1 \times 10^{15}$
Per-emb 53	$5.1^{+2.9}_{-3.2} \times 10^{15}$	$<7.7 \times 10^{13}$	$<1.0 \times 10^{14}$	$<3.8 \times 10^{15}$	$<4.5 \times 10^{12}$	$<1.5 \times 10^{15}$

Source	CH_3OCHO $v = 1$ (cm^{-2})	CH_3COCH_3 (cm^{-2})	t-HCOOH (cm^{-2})	C_2H_5CN (cm^{-2})	NH_2CHO (cm^{-2})	CH_2DCN (cm^{-2})
L1448 NW	$<1.7 \times 10^{16}$	$<5.0 \times 10^{14}$	$<1.2 \times 10^{15}$	$<2.5 \times 10^{14}$	$<2.1 \times 10^{14}$	$<7.5 \times 10^{13}$
Per-emb 33 A	$<7.6 \times 10^{15}$	$<7.6 \times 10^{14}$	$<4.3 \times 10^{14}$	$<2.3 \times 10^{14}$	$<2.0 \times 10^{14}$	$<1.2 \times 10^{14}$
Per-emb 33 B/C	$<4.7 \times 10^{15}$	$<1.0 \times 10^{15}$	$<1.2 \times 10^{15}$	$<2.3 \times 10^{14}$	$<5.1 \times 10^{13}$	$<1.5 \times 10^{14}$
L1448 IRS 3A	$<9.0 \times 10^{15}$	$<5.2 \times 10^{14}$	$<9.8 \times 10^{14}$	$<2.0 \times 10^{14}$	$<9.4 \times 10^{13}$	$<7.3 \times 10^{13}$
Per-emb 26	$<1.2 \times 10^{16}$	$<9.8 \times 10^{14}$	$1.0^{+0.6}_{-0.5} \times 10^{15}$	$2.6^{+0.8}_{-0.5} \times 10^{14}$	$1.4^{+0.5}_{-0.5} \times 10^{14}$	$1.5^{+0.7}_{-0.6} \times 10^{14}$
Per-emb 42	$<5.3 \times 10^{15}$	$<1.3 \times 10^{15}$	$<1.2 \times 10^{15}$	$<2.7 \times 10^{14}$	$<2.3 \times 10^{14}$	$<1.1 \times 10^{14}$
Per-emb 22 A	$<1.4 \times 10^{16}$	$<3.9 \times 10^{13}$	$<7.8 \times 10^{14}$	$<1.4 \times 10^{14}$	$<1.8 \times 10^{14}$	$<1.3 \times 10^{14}$
Per-emb 22 B	$<9.4 \times 10^{15}$	$<9.9 \times 10^{14}$	$<1.0 \times 10^{15}$	$<2.3 \times 10^{14}$	$<1.9 \times 10^{14}$	$<6.7 \times 10^{13}$
Per-emb 25	$<4.3 \times 10^{15}$	$<1.2 \times 10^{15}$	$<9.4 \times 10^{14}$	$<1.9 \times 10^{14}$	$<8.9 \times 10^{13}$	$<1.4 \times 10^{14}$
Per-emb 20	$<8.0 \times 10^{15}$	$<4.9 \times 10^{14}$	$<3.8 \times 10^{14}$	$<1.8 \times 10^{14}$	$9.6^{+3.1}_{-3.6} \times 10^{13}$	$<8.6 \times 10^{13}$
L1455 IRS 2	$<1.1 \times 10^{16}$	$<5.6 \times 10^{14}$	$<1.4 \times 10^{15}$	$<2.7 \times 10^{14}$	$<7.7 \times 10^{13}$	$<7.9 \times 10^{13}$
Per-emb 44	$1.7^{+0.6}_{-0.2} \times 10^{17}$	$6.3^{+3.7}_{-4.4} \times 10^{16}$	$1.5^{+0.6}_{-0.7} \times 10^{16}$	$2.8^{+0.9}_{-0.6} \times 10^{15}$	$1.9^{+0.6}_{-0.7} \times 10^{15}$	$1.9^{+1.0}_{-0.8} \times 10^{15}$
SVS 13A2	$<3.3 \times 10^{15}$	$<7.9 \times 10^{14}$	$<6.3 \times 10^{14}$	$<2.1 \times 10^{14}$	$<1.9 \times 10^{14}$	$<1.2 \times 10^{14}$
Per-emb 12 A	$<6.6 \times 10^{15}$	$<6.5 \times 10^{14}$	$<7.5 \times 10^{14}$	$<1.5 \times 10^{14}$	$<1.4 \times 10^{14}$	$<7.8 \times 10^{13}$
Per-emb 12 B	$1.1^{+0.3}_{-0.2} \times 10^{17}$	$3.9^{+5.5}_{-3.0} \times 10^{16}$	$9.1^{+4.8}_{-4.2} \times 10^{15}$	$2.3^{+0.6}_{-0.5} \times 10^{15}$	$1.1^{+0.4}_{-0.4} \times 10^{15}$	$1.3^{+0.6}_{-0.5} \times 10^{15}$
Per-emb 13	$3.8^{+1.4}_{-0.6} \times 10^{16}$	$9.6^{+14.4}_{-7.8} \times 10^{15}$	$1.4^{+0.8}_{-0.7} \times 10^{15}$	$5.7^{+1.5}_{-1.2} \times 10^{14}$	$2.3^{+0.8}_{-0.9} \times 10^{14}$	$2.3^{+1.1}_{-0.9} \times 10^{14}$
IRAS4B'	$<8.2 \times 10^{15}$	$<5.5 \times 10^{14}$	$<3.8 \times 10^{14}$	$<1.9 \times 10^{14}$	$<1.5 \times 10^{14}$	… [a]
Per-emb 27	$6.9^{+3.7}_{-1.2} \times 10^{16}$	$3.0^{+4.3}_{-2.4} \times 10^{16}$	$1.6^{+0.8}_{-0.7} \times 10^{16}$	$3.1^{+1.0}_{-0.8} \times 10^{15}$	$2.1^{+0.7}_{-0.8} \times 10^{15}$	$1.4^{+0.7}_{-0.5} \times 10^{15}$
Per-emb 54	$<1.6 \times 10^{16}$	$<1.0 \times 10^{15}$	$<4.0 \times 10^{14}$	$<2.4 \times 10^{14}$	$<2.4 \times 10^{14}$	$<1.0 \times 10^{14}$
Per-emb 21	$<1.4 \times 10^{16}$	$<9.0 \times 10^{14}$	$<3.5 \times 10^{14}$	$<2.2 \times 10^{14}$	$<2.1 \times 10^{14}$	$<4.3 \times 10^{13}$
Per-emb 14	$<1.5 \times 10^{16}$	$<7.4 \times 10^{14}$	$<9.8 \times 10^{14}$	$<1.2 \times 10^{14}$	$<1.2 \times 10^{14}$	$<8.8 \times 10^{13}$
Per-emb 35 A	$<8.8 \times 10^{15}$	$<8.0 \times 10^{14}$	$9.1^{+5.0}_{-4.5} \times 10^{14}$	$<1.5 \times 10^{14}$	$1.3^{+0.4}_{-0.5} \times 10^{14}$	$<1.0 \times 10^{14}$
Per-emb 35 B	$<8.6 \times 10^{15}$	$<9.1 \times 10^{14}$	$<8.5 \times 10^{14}$	$<1.9 \times 10^{14}$	$<2.0 \times 10^{14}$	$<6.8 \times 10^{13}$
SVS 13B	$<1.9 \times 10^{15}$	$<7.6 \times 10^{14}$	$<2.4 \times 10^{14}$	$<1.7 \times 10^{14}$	$<5.3 \times 10^{13}$	… [a]
Per-emb 15	$<9.5 \times 10^{15}$	$<7.9 \times 10^{14}$	$<7.6 \times 10^{14}$	$<6.2 \times 10^{13}$	$<1.7 \times 10^{14}$	$<1.2 \times 10^{14}$
Per- emb 50	$<8.1 \times 10^{15}$	$<3.6 \times 10^{14}$	$<8.6 \times 10^{14}$	$<2.3 \times 10^{14}$	$<6.9 \times 10^{13}$	$<6.2 \times 10^{13}$
Per-emb 18	$<3.2 \times 10^{15}$	$<6.9 \times 10^{14}$	$<2.9 \times 10^{14}$	$<1.6 \times 10^{14}$	$<1.6 \times 10^{14}$	$<8.2 \times 10^{13}$
Per-emb 37	$<1.3 \times 10^{16}$	$<2.7 \times 10^{13}$	$<9.2 \times 10^{14}$	$<1.8 \times 10^{14}$	$<1.8 \times 10^{14}$	$<5.6 \times 10^{13}$
EDJ2009-235	$<1.5 \times 10^{16}$	$<1.1 \times 10^{15}$	$<1.1 \times 10^{15}$	$<2.5 \times 10^{14}$	$<1.6 \times 10^{14}$	$<8.1 \times 10^{13}$
Per-emb 36	$<4.6 \times 10^{15}$	$<6.8 \times 10^{14}$	$<5.8 \times 10^{14}$	$<1.5 \times 10^{14}$	$<1.1 \times 10^{14}$	$<8.2 \times 10^{13}$
B1-b S	$2.1^{+0.8}_{-0.3} \times 10^{16}$	$6.4^{+8.8}_{-5.0} \times 10^{15}$	$<7.8 \times 10^{14}$	$2.9^{+0.7}_{-0.7} \times 10^{14}$	$<1.6 \times 10^{14}$	$2.2^{+1.2}_{-0.9} \times 10^{14}$
B1-b N	$<8.5 \times 10^{15}$	$<9.5 \times 10^{14}$	$<3.7 \times 10^{14}$	$<1.7 \times 10^{14}$	$<2.0 \times 10^{14}$	$<1.1 \times 10^{14}$
Per-emb 29	$7.0^{+2.8}_{-1.1} \times 10^{16}$	$2.5^{+3.7}_{-2.0} \times 10^{16}$	$1.5^{+0.8}_{-0.7} \times 10^{15}$	$1.5^{+0.4}_{-0.2} \times 10^{15}$	$3.5^{+1.2}_{-1.3} \times 10^{14}$	$5.3^{+2.6}_{-2.1} \times 10^{14}$
Per-emb 10	$<1.9 \times 10^{16}$	$<1.3 \times 10^{15}$	$<1.4 \times 10^{15}$	$<2.7 \times 10^{14}$	$<2.2 \times 10^{14}$	$<2.2 \times 10^{14}$
Per-emb 40	$<2.0 \times 10^{16}$	$<1.3 \times 10^{15}$	$<1.4 \times 10^{15}$	$<2.9 \times 10^{14}$	$<2.4 \times 10^{14}$	$<1.0 \times 10^{14}$
Per-emb 2	$<8.6 \times 10^{15}$	$<6.0 \times 10^{14}$	$<2.3 \times 10^{14}$	$<1.3 \times 10^{14}$	$<1.2 \times 10^{14}$	$<8.7 \times 10^{13}$

Table 5
(Continued)

Source	CH_3OCHO $v = 1$ (cm^{-2})	CH_3COCH_3 (cm^{-2})	*t*-HCOOH (cm^{-2})	C_2H_5CN (cm^{-2})	NH_2CHO (cm^{-2})	CH_2DCN (cm^{-2})
Per-emb 5	$<1.5 \times 10^{16}$	$<1.0 \times 10^{15}$	$<1.1 \times 10^{15}$	$<1.8 \times 10^{14}$	$<1.8 \times 10^{14}$	$<1.6 \times 10^{14}$
Per-emb 1	$<7.1 \times 10^{15}$	$<8.3 \times 10^{14}$	$<3.3 \times 10^{14}$	$<2.2 \times 10^{14}$	$<1.7 \times 10^{14}$	… [a]
Per-emb 11 A	$8.7^{+3.8}_{-1.6} \times 10^{15}$	$2.0^{+2.9}_{-1.6} \times 10^{15}$	$<8.5 \times 10^{14}$	$<1.3 \times 10^{14}$	$<1.7 \times 10^{14}$	… [a]
Per-emb 11 B	$<1.1 \times 10^{16}$	$<6.8 \times 10^{14}$	$<2.6 \times 10^{14}$	$<6.0 \times 10^{13}$	$<1.3 \times 10^{14}$	$<4.8 \times 10^{13}$
Per-emb 11 C	$<5.5 \times 10^{15}$	$<3.8 \times 10^{14}$	$<6.3 \times 10^{14}$	$<1.5 \times 10^{14}$	$<1.1 \times 10^{14}$	$<3.5 \times 10^{13}$
Per-emb 8	$<2.0 \times 10^{16}$	$<5.6 \times 10^{14}$	$<1.1 \times 10^{15}$	$<3.0 \times 10^{14}$	$<1.9 \times 10^{14}$	$<9.6 \times 10^{13}$
Per-emb 55	$<1.4 \times 10^{16}$	$<1.3 \times 10^{15}$	$<1.1 \times 10^{15}$	$<1.9 \times 10^{14}$	$<6.1 \times 10^{13}$	$<1.8 \times 10^{14}$
Per-emb 16	$<1.3 \times 10^{16}$	$<5.2 \times 10^{14}$	$<7.8 \times 10^{14}$	$<1.3 \times 10^{14}$	$<1.4 \times 10^{14}$	$<8.1 \times 10^{13}$
Per-emb 28	$<3.4 \times 10^{16}$	$<2.0 \times 10^{15}$	$<4.5 \times 10^{15}$	$<1.3 \times 10^{15}$	$<8.5 \times 10^{14}$	$<2.9 \times 10^{14}$
Per-emb 53	$<8.1 \times 10^{15}$	$<1.6 \times 10^{14}$	$<6.7 \times 10^{14}$	$<1.2 \times 10^{14}$	$<1.5 \times 10^{14}$	$<5.4 \times 10^{13}$

Notes. The column density is fitted with a source size of $0\farcs5$ and an aperture of the averaged convolved continuum size listed in Table 4 of the published article.
[a] The column densities of molecules are unconstrained due to the exclusion of the spectral window contaminated by the SiO emission.

The authors gratefully thank Shih-Ying Hsu for noticing this error and bringing it to our attention.

ORCID iDs

Yao-Lun Yang https://orcid.org/0000-0001-8227-2816
Nami Sakai https://orcid.org/0000-0002-3297-4497
Yichen Zhang https://orcid.org/0000-0001-7511-0034
Ziwei E. Zhang https://orcid.org/0000-0002-9927-2705
Aya E. Higuchi https://orcid.org/0000-0002-9221-2910
Ana López-Sepulcre https://orcid.org/0000-0002-6729-3640
Satoshi Yamamoto https://orcid.org/0000-0002-9865-0970
Bertrand Lefloch https://orcid.org/0000-0002-9397-3826
Mathilde Bouvier https://orcid.org/0000-0003-0167-0746
Cecilia Ceccarelli https://orcid.org/0000-0001-9664-6292
Tomoya Hirota https://orcid.org/0000-0003-1659-095X
Muneaki Imai https://orcid.org/0000-0002-5342-6262
Yoko Oya https://orcid.org/0000-0002-0197-8751
Takeshi Sakai https://orcid.org/0000-0003-4521-7492
Yoshimasa Watanabe https://orcid.org/0000-0002-9668-3592